Radiative Transfer and Photochemistry in the Upper Atmosphere of Jupiter

Thesis by

George Randall Gladstone

In Partial Fulfillment of the Requirements

for the Degree of

Doctor of Philosophy

California Institute of Technology

Pasadena, California

1983

(submitted 29 September 1982)

Acknowledgements

It is with much pleasure that I acknowledge the help given to me by my thesis advisor Dr. Yuk Yung. I have greatly benefited from his friendship, experience, and guidance, and without his inspiration this work would not have been possible.

I would like to thank my academic advisor, Dr. Duane Muhleman, for his helpful advice during my class-taking years, and Drs. Peter Goldreich, Andrew Ingersoll, Dave Stevenson, and John Trauger for the help and insight they have given me on a number of occasions. I am also grateful to Dr. Mark Allen for sharing his knowledge of chemistry and programming with me, as well as the program KINETICS.

My fellow graduate students and friends within and without the department have helped to make my stay at Caltech a very pleasant and memorable one. In particular I would like to thank Dr. Jobea Cimino, Todd Clancy, Dr. John Dvorak, Jim Friedson, Lucien Froidevaux, Dr. Bruce Jakosky, Dave Jewitt, Randy Kirk, Jonathan Lunine, Dr. Bill McKinnon, Dave Paige, Dr. Quinn Passey, Judy Pechmann, Carolyn Porco, Don Rudy, Mike Summers, Dan Wenkert, and Dr. Jack Wisdom.

I owe much to Kay Campbell for helping me understand how the department and Caltech operate, and to Donna Lathrop for her excellent assistance in preparing papers and this thesis.

Many people outside Caltech have helped me with this project. I thank Drs. D.G. Hummer and R.R. Meier for their assistance with the frequency redistribution program. I am also grateful to Drs. John Clarke, Bill Maguire, Jack McConnell, and Don Shemansky for useful discussions regarding their data.

This work was supported in part by NASA grant NSG-7376 of the Planetary Atmosphere Program. I gratefully acknowledge tuition fellowships received from Caltech.

Finally, I would like to thank my family, most of all.

Abstract

The upper atmosphere of Jupiter, from the tropopause to well above the homopause, is investigated as to its compositional structure and vertical mixing parameters. Constraints are obtained through the study of the radiative transfer of ultraviolet resonance lines and continuum radiation. These constraints and others are then used in the modeling of the hydrocarbon photochemistry of Jupiter.

A direct finite difference numerical solution for the equation of radiative transfer is developed for use in planetary atmospheres. The procedure uses a plane-parallel atmosphere, and can treat partial frequency redistribution (for use in the radiative transfer of optically thick resonance lines), inhomogeneity, external or internal sources, and various boundary conditions. Isotropic scattering is assumed, but in the case of no frequency redistribution, a Rayleigh phase function may be used. A program utilizing this solution is tested against more powerful and elaborate methods. This program is then applied to the Lyman-α aurora of Jupiter, and detailed line profiles are presented.

Using this program, a study is made of the UV reflection spectrum of Jupiter as measured by the *International Ultraviolet Explorer*. Detailed modeling reveals the mixing ratios of C_2H_2, C_2H_6, and C_4H_2 to be $(1.0 \pm 0.1)\times10^{-7}$,$(6.6 \pm 5.3)\times10^{-6}$, and $(2.9 \pm 2.0)\times10^{-10}$, respectively in the pressure region between ~ 3 and 40 mbar. Upper limits in this pressure region for the mixing ratios of C_2H_4 and NH_3 were determined to be $(3.9 \pm {}^{4.9}_{3.9})\times10^{-10}$ and $(4.2 \pm {}^{6.7}_{4.2})\times10^{-9}$, respectively. An upper limit to the optical depth of dust above the tropopause, assuming it is well mixed, is $0.2 \pm {}^{0.3}_{0.2}$, and an upper limit on the dayglow emission by the Lyman bands of H_2 is $1.4 \pm {}^{2.4}_{1.4}$ kiloRayleighs. Comparison with *Voyager* results suggests that the scale height of C_2H_2 in the

region 150-10 mbar is approximately twice that of the bulk atmosphere, consistent with the *IUE* observation of cosine-like limb darkening in the north-south direction on Jupiter in the UV.

The resonant scattering of the solar He I 584 Å emission line by the upper Jovian atmosphere is investigated next. The observed intensity of this scattered line depends directly on the eddy diffusion for vertical mixing (K_h) and the temperature (T_h) at the homopause. Using the temperature profile determined by the *Voyager UVS* experiment, a value of $K_h = 1.3 \times 10^6$ cm^2 s^{-1} ± 30% is obtained. If the temperature profile was the same during the *Pioneer* 10 encounter with Jupiter, then $K_h \approx 1 \times 10^8$ cm^2 s^{-1} at that time. The He 584 Å brightness is found not to depend strongly on the gradients of either the eddy diffusion or temperature profiles. A semi-analytical expression for computing the He 584 Å brightness for a constant-K, constant-T atmosphere is derived and compared with calculations by other authors. It is speculated that the apparent decrease in K_h by two orders of magnitude between the *Pioneer* and *Voyager* encounters may be the result of an increase in the pole-to-equator circulation in the thermosphere, perhaps driven by the solar cycle.

The above results are used as constraints for a one-dimensional photochemical-diffusive model of the hydrocarbon chemistry in Jupiter's upper atmosphere. The important chemical cycles and pathways among the C and C_2 species are outlined and it is shown that the amount of methane dissociation resulting from acetylene photochemistry is comparable to the amount that is due to direct photolysis. Profiles for the major observed hydrocarbon species are calculated and their sensitivity to eddy diffusion profile, chemistry, and solar UV flux is examined. A best fit to the eddy diffusion profile of the upper atmosphere during the *Voyager* encounters is found to be given by

$K = 1.3 \times 10^6 (2.17 \times 10^{13}/n)^{0.5}$ cm^2 s^{-1} (where n is the total number density), which implies a vertical mixing time at the tropopause of ~ 50 years. It is shown that polyacetylene formation driven by acetylene photochemistry in the models presented here is capable of producing the observed abundance of Danielson dust in the stratosphere of Jupiter. The disk-averaged Lyman-α albedo of the the preferred model is calculated to be ~ 8 kiloRayleighs, almost a factor of two lower than the *Voyager* observed value of ~ 14 kiloRayleighs. This may indicate the need for an increased flux of atomic hydrogen from the thermosphere over the already present source from EUV and soft electron dissociation of H_2. Such a flux is available from the auroral regions if there exists a pole-to-equator flow in the thermosphere as postulated earlier. Finally, a brief consideration of the auroral chemistry concludes that more lab studies of ion-neutral and ion-electron recombination reactions are needed before a meaningful study of that problem may be undertaken.

Table of Contents

Chapter 1

Radiative Transfer with Partial Frequency Redistribution in Inhomogeneous Atmospheres: Application to the Jovian Aurora

1.1 Introduction

There exist a large number of interesting radiative transfer (RT) problems in planetary atmospheres, such as ultraviolet reflection spectra, and auroral or dayglow emissions. These types of problems, although too complex for treatment by analytical or simple numerical methods, are not sufficiently well defined or important enough to justify using large and expensive computer codes for their solution, such as Monte Carlo methods. In this study, the method of Feautrier (1964) is developed for use in a finite difference program which is able to consider a variety of RT problems. This program is applied to the Lyman-α aurora of Jupiter at the end of this chapter. In Chapter 2 the program is used to model the UV reflection spectra of Jupiter and in Chapter 3 it is used to study the resonant reflection of the solar He 584 Å line by helium in the Jovian upper atmosphere.

The procedure developed here has been restricted to the case of plane-parallel atmospheres. The ability to analyze optically thick, inhomogeneous media with internal or external sources, isotropic or Rayleigh scattering phase functions, frequency redistribution (for an isotropically scattering phase function only), and a Lambert lower boundary has been maintained. The most general case considered in this work is that of angle-averaged partial frequency redistribution with external and internal sources of arbitrary frequency distribution and a Lambert-like monochromatically reflecting lower boundary. This case will be used to outline the method of solution. Results will be shown for various cases in which this model is compared with the results from more

elaborate models. New results will also be presented for the case of a Jovian Lyman-α aurora, demonstrating the effect of frequency redistribution on a line profile in a highly inhomogeneous atmosphere with an internal source at large optical depth.

1.2 Method of Solution

The equation of radiative transfer for an isotropic scattering phase function with frequency redistribution and both external and internal sources can be written as

$$\frac{\mu}{E(z,x)}\frac{dI}{dz}(z,\mu,x) = -I(z,\mu,x)$$

$$+ \frac{n^s(z)}{2E(z,x)}\int_{-\infty}^{+\infty} \sigma^s(z,x')\, r(z,x,x') \int_{-1}^{+1} I(z,\mu',x')\, d\mu'\, dx'$$

$$+ \frac{n^s(z)}{4E(z,x)}\int_{-\infty}^{+\infty} \sigma^s(z,x')\, r(z,x,x')\, F(x') \exp[-\int_{z}^{\infty} E(z,x')\, \frac{dz}{\mu_0}]\, dx'$$

$$+ \frac{V(z,x)}{4\pi E(z,x)}, \qquad (1.1)$$

where $z \equiv$ height; $\mu \equiv$ cosine of zenith angle; $x \equiv$ frequency in Doppler units from line center $= (\nu - \nu_0)/\Delta\nu_D$ (where $\nu_0 \equiv$ line center frequency, $\Delta\nu_D = \frac{\nu_0}{c}\sqrt{2kT/m}$, $T \equiv$ temperature, and $m \equiv$ mass of scattering particle); $I(z,\mu,x) \equiv$ specific intensity (usually in photons $cm^{-2}\, s^{-1}\, sr^{-1}\, \Delta\nu_D^{-1}$); $E(z,x) = n^s(z)\, \sigma^s(z,x) + n^a(z)\, \sigma^a \equiv$ total extinction per unit path length; $n^s(z) \equiv$ number density of scattering particles; $n^a(z) \equiv$ number density of absorbing particles; $\sigma^s(z,x) \equiv$ scatterer cross-section; $\sigma^a \equiv$ absorber cross-section (assumed constant); $r(z,x,x') \equiv$ frequency redistribution function, defined as R (see Hummer, 1962) divided by the normalized Voigt function;

$\pi F(x) \equiv$ external source flux; $-\mu_0 \equiv$ cosine of external source zenith angle; and $V(z,x) \equiv$ total emission rate of internal source (the internal source is assumed to be isotropic).

The second term on the right-hand side of Equation (1.1) is the contribution to the source function in the direction μ at a frequency x due to scattering from all directions μ' and all frequencies x', all at a level z. The third term on the right is the contribution to the source function from the external flux of all frequencies x' that penetrate to the level z, and are then scattered into direction μ and frequency x. The fourth term on the right is due to an isotropically emitting internal source. Such an internal source could be used to represent aurorae or dayglow, for example.

This equation is solved by the Feautrier method, as described by Mihalas (1978). To start the solution, Equation (1.1) is first separated into upward and downward streams. We define j as the mean intensity and h as one half the net intensity along a given direction; then,

$$j(z,\mu,x) = \frac{1}{2}[I^+(z,\mu,x) + I^-(z,\mu,x)] , \tag{1.2}$$

$$h(z,\mu,x) = \frac{1}{2}[I^+(z,\mu,x) - I^-(z,\mu,x)] . \tag{1.3}$$

Equation (1.1) may be rewritten as

$$\frac{\mu}{E}\frac{dh}{dz} = -j + \frac{n^s}{E}\int_{-\infty}^{+\infty} \sigma^s \tau \int_0^1 j \, d\mu' \, dx'$$

$$+ \frac{n^s}{4E}\int_{-\infty}^{+\infty} \sigma^s \tau F \exp\left(-\int_z^{\infty} E \frac{dz}{\mu_0}\right) dx' + \frac{V}{4\pi E} , \tag{1.4}$$

$$\frac{\mu}{E}\frac{dj}{dz} = -h , \tag{1.5}$$

where explicit dependences have been dropped. Combining these equations

yields a second-order differential integral equation in j, the quantity that will be solved for, viz.

$$\left(\frac{\mu^2}{E^2}\right)\frac{d^2j}{dz^2} - \left(\frac{\mu^2}{E^3}\frac{dE}{dz}\right)\frac{dj}{dz} - j + \frac{n^s}{E}\int_{-\infty}^{+\infty} \sigma^s \tau \int_0^1 j \, d\mu' \, dx'$$

$$= -\frac{n^s}{4E}\int_{-\infty}^{+\infty} \sigma^s \tau F \exp\left(-\int_z^{\infty} E \frac{dz}{\mu_0}\right) dx' - \frac{V}{4\pi E}. \qquad (1.6)$$

The procedure is to discretize this equation in the three independent variables z, μ, and x, using log divisions in z, Gaussian divisions in μ, and even divisions in x. The integrations in x are only performed over the range $-x^*$ to $+x^*$ where x^* is an adjustable parameter. In discretized form, Equation (1.6) becomes

$$\frac{\mu_n^2}{E_{lm}^2}\left[\frac{2j_{l-1mn}}{\Delta_{l-1}(\Delta_{l-1}+\Delta_l)} - \frac{2j_{lmn}}{\Delta_{l-1}\Delta_l} + \frac{2j_{l+1mn}}{\Delta_l(\Delta_{l-1}+\Delta_l)}\right]$$

$$-\frac{\mu_n^2}{E_{lm}^3}\left(\frac{dE}{dz}\right)_{lm}\left[\frac{j_{l-1mn}}{(\Delta_{l-1}+\Delta_l)} - \frac{j_{l+1mn}}{(\Delta_{l-1}+\Delta_l)}\right]$$

$$-j_{lmn} + \frac{n_l^s}{2E_{lm}}\sum_{m'=1}^{M} b_{m'}\sigma_{lm'}^s \tau_{lmm'}\sum_{n'=1}^{N} a_{n'} j_{lm'n'}$$

$$= -\frac{n_l^s}{4E_{lm}}\sum_{m'=1}^{M} b_{m'}\sigma_{lm'}^s \tau_{lmm'} F_{m'} \exp\left(-\sum_{l'=1}^{l-1} E_{l'm'}\frac{\Delta_{l'}}{\mu_0}\right) - \frac{V_{lm}}{4\pi E_{lm}}, \qquad (1.7)$$

where l, m, and n are the indices for z, x, and μ, respectively, and $\Delta_l = z_l - z_{l+1}$. The integrals over over x' and μ' have been replaced with their discrete equivalents, i.e.,

$$\int_{-\infty}^{+\infty} f(x')\,dx' \approx \int_{-x^*}^{+x^*} f(x')\,dx' = \sum_{m'=1}^{M} b_{m'} f(x_{m'}) \qquad (1.8)$$

and

$$\int_0^{+1} g(\mu')\, d\mu' = \frac{1}{2}\int_{-1}^{+1} g\left(\frac{q+1}{2}\right) dq = \frac{1}{2}\sum_{n'=1}^{N} a_{n'}\, g\left(\frac{q_{n'}+1}{2}\right), \qquad (1.9)$$

with a_n' and q_n' representing the Gaussian weights and divisions on the interval [-1,+1] for direction, and with b_m' and x_m' representing even weights and divisions on the interval $[-x^*,+x^*]$ for frequency.

To simplify the rest of the derivation (and the programming), the indices for x and μ (m and n) are combined into one index k. This new index will run through $K = M \times N$ values. After rearranging Equation (1.7) in terms of l, the following equation is obtained:

$$\sum_{k'=1}^{K} \left\{\frac{\mu_{k'}^2}{E_{lk'}^2 (\Delta_{l-1} + \Delta_l)}\left[\frac{2}{\Delta_{l-1}} - \frac{1}{E_{lk'}}\left(\frac{dE}{dz}\right)_{lk'}\right]\right\} \delta_{kk'}\, j_{l-1k'}$$

$$+ \sum_{k'=1}^{K} \left[\left(-2\frac{\mu_{k'}^2}{E_{lk'}^2\, \Delta_{l-1}\Delta_l} - 1\right)\delta_{kk'} + \frac{n_l^s}{2E_{lk}}\, a_{k'}\, b_{k'}\, \sigma_{lk'}^s\, \tau_{lkk'}\right] j_{lk'}$$

$$+ \sum_{k'=1}^{K} \left\{\frac{\mu_{k'}^2}{E_{lk'}^2 (\Delta_{l-1} + \Delta_l)}\left[\frac{2}{\Delta_l} + \frac{1}{E_{lk'}}\left(\frac{dE}{dz}\right)_{lk'}\right]\right\} \delta_{kk'}\, j_{l+1k'}$$

$$= -\frac{n_l^s}{4E_{lk}} \sum_{k'=1}^{K} b_{k'}\, \sigma_{lk'}^s\, \tau_{lkk'}\, F_{k'} \exp\left(-\sum_{l'=1}^{l-1} E_{l'k'}\, \frac{\Delta_{l'}}{\mu_0}\right) - \frac{V_{lk}}{4\pi E_{lk}}. \qquad (1.10)$$

This equation has the form

$$A_{lkk'}\, j_{l-1k'} + B_{lkk'}\, j_{lk'} + C_{lkk'}\, j_{l+1k'} = G_{lk}, \qquad (1.11)$$

which is a tridiagonal system of equations in j. Upper and lower boundary conditions must now be applied to this system to obtain a unique solution.

The upper boundary condition for most problems is that the downward diffuse flux is zero, i.e.,

$$I^-(z_{max},\mu,x) = 0 , \tag{1.12}$$

where z_{max} corresponds to zero optical depth.

By definition, $I^- = j - h$ and, using Equation (1.5), the upper boundary condition becomes

$$j_{1k} + \frac{\mu_k}{E_{1k}}\left(\frac{dj}{dz}\right)_{1k} \approx j_{1k} + \frac{\mu_k}{E_{1k}\Delta_1}(j_{1k} - j_{2k}) = 0 \tag{1.13}$$

so that $B_{1kk'} = (1 + \frac{\mu_{k'}}{E_{1k'}\Delta_1})\,\delta_{kk'}$, $C_{1kk'} = -\frac{\mu_{k'}}{E_{1k'}\Delta_1}\delta_{kk'}$, and $G_{1k} = 0$. For the lower boundary, a monochromatic Lambert reflecting surface of albedo λ is simulated, i.e.,

$$I^+(z_{min},\mu,x) = \lambda\, F_{inc}\,(z_{min},x) , \tag{1.14}$$

where $F_{inc}(z_{min},x) = \mu_0\, F(x)\, \exp[-\int_{z_{min}}^{\infty} E(z,x)\frac{dz}{\mu_0}] + 2\int_0^1 \mu'\, I^-\,(z_{min},\mu',x)\, d\mu'$.

The second term in F_{inc} is approximated by $I^-\,(z_{min},\mu,x)$, which is actually only a good approximation in media that are optically thick enough that $I^-\,(z_{min},\mu,x)$ is a very weak function of μ. With this approximation, the lower boundary condition becomes

$$I^+\,(z_{min},\mu,x) - \lambda I^-\,(z_{min},\mu,x) = \lambda\mu_0\, F\, \exp(-\int_{z_{min}}^{\infty} E\,\frac{dz}{\mu_0}) . \tag{1.15}$$

To convert this into terms in j, the relations

$$I^+(z_{min},\mu,x) = j_{Lk} - \frac{\mu_k}{E_{Lk}}\left(\frac{dj}{dz}\right)_{Lk} \approx j_{Lk} - \frac{\mu_k}{E_{Lk}\Delta_{L-1}}(j_{L-1k} - j_{Lk}) \tag{1.16}$$

and

$$I^-(z_{min},\mu,x) = j_{Lk} + \frac{\mu_k}{E_{Lk}}\left(\frac{dj}{dz}\right)_{Lk} \approx j_{Lk} + \frac{\mu_k}{E_{Lk}\Delta_{L-1}}(j_{L-1k} - j_{Lk}) \tag{1.17}$$

are used. Substitution of these relations into Equation (1.15) yields

$A_{Lkk'} = -(1-\lambda)\,\mu_{k'}\,\delta_{kk'}/E_{Lk'}\,\Delta_{L-1}$, $B_{Lkk'} = (1-\lambda)(1 + \frac{\mu_{k'}}{E_{Lk'}\,\Delta_{L-1}})\,\delta_{kk'}$, and

$$G_{lk} = \lambda\mu_0 F_k \exp(-\sum_{l'=1}^{L-1} E_{l'k} \frac{\Delta_{l'}}{\mu_0}) .$$

The tridiagonal system of matrix equations is now complete and may be solved using the method outlined in Mihalas (1978). Although this was the basic method used, refinements have been made in the application of the boundary conditions and in calculating the attenuated external flux.

For cases in which it is not necessary to consider frequency redistribution, the solution may be simplified by dropping τ and the integrals over x in Equation (1.1) and by dropping all dependences on x. Then $d\tau = -Edz$ and $\tilde{\omega}_0 = \sigma_s n_s / E$ and Equation (1.1) would be the ordinary equation of radiative transfer for isotropic scattering in an inhomogeneous medium. By specifying an isotropic scattering phase function, dependences on azimuth are removed. However, for the case of no frequency redistribution (i.e., monochromatic scattering), a Rayleigh phase function may be treated by expanding all azimuthally varying quantities in a cosine series of the azimuth angle, i.e.,

$$I(\tau,\mu) = I^{(0)}(\tau,\mu) + I^{(1)}(\tau,\mu)\cos(\varphi - \varphi_0) + I^{(2)}(\tau,\mu)\cos 2(\varphi - \varphi_0) . \qquad (1.18)$$

The Rayleigh phase function $p(\Theta) = \frac{3}{4}(1 + \cos^2\Theta)$, where Θ is the scattering angle, may be expanded via

$$\cos\Theta = \mu\mu' + \sqrt{(1-\mu^2)(1-\mu'^2}\cos(\varphi - \varphi') \qquad (1.19)$$

into the function

$$p(\mu,\varphi;\mu',\varphi') = p^{(0)}(\mu,\mu') + p^{(1)}(\mu,\mu')\cos(\varphi - \varphi') + p^{(2)}(\mu,\mu')\cos 2(\varphi - \varphi') , \qquad (1.20)$$

where

$$p^{(0)}(\mu,\mu') = p^{(0)}(-\mu,\mu') = \frac{3}{8}(3 - \mu^2 + (3\mu^2 - 1)\mu'^2) , \tag{1.21}$$

$$p^{(1)}(\mu,\mu') = -p^{(1)}(-\mu,\mu') = \frac{3}{2}\mu\mu'\sqrt{(1 - \mu^2)(1 - \mu'^2)} , \tag{1.22}$$

and

$$p^{(2)}(\mu,\mu') = p^{(2)}(-\mu,\mu') = \frac{3}{8}(1 - \mu^2 + (\mu^2 - 1)\mu'^2) . \tag{1.23}$$

This procedure allows the equation of transfer to be split into three equations in $\cos m(\varphi - \varphi_0)$. The zeroth and second order equations in $\cos m(\varphi - \varphi_0)$ may be solved for j in the same way as outlined above. The first order equation, because of the anti-symmetry in $\pm\mu$, is easier to solve for h than j.

Figures 1.1 and 1.2 show how the Feautrier method program (hereafterward referred to as the FMP) compares with the invariant imbedding program of Hansen (see Sato et al., 1975 for a description of the invariant imbedding method). Figure 1.1 shows the comparison for both isotropic and Rayleigh scattering phase functions in homogeneous atmospheres of total optical depth $\tau_{max} = 10^2$, for various single-scattering albedos $\tilde{\omega}_0$. The Lambert-scattering ground albedo $\lambda = 1$ in these examples, but because of the large optical depth, it only affects the calculated intensities for $\tilde{\omega}_0 = 1$, which are shown as asymptotic values. The geometric albedo p is the quantity that would be observed of a planet having this atmosphere at zero phase angle (i.e., it is a weighted sum of all intensities with $\mu = \mu_0$). The agreement between all cases of homogeneous atmospheres shown here is seen to be almost exact.

Figure 1.2 shows the comparison for both isotropic and Rayleigh scattering phase functions in highly inhomogeneous atmospheres of total optical depth $\tau_{max} = 10^4$ for various emission angles. Two different functional dependences of $\tilde{\omega}_0(\tau)$ were chosen. In the first case $\tilde{\omega}_0(\tau)$ was chosen to vary from 1 to 0 with increasing log τ and in the second case $\tilde{\omega}_0(\tau)$ was chosen to vary

Figure 1.1

(a) Dependence of I^+ / F (for $\mu=\mu_0=1$ and $\mu=\mu_0=0.5$) and geometric albedo p on the single-scattering albedo $\tilde{\omega}_0$ in an isotropically-scattering atmosphere ($\tau_{max}=100$) with a Lambert-reflecting lower boundary ($\lambda=1$). Solid lines: results of Invariant Imbedding method. Open triangles: FMP results.

(b) The same as (a), using a Rayleigh phase function.

Figure 1.2

(a) Dependence of I^+ / F on μ for $\mu_0=1$ in an isotropically-scattering atmosphere ($\tau_{max}=10^4$) using two different functional forms for $\tilde{\omega}_0(\tau)$, both highly inhomogeneous. Filled circles represent both FMP and invariant imbedding method results (they are indistinguishable at this resolution). Solid lines are interpolated.

(b) The same as (a), using a Rayleigh phase function.

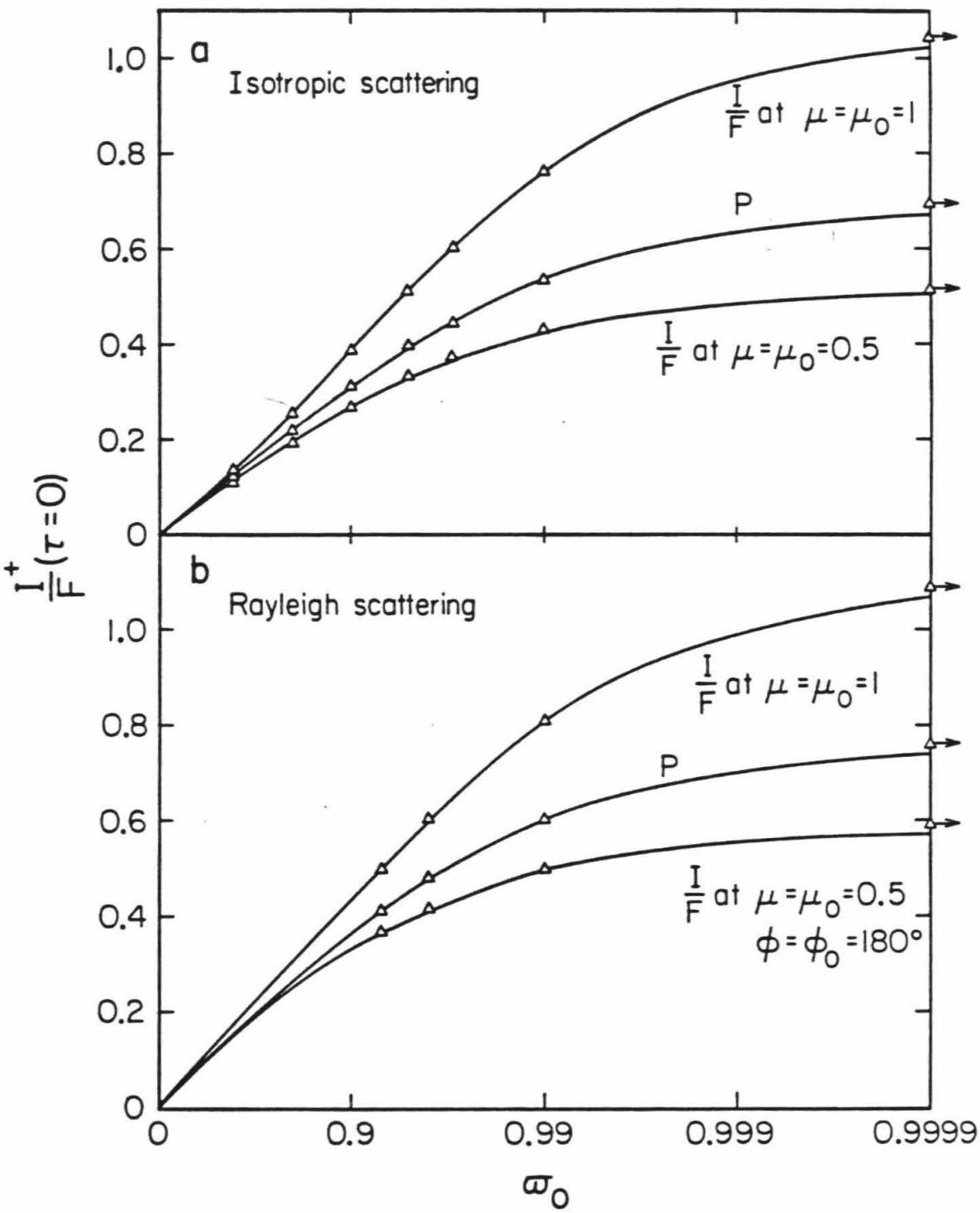
a
Isotropic scattering
$\frac{I}{F}$ at $\mu=\mu_0=1$
P
$\frac{I}{F}$ at $\mu=\mu_0=0.5$
b
Rayleigh scattering
$\frac{I}{F}$ at $\mu=\mu_0=1$
P
$\frac{I}{F}$ at $\mu=\mu_0=0.5$
$\phi=\phi_0=180°$
$\frac{I^+}{F}(\tau=0)$
ω_0
0
0.2
0.4
0.6
0.8
1.0
0.9
0.99
0.999
0.9999

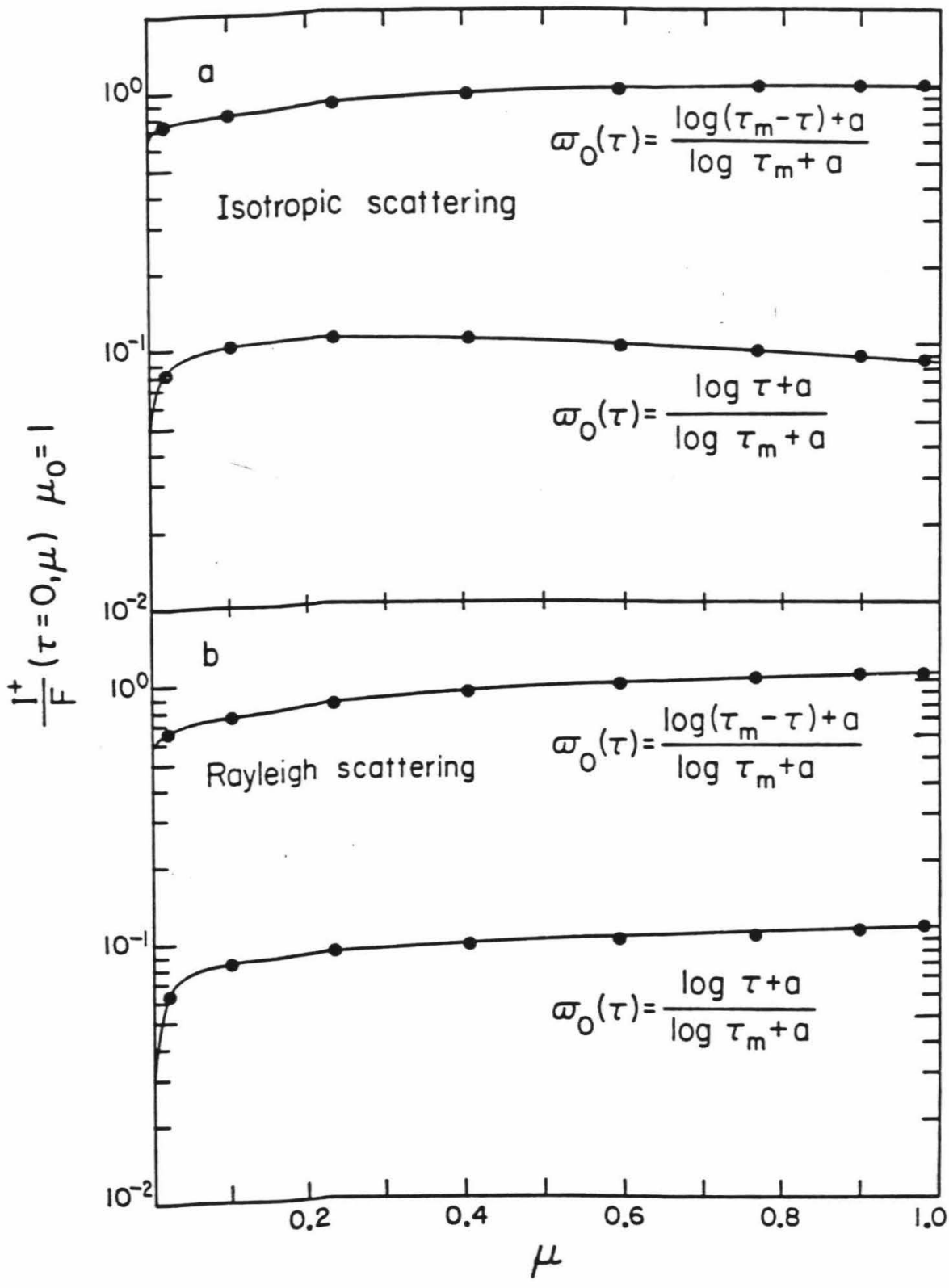
a
10^0
$\varpi_0(\tau) = \frac{\log(\tau_m - \tau) + a}{\log \tau_m + a}$
Isotropic scattering
10^{-1}
$\varpi_0(\tau) = \frac{\log \tau + a}{\log \tau_m + a}$
10^{-2}
b
10^0
Rayleigh scattering
$\varpi_0(\tau) = \frac{\log(\tau_m - \tau) + a}{\log \tau_m + a}$
10^{-1}
$\varpi_0(\tau) = \frac{\log \tau + a}{\log \tau_m + a}$
10^{-2}
0.2
0.4
0.6
0.8
1.0
μ
$\frac{I^+}{F}(\tau = 0, \mu)$ $\mu_0 = 1$

from 0 to 1 with increasing log τ. The actual formulas used in the two cases were

$$\tilde{\omega}_0(\tau) = \frac{\log(\tau_{max} - \tau) + a}{\log\tau_{max} + a} \tag{1.24}$$

and

$$\tilde{\omega}_0(\tau) = \frac{\log\tau + a}{\log\tau_{max} + a}, \tag{1.25}$$

respectively, where $a = 4.157$. Identical sets of data were used in the FMP and in the invariant imbedding program of Hansen. The FMP almost consistently yields slightly higher intensities than Hansen's method. The differences are everywhere less than 3%. The average CPU time used by the FMP in solving one of these atmospheres for a Rayleigh scattering phase function, 100 layers in τ, and 8 Gaussian angles per hemisphere was ~3.8 seconds on an IBM 370/3032 computer. The CPU time scales linearly with the number of layers and quadratically with the number of angles.

1.3 Frequency Redistribution Functions

A photon emitted near line center deep in an optically-thick atmosphere will undergo a large number of scatterings before it can escape. Generally, each scattering will result in a shift in the photon's frequency due to the Doppler effect. This process, known as frequency redistribution, complicates the radiative transfer problem by coupling the optically thick core of a line with its optically thin wings. Its proper treatment requires the use of a function that is dependent on the frequency and direction of the photon before and after scattering. Many approximations to this function can be made. The best approximation that the FMP can currently handle is a redistribution function that is averaged over the scattering angle of the photon. For the derivation of many physically meaningful frequency redistribution functions, an excellent

treatment of the problem is given by Hummer (1962). The rest of this chapter deals with the effects of frequency redistribution in optically thick resonance lines and attempts to model them. It will be seen that the frequency redistribution function used will dramatically affect the derived line profiles.

The FMP solution allows for the use of arbitrary frequency redistribution functions. For practical purposes, only three were used in this work. They are (i) monochromatic scattering (MS), (ii) Voigt complete redistribution (VCR) (i.e., no dependence on pre-scattered photon frequency), and (iii) angle-averaged partial redistribution (AAPR), where the notation of Lee and Meier (1980) has been adopted. The normalization of the frequency redistribution function is such that

$$\int_{-\infty}^{+\infty} r(z,x,x')\Phi(a,x')\,dx' = \Phi(a,x)\,; \tag{1.26}$$

$\Phi(a,x)$ is the normalized Voigt function

$$\Phi(a,x) = \frac{a}{\pi^{3/2}}\int_{-\infty}^{+\infty} \frac{e^{-y^2}}{a^2 + (x-y)^2}\,dy\,, \tag{1.27}$$

where a is the ratio of the natural width of the line to the Doppler width. This normalization was enforced at the expense of bending the shape of r (see Adams et al., 1971).

(i) For MS,

$$r(z,x,x') = \delta(x - x')\,, \tag{1.28}$$

where $\delta(x)$ is the Dirac delta-function.

(ii) For VCR,

$$r(z,x,x') = \Phi(a,x)\,; \tag{1.29}$$

it should be noted that, in general, a will vary with z (i.e., the temperature of the atmosphere varies with z).

(iii) For AAPR,

$$\tau(z,x,x') = \frac{\Phi(a,x)}{\Phi(a,x')} \frac{R(z,x,x')}{\int_{-\infty}^{+\infty} R(z,x,x')\,dx'} \quad , \tag{1.30}$$

where

$$R(z,x,x') = \int_0^{\pi} \exp\{-[\frac{x-x'}{2\sin(\Theta/2)}]^2\}\,\Phi(a\sec(\Theta/2), \frac{(x+x')}{2}\sec(\Theta/2))\,d\Theta \tag{1.31}$$

and $\cos\Theta = \mu\mu' + \sqrt{(1-\mu^2)(1-\mu'^2)}\cos(\varphi - \varphi')$ is the scattering angle as before.

1.4 Results

To test the frequency redistribution model, an attempt was made to match the results obtained by Lee and Meier (1980) and by Meier and Lee (1981), who used a Monte Carlo technique, for both external and internal sources.

1.4.1 External Sources

In Figure 1.3, we compare FMP results with those of Lee and Meier (1980) for the external source case. The atmosphere has uniform composition and is purely scattering (i.e., n^s is constant and $n^a = 0$), with total optical depth at line center $\tau_{max} = 10^4$ and $a = 2 \times 10^{-3}$. It is illuminated from above at an angle $\mu_0 = 1$ by a uniform flux of πF (photons $cm^{-2}\ sec^{-1}\ \Delta\nu_D^{-1}$) with $F = 1$. The FMP model has 149 layers in z (chosen such that $\Delta\tau_{\nu_0} = \sigma^s_{\nu_0} n^s \Delta$ decreases logarithmically from the center of the atmosphere towards either boundary), 2 Gaussian angles in the range $0 < \mu_n < 1$, and 25 Gaussian frequencies in the range $0 < x_m < 12.5$.

The FMP yields specific intensities and, to convert to the emission rate of Lee and Meier (1980), these intensities were multiplied by $8/\sqrt{\pi}$. Figure 1.3a shows the comparison between the FMP and Lee and Meier's for the case of VCR, and Figure 1.3b shows the comparison between the FMP and Lee and Meier's for

Figure 1.3

Profiles of emission rate at μ=1 plotted against frequency for an isotropically-scattering conservative atmosphere (τ_{max}=10^4) with an external source (μ_0=1) .

(a) Results of Lee and Meier (1980) for VCR case (solid lines). The upper curve corresponds to the source side, the lower curve corresponds to the anti-source side. Open triangles: FMP results, solid lines are interpolated.

(b) Results of Lee and Meier (1980) for AAPR case. The open circles correspond to the source side, the filled circles correspond to the anti-source side. Open triangles: FMP results, solid lines are interpolated.

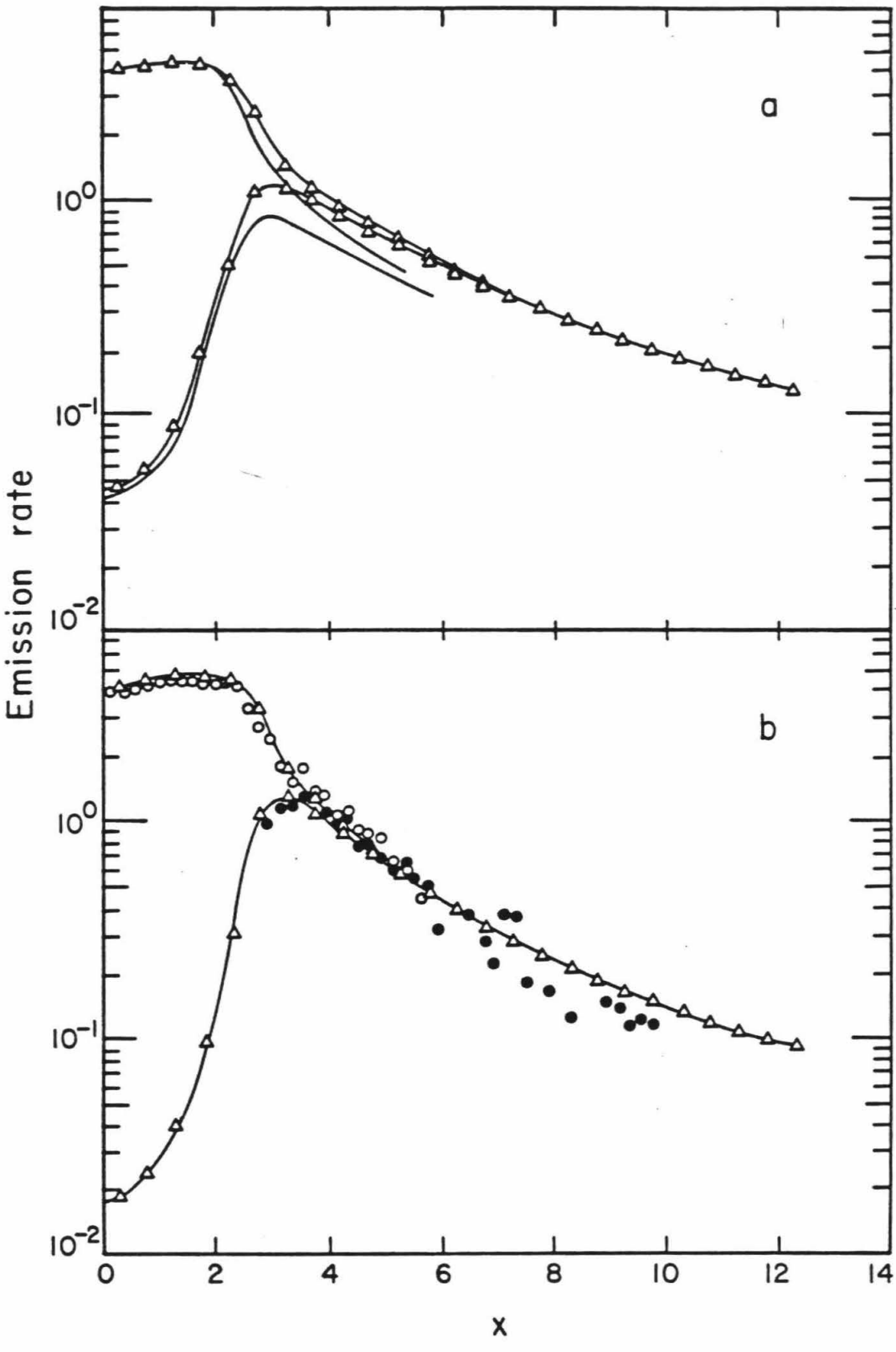
a
b
Emission rate
10^{0}
10^{-1}
10^{-2}
0
2
4
6
8
10
12
14
X

the case of AAPR. The disagreement outside the core in Figure 1.3a is due to different choices in x^* between the two models. In Figure 1.3b, the agreement is quite good out to $x \approx 6$ (maximum difference $\approx$ 30%). At $x > 6$, the Monte Carlo results become noisy, and the comparison is not as good (maximum difference $\approx$ 60%). The overall fit to the AAPR case is quite reasonable, especially since the FMP program took 650 seconds of CPU time on an IBM 370/3032 while Lee and Meier's program took 51100 seconds of CPU time on a CDC 6400, although admittedly their results have much better frequency coverage.

1.4.2 Internal Sources

Using the same atmosphere as for the external source case (i.e., $\tau_{max} = 10^4$, uniform, and $a = 2 \times 10^{-3}$), the external source is turned off and a uniform isotropic internal source

$$\frac{V(z,x)}{4\pi} = \frac{\Phi(a,x)}{4\pi} (\text{ph cm}^{-3}\,\text{sec}^{-1}\,\text{sr}^{-1}\,\Delta\nu_D^{-1}) \tag{1.32}$$

is turned on.

Figure 1.4 demonstrates the comparison between the FMP results and those of Meier and Lee (1981). The comparisons are for both VCR and AAPR. This time, however, the intensity as a function of frequency is compared for one boundary of the atmosphere (either one, since the problem is symmetrical) and for the middle of the atmosphere. This time the comparison for the VCR approximation (Figures 1.4a and 1.4b) is very good overall, with the FMP results for this case everywhere close to Meier and Lee's result. The intensity at the center (Figure 1.4b) seems to be overestimated a little by the FMP. For the case of AAPR, the comparison is good for the boundary (Figure 1.4c) out to $x \approx 3$, and the center (Figure 1.4d) everywhere, but the FMP values for $x > 3$ at the

Figure 1.4

Profiles of emission rate at μ=1 plotted against frequency for an isotropically-scattering conservative atmosphere (τ_{max}=10^4) with a uniform internal source which is isotropic and has a Voigt frequency profile; (a) and (c) show profiles at the boundary of the atmosphere, while (b) and (d) show profiles at the center of the atmosphere. Results of Meier and Lee (1981) are shown in (a) and (b) for the VCR case (crosses) and in (c) and (d) for the AAPR case (diamonds). FMP results for the same cases are plotted as filled circles with solid line interpolations.

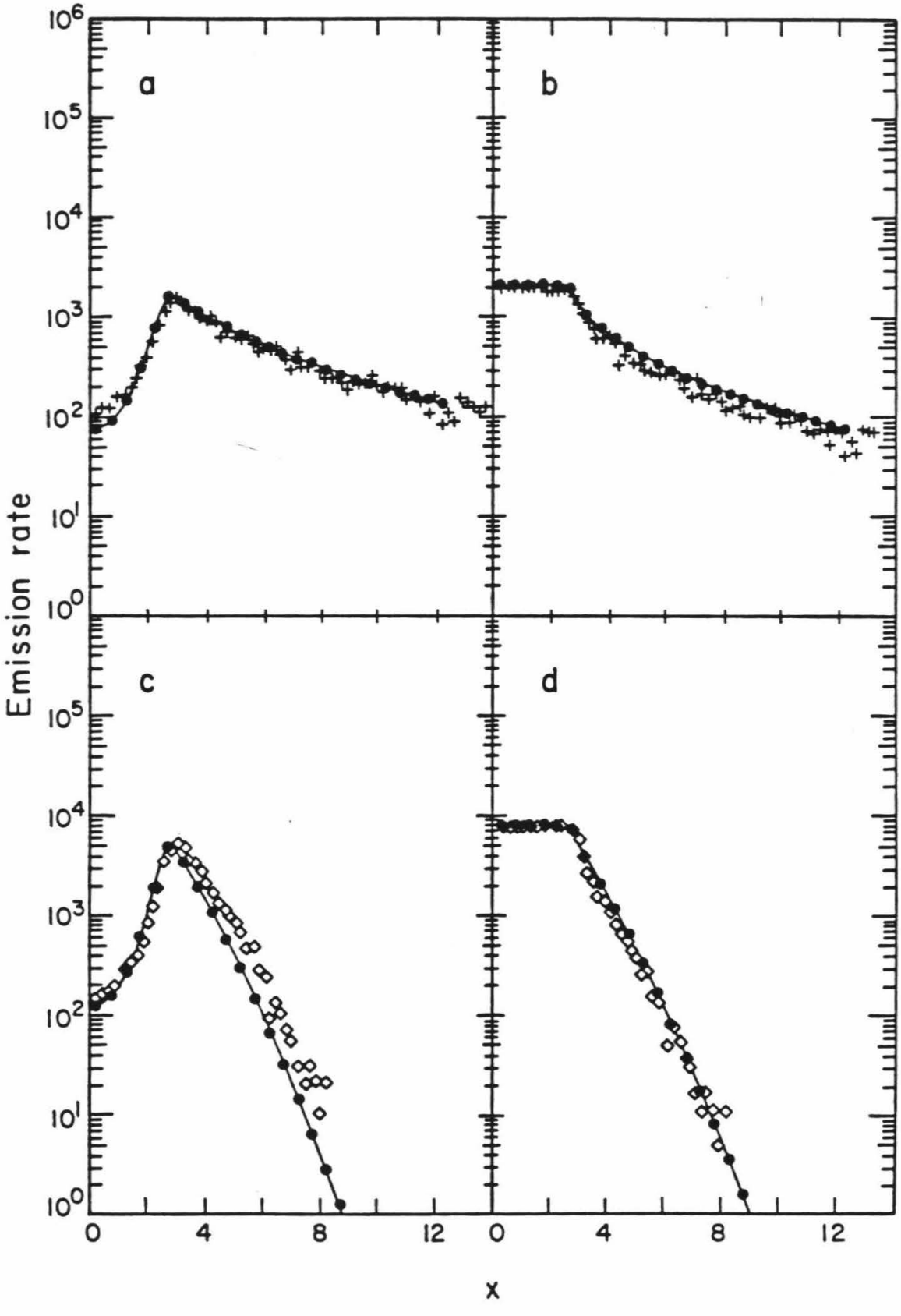
a
b
c
d
Emission rate
x
10^6
10^5
10^4
10^3
10^2
10^1
10^0
0
4
8
12

boundary fall off more quickly than the values of Meier and Lee. This result has been checked many times, since the error at $x = 7$ is a factor of ~ 2, but so far the two models cannot be reconciled. Overall, however, the comparison is fairly good. To test the FMP in a practical situation, the case of the Lyman- α aurora on Jupiter is now considered.

1.5 Jupiter Lyman-alpha Aurora

Lyman alpha aurorae on Jupiter have been observed by the ultraviolet spectrometer (*UVS*) experiments of both *Voyager* spacecraft (Sandel et al., 1979), and by the *International Ultraviolet Explorer* (*IUE*) satellite (Clarke et al., 1980; Durrance et al., 1982). The brightness of the aurora is quite variable, but it is typically around 20-40 kR (1 kR = 10^9 photons cm^{-2} sec^{-1}). The source of excitation for the aurora is likely to be energetic particle precipitation. These particles excite a number of UV emissions, most notably Lyman-α, and the Lyman and Werner bands. By studying the color ratios of the observed spectrum we can determine the mean energy of the particles. This is possible because the more energetic a particle is, the deeper into the Jovian atmosphere it penetrates, and if it makes it down to beneath the homopause, the short wavelength emissions will be partially absorbed by hydrocarbons. The phenomenon of frequency redistribution makes the Lyman alpha aurora a special case, however, since a Lyman alpha photon that is created near line center at great optical depth will escape much more easily if it moves out into the less optically thick wings of the line. In general, frequency redistribution allows more photons to escape and greatly modifies the line profile.

To study the Jovian aurora, a model upper atmosphere for Jupiter was constructed which contains the height profiles of H_2, H, and CH_4. These profiles are based on a value of 3.0×10^6 cm^2 sec^{-1} for the eddy diffusion coefficient at

the homopause (K_h). In Chapter 3 it will be shown that the most realistic value for the equatorial value of K_h at the time of the *Voyager* encounters is $\sim 1.3 \times 10^6$ cm^2 sec^{-1}. If the eddy diffusion for the auroral region were the same as that for the equatorial region, this difference would mean that in the model profile used here there is an excess of CH_4 in the upper atmosphere. Since the actual auroral eddy diffusion profile is unknown, we feel that the chosen profile is realistic enough for demonstration purposes. Likewise, the temperature profile was taken from the Festou et al. (1981) results for the equatorial region. The gravity was taken to be 2640 cm sec^{-2} using formulas found in Anderson (1976) for 65° north.

The optical properties of this atmosphere are shown in Figure 1.5. This figure shows the quantity $1 - \tilde{\omega}_0$ as a function of height above the tropopause at line center as well as 3, 8, and 30 Doppler units from line center. The significant high inhomogeneity in this atmosphere is due to the rapidly decreasing mixing ratio of methane (the principal absorber of Lyman-α) near the homopause (around 400 km or $P \sim 7 \times 10^{-7}$ bars). Into this atmosphere, a monoenergetic beam of electrons was input at a zenith angle of 0.5, simulating a hemispherically-isotropic distribution. Figure 1.6 shows the height profiles for the volume production rate of Lyman-α photons by a 1 erg cm^{-2} sec^{-1} flux of primary electrons of 1, 10, and 100 keV. These profiles were generated using the continuous loss approximation (see Appendix) with the loss function for H_2 taken from Cravens et al. (1975) and the cross-sections for production of H(2s) and H(2p) from the dissociative excitation of H_2 (the principal source of Lyman-α) were the same as those used in Yung et al. (1982a). The effect of the electron beam on the height profiles of H_2, H, and CH_4 was not considered, so that an implicit assumption made here is that the profiles are not altered by the auroral chemistry. This assumption would be valid, for instance, if the horizontal

Figure 1.5

Height profiles of $1 - \tilde{\omega}_0$ in the model Jovian atmosphere for four different frequencies in the Lyman-α line profile. Altitudes are measured from the tropopause. Total optical depths are also indicated for each frequency at ~ 500 km.

Figure 1.6

Height profiles of the line-integrated volume production rate of Lyman-α photons in the model Jovian atmosphere resulting from the dissociative excitation of H_2 by a beam of primary electrons of energy E.

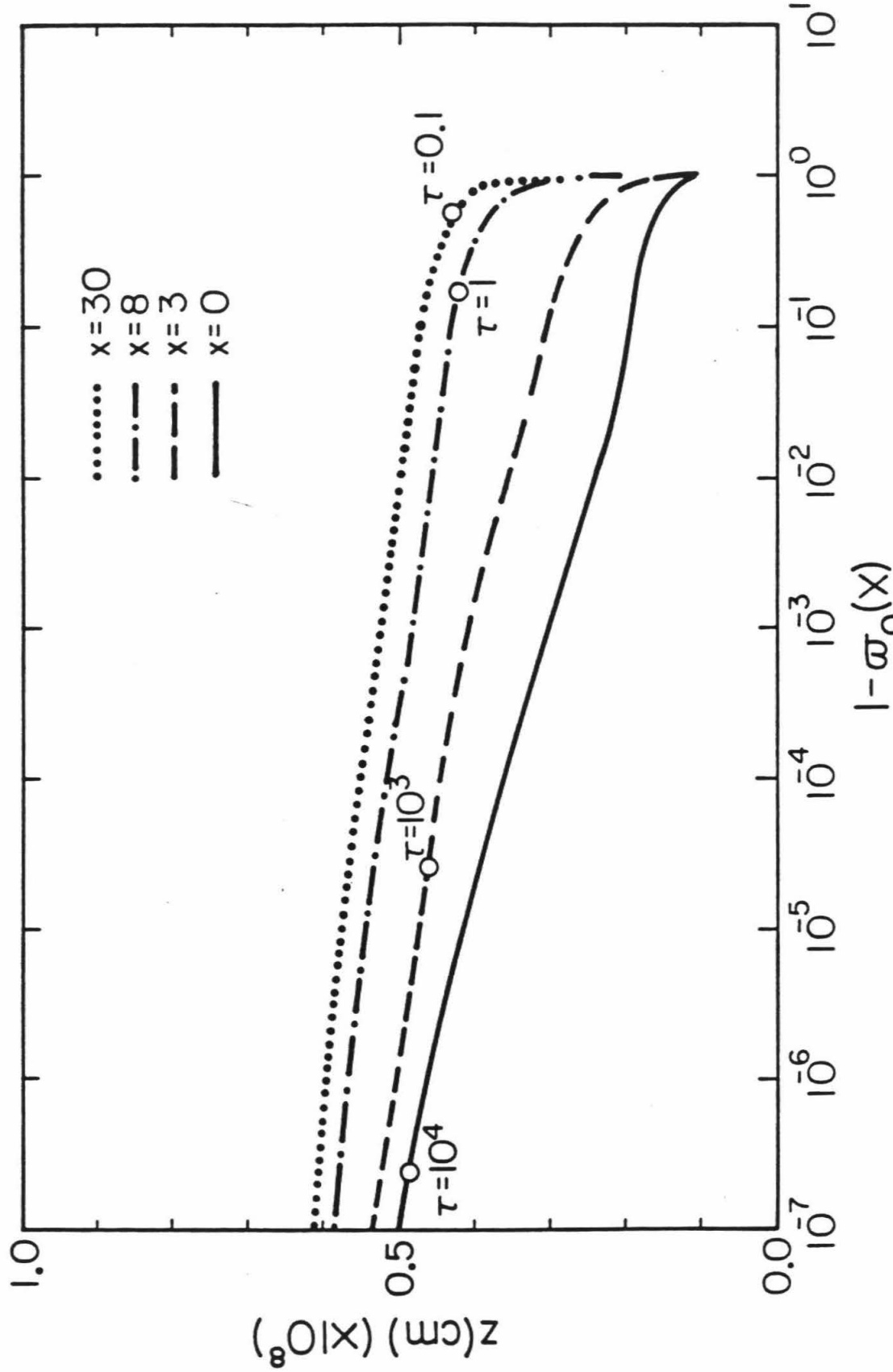
x=30
x=8
x=3
x=0
τ=0.1
τ=1
τ=10
τ=10⁴
z(cm) (x10⁸)
1.0
0.5
0.0
10⁻⁷
10⁻⁶
10⁻⁵
10⁻⁴
10⁻³
10⁻²
10⁻¹
10⁰
10¹
1-ϖ₀(X)

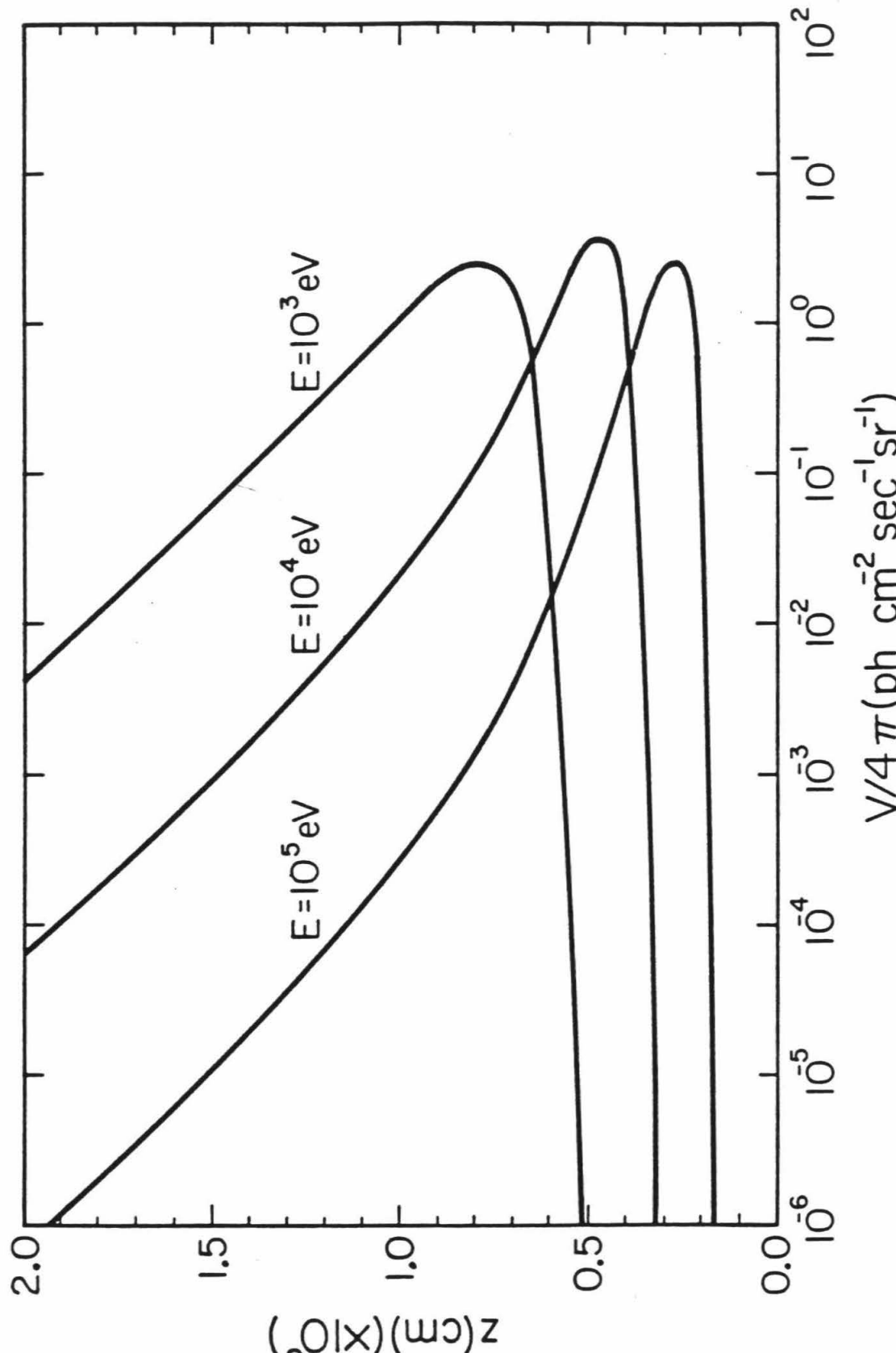
E=10^3 eV
E=10^4 eV
E=10^5 eV
z(cm)(x10^8)
2.0
1.5
1.0
0.5
0.0
10^-6
10^-5
10^-4
10^-3
10^-2
10^-1
10^0
10^1
10^2
V/4π(ph cm^-2 sec^-1 sr^-1)

transport from non-auroral regions were large enough to dilute the local effects of the beam. Figure 1.7 displays the emission line profiles that would be generated by the three internal source distributions shown in Figure 1.6. The optically thin approximation shows the basic shape of the internal source frequency dependence. When an H_2 molecule is dissociated, the excited H fragments carry away a substantial amount of kinetic energy and the distribution of kinetic energies translates into the frequency dependence of the source. The distribution of kinetic energies for the H(2p) and H(2s) fragments were taken from the calculations of Lee (1981) and Lee et al. (1982). Also shown are the FMP results for MS, AAPR, and VCR cases.

The peculiar shape of the MS profiles are due to the following physical processes. At frequencies greater than $x \approx 8$ the atmosphere is optically thin. Here x is defined as one Doppler unit at Lyman-α at a temperature of 150 K. In the region $3 < x < 8$, the column of H above the main source region becomes optically thick to scattering. This traps photons so that they have a much larger chance of being absorbed by hydrocarbons and as a result the emission in this frequency range is lower. In the region $0 < x < 3$, the photons are still trapped, but the probability of being absorbed by a hydrocarbon is much less than the probability of being scattered (i.e., $1 - \tilde{\omega}_0 \sim 10^{-2}$ or less), so that the emission in this region starts to increase again.

Frequency redistribution has the effect of transferring photons from the $x < 7$ region out to the $x \approx 7$ region. The effects on the line profiles are quite dramatic. Also shown in Figure 1.7 is the transmission T, defined as the ratio of the line-integrated intensity of the MS, AAPR, and VCR cases to the line-integrated intensity for the optically thin case. The transmission is greater than 1 for impact of 1 kev electrons, since the source region of the photons is above a thick layer of conservatively scattering hydrogen, resulting in a kind of

Figure 1.7

Lyman-α intensity $I^{+}(\tau=0,\mu=0.5)$ in ph cm^{-2} sec^{-1} sr^{-1} $\Delta\nu_D^{-1}$ versus frequency (Doppler units at 150K). Solid line: optically thin approximation. Crosses: MS approximation (solid line is interpolated). Open circles: AAPR approximation (solid line is interpolated). Plus signs: VCR approximation (solid line is interpolated). Also shown are the values for the transmission T, defined here as the ratio of the line-integrated intensity of either the MS, AAPR, or VCR case to the line-integrated intensity of the optically thin approximation. Results for a 1 erg cm^{-2} sec^{-1} flux of (a) 1 keV electrons, (b) 10 keV electrons, and (c) 100 keV electrons.

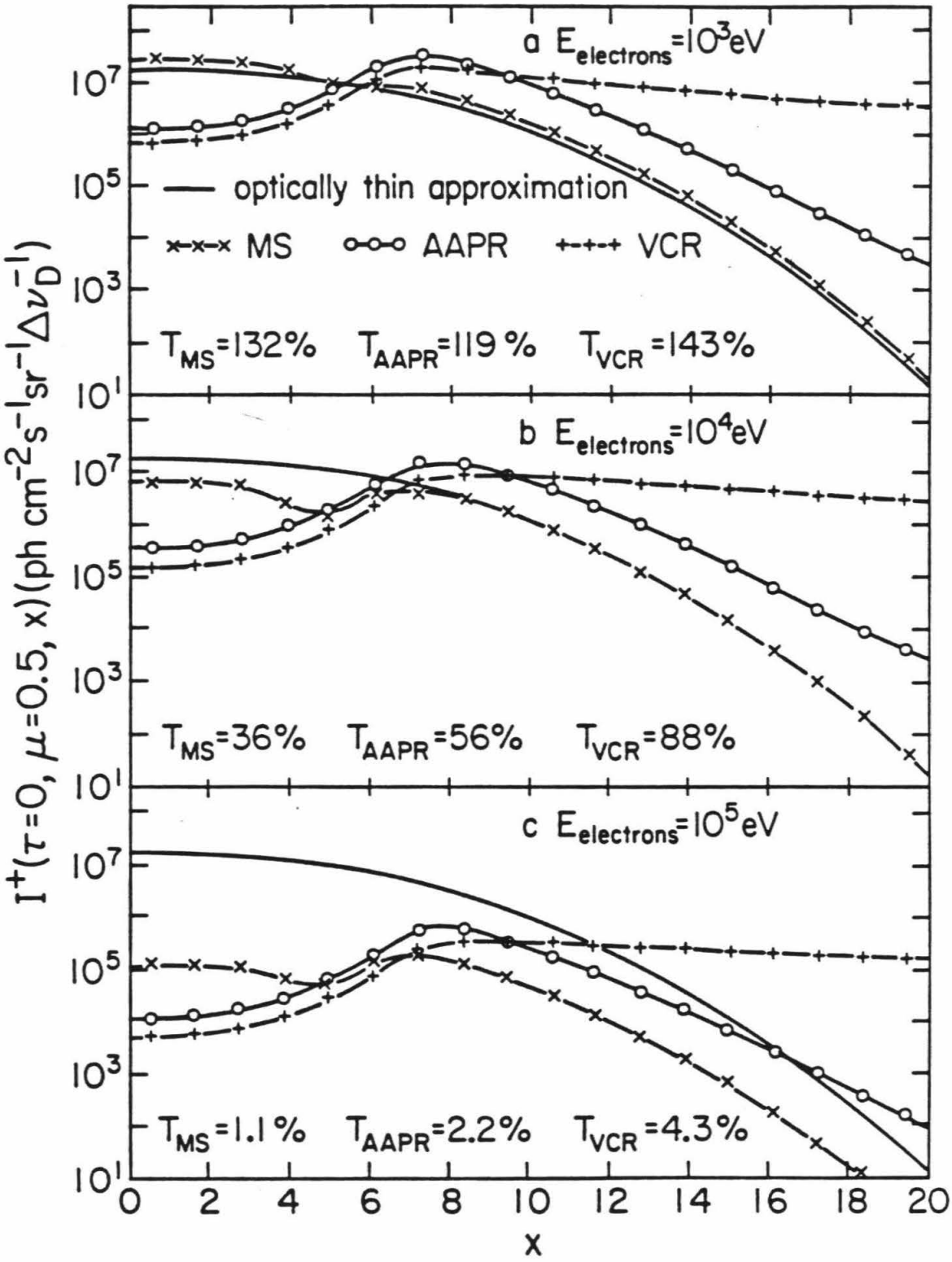
a $E_{electrons}=10^3$eV
b $E_{electrons}=10^4$eV
c $E_{electrons}=10^5$eV
optically thin approximation
MS
AAPR
VCR
T_{MS}=132% T_{AAPR}=119% T_{VCR}=143%
T_{MS}=36% T_{AAPR}=56% T_{VCR}=88%
T_{MS}=1.1% T_{AAPR}=2.2% T_{VCR}=4.3%
$I^+(\tau=0, \mu=0.5, x)$(ph cm^{-2}s^{-1}sr$^{-1}\Delta\nu_D^{-1}$)
x

reflection effect. Frequency redistribution can have important effects on the line profiles and the line-integrated intensities for a given source $V(z,x)$. It can be seen that VCR is very efficient at letting photons escape, but AAPR is not as efficient, the difference between them being anywhere from about 20% to about 100% depending on the energy of the precipitating particles. This shows that not only is frequency redistribution important, but the type of redistribution used is also crucial. The validity of these results could be tested by future observations of auroral Lyman-α emissions at high resolution. Auroral emissions of Lyman-β should also show the effects of frequency redistribution. However, since this is not a true resonance line most of the photons will be converted into Hα and Lyman-α photons after a large number of scatterings.

1.6 Conclusions

The purpose of this chapter was to introduce and demonstrate the usefulness of solving the equation of transfer directly by finite difference numerical methods. This allows for much more variety in forcing functions and boundary conditions and is generally more intuitive than either Monte Carlo or integral methods. The FMP method is easily generalized to give better angular resolution and better frequency resolution, being limited only by the available computer capacity. The largest case of 150 levels in z, 5 angles, and 10 frequencies required ~ 6800 K of region, but the program could undoubtedly be improved to be much more efficient. The agreement with standard cases is good in most cases, with only a few areas of moderate disagreement. It has been demonstrated that this method is versatile enough to be useful in moderately detailed investigations of the radiative transfer of a great variety of problems in planetary atmospheres. Further application of this program is made in Chapters 2 and 3.

Chapter 2

An Analysis of the Reflection Spectrum of Jupiter from 1500 Å to 1740 Å

2.1 Introduction

Solar ultraviolet light in the range from 1500 Å to 1740 Å penetrates the atmosphere of Jupiter to a pressure of ~ 10 to 30 mbar. This region is located between two and three scale heights above the tropopause (at ~ 150 mbar). The principal absorbing gases expected in this region are C_2H_2 and C_2H_6. Possible minor absorption may be present due to C_4H_2 and C_2H_4. Although these last two gases have not been detected spectroscopically, their presence is predicted by photochemical models of Jupiter and they have large absorption cross-sections in this spectral range. Methane is not an important absorber at wavelengths longer than 1500 Å. Although its mixing ratio falls rapidly with height above the tropopause due to photodissociation, NH_3 may also affect the spectrum, especially at the longer wavelengths. Other gases, such as CH_3C_2H,C_3H_8,PH_3 and H_2S may also have a marginal effect on the spectrum if they are present in the region, but they are not considered here. In most recent models of the reflection spectra of Jupiter at longer wavelengths (0.3 to 1 μm) it has been found necessary to include a haze layer above the cloud deck at ~ 500 mbar. This haze extends up to ~ 150 mbar or possibly higher (Sato and Hansen 1979; West 1981). Also complicating the spectrum is the presence of dayglow emission from the H_2 Lyman bands at a much higher altitude.

In this study, we have modeled the reflection spectrum in an attempt to determine the mixing ratios of the major gases C_2H_2 and C_2H_6, obtain upper limits to the mixing ratios of the minor gases C_2H_4, C_4H_2, and NH_3, determine the amount of dust (if any) in the stratosphere, and deduce the intensity of the H_2 Lyman band dayglow emission. The derived mixing ratios and upper limits are

useful in constraining photochemical models of the upper atmosphere of Jupiter. They may also be compared with mixing ratios determined from infrared spectra, such as the *IRIS* instruments on *Voyagers* 1 and 2. One advantage of analyzing UV absorption spectra to obtain mixing ratios is that the results are not sensitive to the temperature profile. We are also able to obtain some constraints on the scale heights of the major absorbers (C_2H_2 and C_2H_6) at ~ 10 mbar.

In section 2.2 we discuss the data and the model parameters associated with the *International Ultraviolet Explorer* (*IUE*). In section 2.3 the model parameters associated with the atmosphere of Jupiter are described, along with the homogeneous and inhomogeneous models that were used. In section 2.4 we present the results of the modeling calculations and compare these with the results of others. Our conclusions are presented in section 2.5.

2.2 Data and *IUE* Model Parameters

The spectrum we are modeling is a sum of eleven 15-minute spectra taken of Jupiter between December 1978 and June 1979 with the *IUE* (Clarke et al. 1982). The spectra were taken at low resolution with the large aperture of the short wavelength prime camera centered on Jupiter. The resulting spectral resolution was 10 Å full-width half-maximum (FWHM). This spectrum is shown in Figure 2.1a, along with a scaled solar spectrum (Mount et al. 1980) degraded to *IUE* resolution. Also shown in this figure above 1695 Å is a spectrum which is the sum of three 5-minute spectra. Below 1500 Å the signal is too small to be modeled, while above 1740 Å scattered light begins to be a problem in the *IUE* (Clarke et al. 1982). We thus restrict our modeling to within these limits.

As seen from the *IUE*, the phase angle of Jupiter is always less than 11°. In our models we consider the phase angle to be 0°. The error introduced by

Figure 2.1

(a) Lower line, 1500 Å to 1740 Å; sum of eleven 15-minute exposures of Jupiter taken with the *IUE* between December 1978 and June 1979 by Clarke et al. (1982). Lower line, 1700 Å to 1750 Å; sum of three 5-minute exposures taken between May and July 1980. Upper line; solar spectrum of Mount et al. (1980) degraded to *IUE* resolution. The upper line scale is shifted upward by 0.04 and is the flux that would be observed by the *IUE* if the backscattered reflectivity of Jupiter were 0.2.

(b) The observed UV reflectivity of Jupiter from 1500 Å to 1740 Å using the data in Figure 2.1a. The major absorption features of C_2H_2 longward of 1625 Å are indicated (see also Figure 2.7).

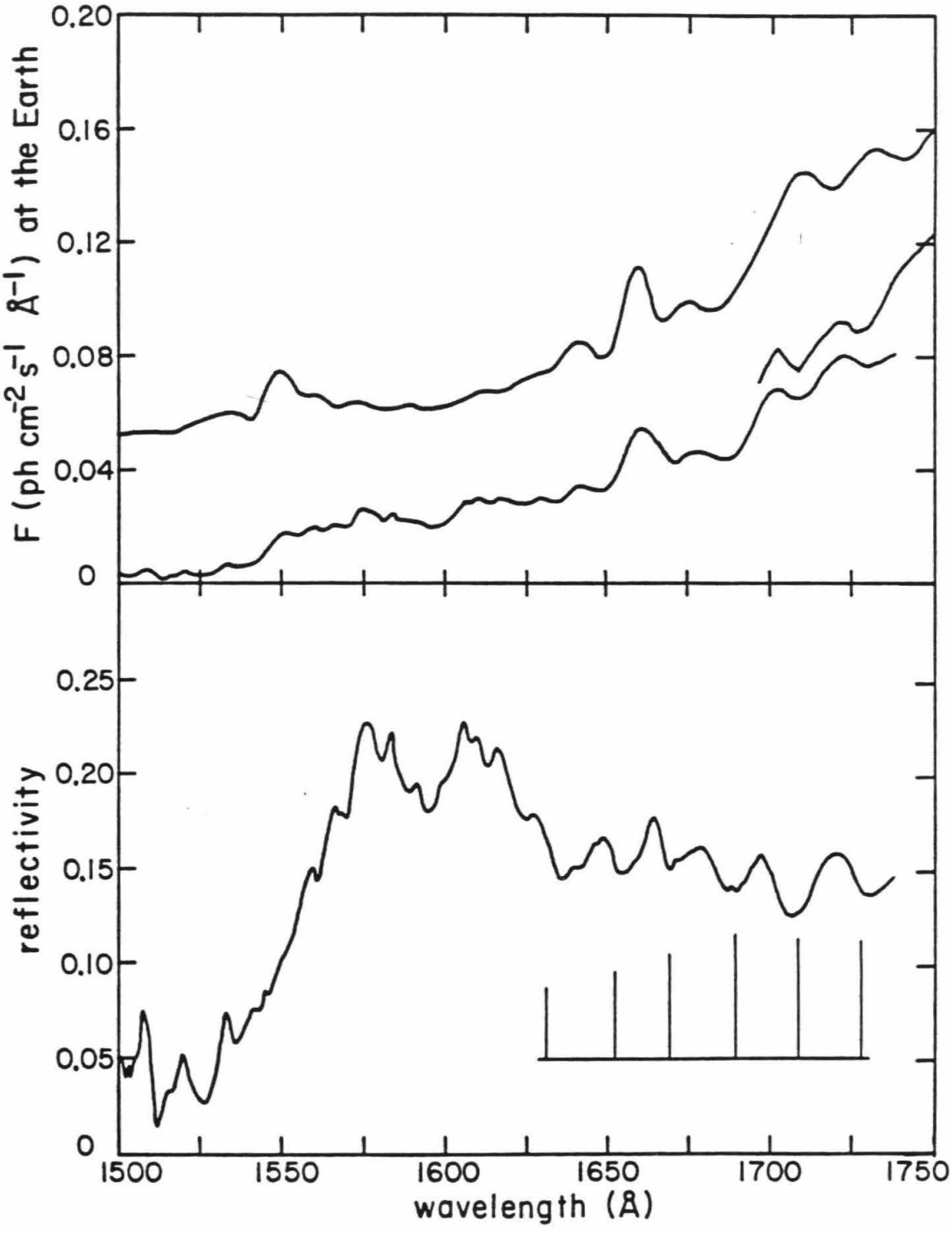
0.20
0.16
0.12
0.08
0.04
0
F (ph cm^{-2} s^{-1} Å^{-1}) at the Earth
0.25
0.20
0.15
0.10
0.05
0
reflectivity
1500
1550
1600
1650
1700
1750
wavelength (Å)

this approximation is less than 2% as long as the single-scattering albedo of the atmosphere is below 0.8. The footprint of the large aperture (subtending a solid angle of 175 sq arcsec or 4.11(-9) sr) on Jupiter was such that the average solar zenith angle within it was ~20°. The flux received by the *IUE* from Jupiter is given by

$$F_{\oplus} = \omega\left[\frac{pF_{\odot}}{\pi R^2} + \frac{10^9}{4\pi} I_{\text{dayglow}}\right] \tag{2.1}$$

where $\omega \equiv$ the solid angle subtended by the *IUE* aperture = 4.11(-9) sr, $p \equiv$ the backscattering reflectivity of Jupiter averaged over the footprint of the *IUE* aperture on the planet, $F_{\odot} \equiv$ the solar flux at 1 a.u. (taken from Mount et al. 1980), $R \equiv$ the sun-Jupiter distance in a.u. = 5.203, and $I_{\text{dayglow}} \equiv$ the H_2 Lyman band emission in kiloRayleighs (1 kR = 10^9 photons cm $^{-2}$ sec $^{-1}$). We approximate p with I/F at $\mu = \mu_0 = \cos 20°$, $\varphi - \varphi_0 = 180°$ (where μ is the cosine of the local zenith angle and φ is the azimuth angle). The variation of the observed p with wavelength is shown in Figure 2.1b, along with identification of some of the major absorption bands of C_2H_2.

$F_{\oplus}$ is calculated at 1 Å intervals (both the solar fluxes and the H_2 band intensities used are at 1 Å resolution) and is then degraded to *IUE* resolution for comparison with the observed spectrum. We model $F_{\oplus}$ rather than the observed p reflectivity for the following reason. Modeling of $F_{\oplus}$ requires only one smoothing of the model calculations to simulate the data. To model the observed p we would need to smooth the calculations a second time, either before or after division by the scaled solar fluxes. This would degrade the spectrum unnecessarily, reducing the amount of information contained in it and adding artifacts from the solar spectrum.

Degrading the calculated model spectrum to *IUE* resolution requires knowledge of the *IUE* instrument function. Since Jupiter is a diffuse source, the

instrument function is a convolution of the large aperture with the grating function and then with the analyzing aperture. The dimensions of the large aperture have recently been redetermined by Panek (1981). This aperture is the major source of dispersion, having a FWHM of 9.6± 0.3 Å. The grating function is assumed to be a Gaussian with a FWHM of 4.2 Å. The analyzing aperture we consider to be a delta-function, since exposures are read out pixel by pixel, which introduces no additional dispersion. The resulting instrument function we calculate has a FWHM of 9.6 Å and is shown in Figure 2.2. By applying this smoothing function to our calculated spectra we obtain a reasonably good fit to the *IUE* spectrum. There remains a slight difference in resolution which may be a result of the error in the aperture dimensions, the stacking of the *IUE* spectra, or possibly the inhomogeneity of the atmosphere, as we will show in sections 2.3 and 2.4.

2.3 Jupiter Model Parameters

From the previous section it is clear that the only Jupiter-related parameters necessary for the modeling of the *IUE* spectrum are the backscattering reflectivity averaged over the footprint of the *IUE* aperture on Jupiter, which we approximate by I/F ($\mu = \mu_0 = \cos 20°$, $\varphi - \varphi_0 = 180°$), and the amount of emission in the H_2 Lyman bands. We use the results of Yung et al. (1982a) for the spectral shape of the H_2 Lyman bands and assume that the emission is excited by 100 eV electrons.

As a first approximation, we consider the atmosphere of Jupiter to be homogeneous, i.e. the mixing ratios of all the scatterers and absorbers are assumed to be constant throughout the atmosphere. The only scatterers in our model are H_2, He, and "dust." For simplicity, we assume that the dust has a Rayleigh phase function, as do the gases. This is, of course, not a very realistic

Figure 2.2

The instrument function for the SWP camera of the *IUE* for an extended source observed under low dispersion with the large aperture.

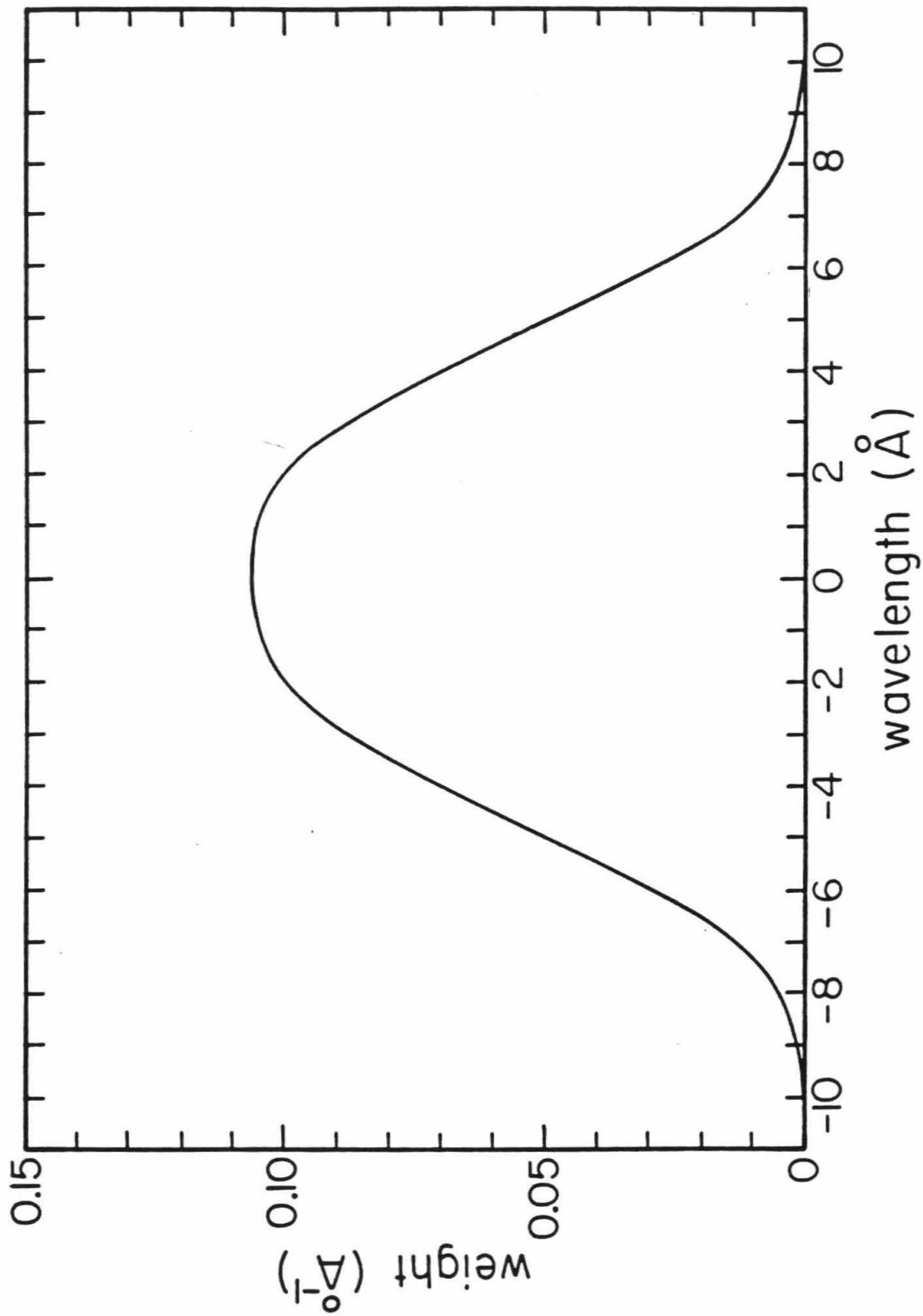
0.15
0.10
0.05
0
weight (Å⁻¹)
-10
-8
-6
-4
-2
0
2
4
6
8
10
wavelength (Å)

assumption, but it allows the dust to make a small contribution to the scattering. The main purpose of including dust is to test the need for a continuum absorber. The H_2 volume mixing ratio is held constant at 89% ($f_{H_2} = 0.89$), so that H_2 does most of the scattering. The cross-sections for Rayleigh scattering by H_2 were taken from Ford and Browne (1973). We hold f_{He} constant at 0.11 and take the scattering cross-sections to be 0.1 times those of the H_2, based on relative polarizabilities. Since He accounts for at most ~ 1% of the scattering, this assumption will not greatly affect the model results. The value of f_{dust} is allowed to vary, and the total cross-section is assumed to be constant at 1×10^{-16} cm^2. For the dust single-scattering albedo we use a formula given by Sato and Hansen (1979) which yields $\tilde{\omega}_{dust} = 0.18$ at 1650 Å. This formula was derived for wavelengths longer than 3000 Å and it is probable that it does not hold too well at the wavelengths we are considering. The optical depth of dust above the tropopause may be estimated by

$$\tau_{dust} \approx 1.1 \times 10^8 (15)^{H_s/H_a} f_{dust} H_a / H_s \quad . \tag{2.2}$$

For all the models we calculated, $\tau_{dust} < 1$.

The absorbers considered in the model (besides the dust) are C_2H_2, C_2H_6, C_4H_2, C_2H_4, and NH_3, in roughly the order of their importance. The cross-sections for these absorbers are taken from Nakayama and Watanabe (1964), Mount and Moos (1978), Okabe (1981), Zelikoff and Watanabe (1953), and Watanabe (1954), respectively.

We also assume that the atmosphere is infinite. This is clearly not true for the real atmosphere, since below the tropopause the mixing ratios of all of the hydrocarbons (except CH_4) will decrease rapidly. The reason for this is that these gases are created photochemically in the stratosphere and are not in

thermodynamic equilibrium. Once they pass below the tropopause they will be mixed rapidly down to levels where they can be destroyed by pyrolysis. However, if the total optical depth at the tropopause is $\gtrsim 3$, and the single-scattering albedo is less than ~ 0.8, then any structure below the tropopause will have less than a 10% effect on the backscattered reflectivity. As we will see, this conditions are indeed met by the actual atmosphere.

For an infinite, homogeneous atmosphere, the only remaining parameter that can modify I/F is the single-scattering albedo, $\tilde{\omega}_0$. For a mixture of scattering and absorbing gases, we define $\tilde{\omega}_0$ as

$$\tilde{\omega}_0 = \left[1 + \frac{\sum f_a \sigma_a}{\sum f_s \sigma_s}\right]^{-1} , \tag{2.3}$$

where $f_a \equiv$ absorber mixing ratio at 10 mbar, $f_s \equiv$ scatterer mixing ratio at 10 mbar, $\sigma_a \equiv$ absorber cross-section, and $\sigma_s \equiv$ scatterer cross-section. The choice of reference level is arbitrary and $p = 10$ mbar is used because for most of the spectral range considered it is approximately the level at which the total optical depth is 0.5.

A plot of I/F versus $\tilde{\omega}_0$ for a homogeneous, infinite atmosphere is shown in Figure 2.3. The curves in this figure were calculated using a ten-stream Feautrier radiative transfer program (see Chapter 1). We find that the empirical function

$$I/F = -0.1854 \ln(1 - \tilde{\omega}_0) \tag{2.4}$$

represents the true I/F to within 1% for $\tilde{\omega}_0 < 0.95$.

To produce a model fit to the observed spectrum we proceed as follows. First, a guess is made for the volume mixing ratios of the absorbing gases and dust, and for the intensity of the Lyman band emission. Next, we calculate $F_\oplus$ at 1 Å intervals via Equations (2.3), (2.4), and (2.1). This model spectrum is then

Figure 2.3

Backscattered reflectivity versus the single-scattering albedo at the level where $\tau_s = 1$, for the cases in which the ratio of scatterer to absorber scale heights, H_s/H_a, is 2.0, 1.0 (homogeneous), and 0.5.

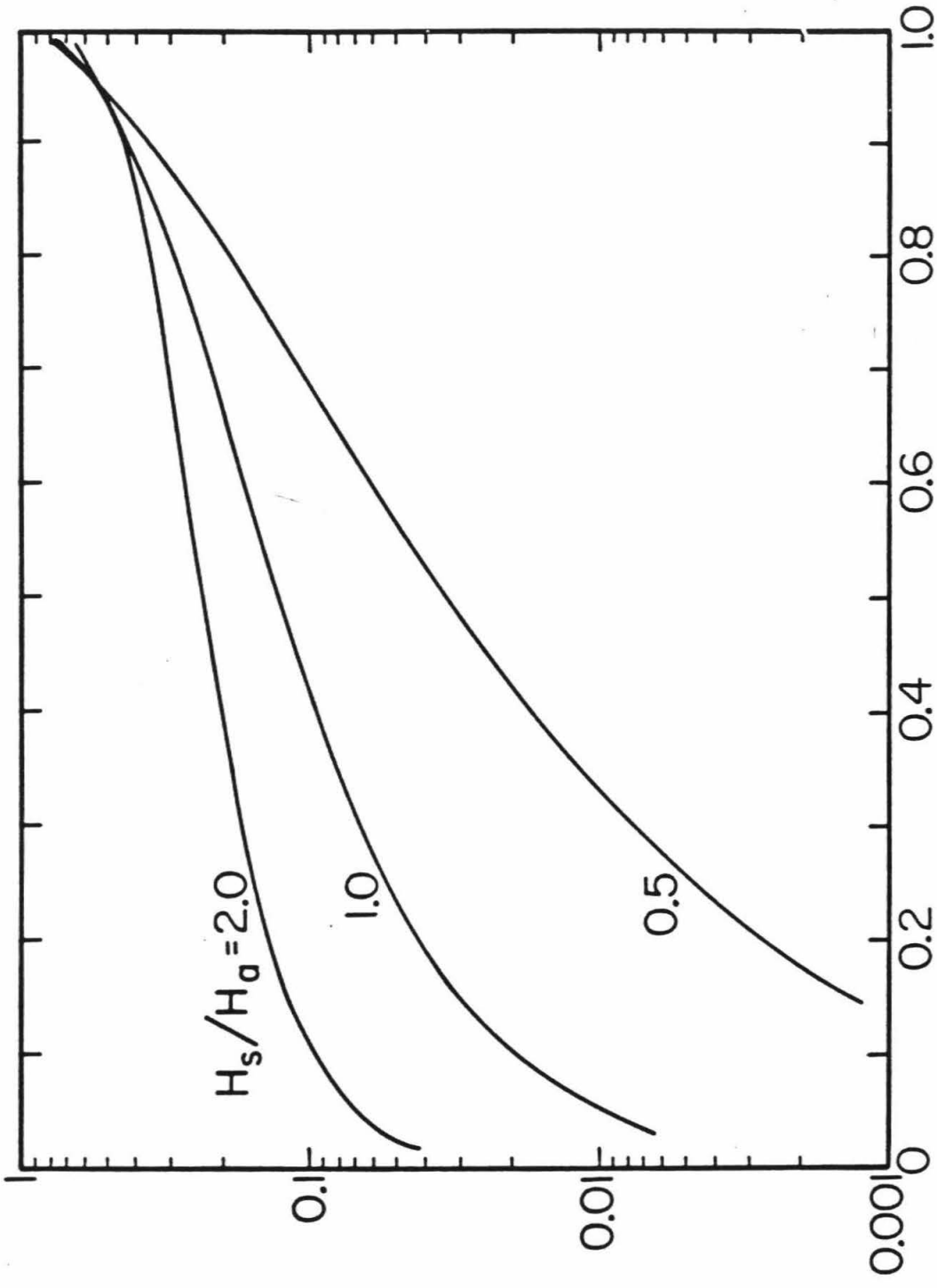
1/F (μ = μ0 = cos (20°), φ - φ0 = 180°)
1.0
0.1
0.01
0.001
0
0.2
0.4
0.6
0.8
1.0
ϖ0 (at τs=1)
Hs/Ha=2.0
1.0
0.5

smoothed using the *IUE* aperture function obtained in section 2.2 (see Figure 2.2) and compared to the observed spectrum between 1500 Å and 1740 Å. The model parameters are then updated and the cycle is repeated until the model spectrum is a least squares approximation of the observed spectrum.

Although the homogeneous models provide a fairly good fit to the observed spectrum, we also wanted to explore cases that were more like the real Jupiter, that is to say, inhomogeneous. To accomplish this we add an extra parameter, the ratio of scatterer to absorber scale heights. The reason for the difference between the two scale heights is that the main absorbers C_2H_2 and C_2H_6 are produced in the stratosphere and are being mixed down until they pass through the tropopause. Their scale heights are determined by the atmospheric eddy diffusion profile and their chemical lifetimes, and are likely to be different from the scale height of the bulk (H_2) atmosphere. For a range of eddy diffusion coefficients at the tropopause between 1×10^3 and 1×10^4 $cm^2\ sec^{-1}$, we expect that the mixing ratios of both C_2H_2 and C_2H_6 will increase with height, i.e. the ratio of scatterer to absorber scale heights, $H_s/H_a < 1$. On the other hand, absorbers such as NH_3 and dust are expected to have mixing ratios that decrease with height, so that $H_s/H_a > 1$. Of course, each absorber probably has a different scale height in the real atmosphere, but we assume here that they are all identical. With this approximation, we can now write the total optical depth and the single-scattering albedo as a function of the scatterer optical depth, i.e.

$$\tau_t = \tau_s + \frac{H_a}{H_s}\left(\frac{1}{\tilde{\omega}_1} - 1\right)\tau_s^{H_s/H_a} \qquad (2.5)$$

and

$$\tilde{\omega}_0 = \left[1 + \left(\frac{1}{\tilde{\omega}_1} - 1\right)\tau_s^{H_s/H_a - 1}\right]^{-1} , \qquad (2.6)$$

where $\tilde{\omega}_1$ is the single-scattering albedo at the level where the scatterer optical depth is equal to one.

In Figure 2.3 we plot I/F ($\mu = \mu_0 = \cos 20°$, $\varphi - \varphi_0 = 180°$) for the cases $H_s/H_a = 0.5$, and 2.0, along with the homogeneous case, $H_s/H_a = 1.0$. Generalizing from the homogeneous case, we find that the function

$$I/F = \left[A \ln(1 - \tilde{\omega}_1)\right]^{H_a/H_s} \qquad (2.7)$$

gives a reasonable fit to the actual I/F if we have $A = -0.273$ for $H_s/H_a = 0.5$ and $A = -0.081$ for $H_s/H_a = 2.0$. These expressions are accurate to 10% in I/F for $0.05 < \tilde{\omega}_1 < 0.9$ with $H_s/H_a = 2.0$, and for $0.45 < \tilde{\omega}_1 < 0.9$ with $H_s/H_a = 0.5$, as determined using the same program that was used in testing the function in the homogeneous case. Using Equation (2.7) in place of Equation (2.4), we follow the same fitting procedure that was used in the homogeneous case.

The results of both the homogeneous and inhomogeneous models are presented and compared with previous measurements in the next section.

2.4 Model Results and Comparisons

In this section we show the model spectra that result when the mixing ratios of C_2H_2, C_2H_6, C_4H_2, C_2H_4, and the amount of Lyman band emission are " floated " i.e. they are left as free parameters in the least squares fit of the data and are solved for by iteration, with $f_{NH_3} = f_{dust} = 0$. We consider the cases $H_s/H_a = 0.5$, 1.0, and 2.0. Later we will consider cases in which only $f_{NH_3} = 0$, and cases in which all the mixing ratios (including f_{NH_3} and f_{dust}) are floated.

Figure 2.4a presents the model spectra associated with the first situation, for the three cases $H_s/H_a = 0.5$, 1.0, and 2.0, along with the observed

Figure 2.4a

Solid line; observed *IUE* spectra, as shown in Figure 2.1a. Dotted line; model spectrum #1 ($H_e/H_\alpha = 0.5$). Short dashed line; model spectrum #2 ($H_e/H_\alpha = 1.0$). Long dashed line; model spectrum #3 ($H_e/H_\alpha = 2.0$).

Figure 2.4b

Solid line; observed *IUE* reflectivity, as shown in Figure 2.1b. Dotted line; model #1 reflectivity ($H_e/H_\alpha = 0.5$). Short dashed line; model #2 reflectivity ($H_e/H_\alpha = 1.0$). Long dashed line; model #3 reflectivity ($H_e/H_\alpha = 2.0$).

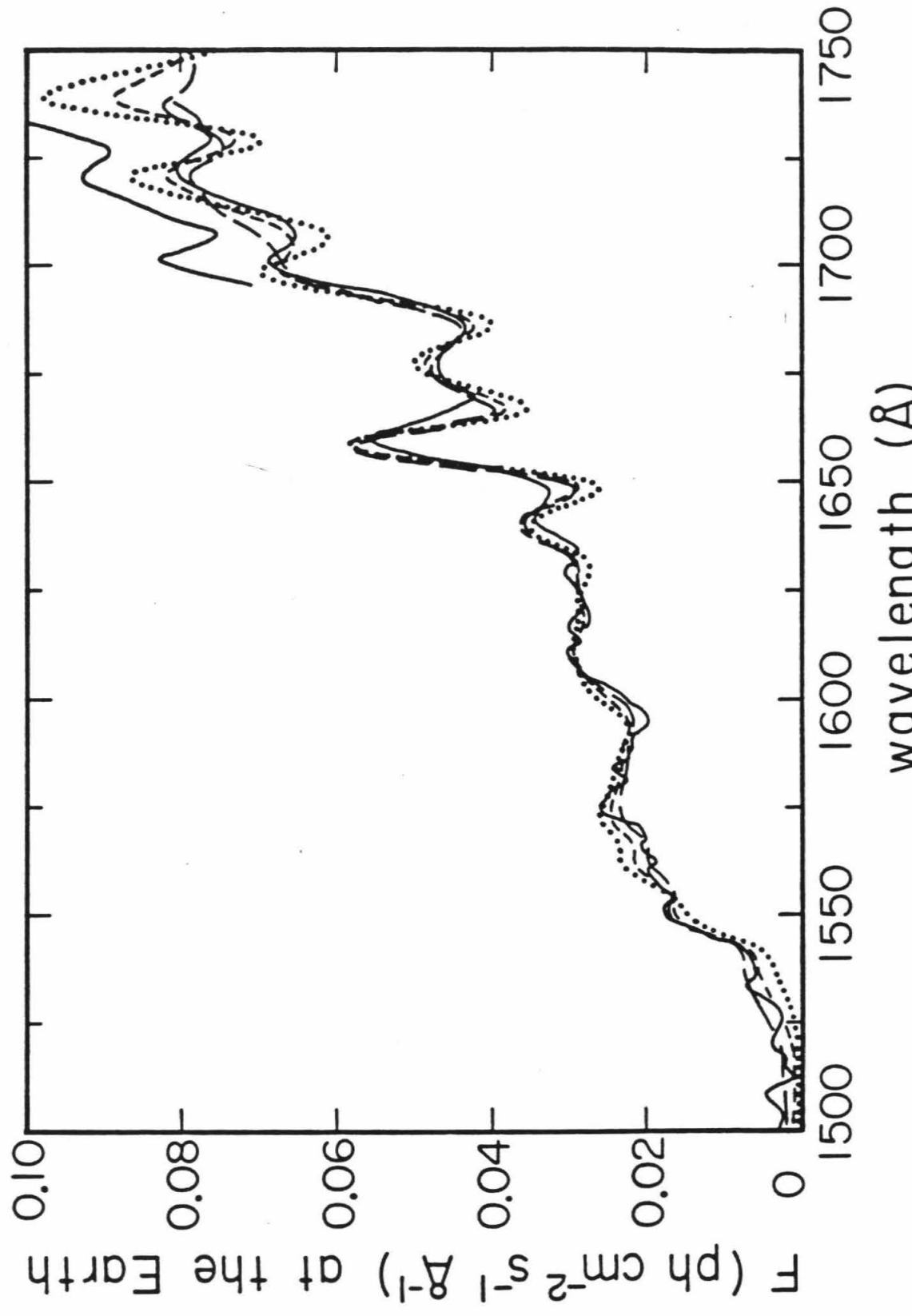
0.10
0.08
0.06
0.04
0.02
0
1500
1550
1600
1650
1700
1750
wavelength (Å)
T (ph cm⁻² s⁻¹ Å⁻¹) at the Earth

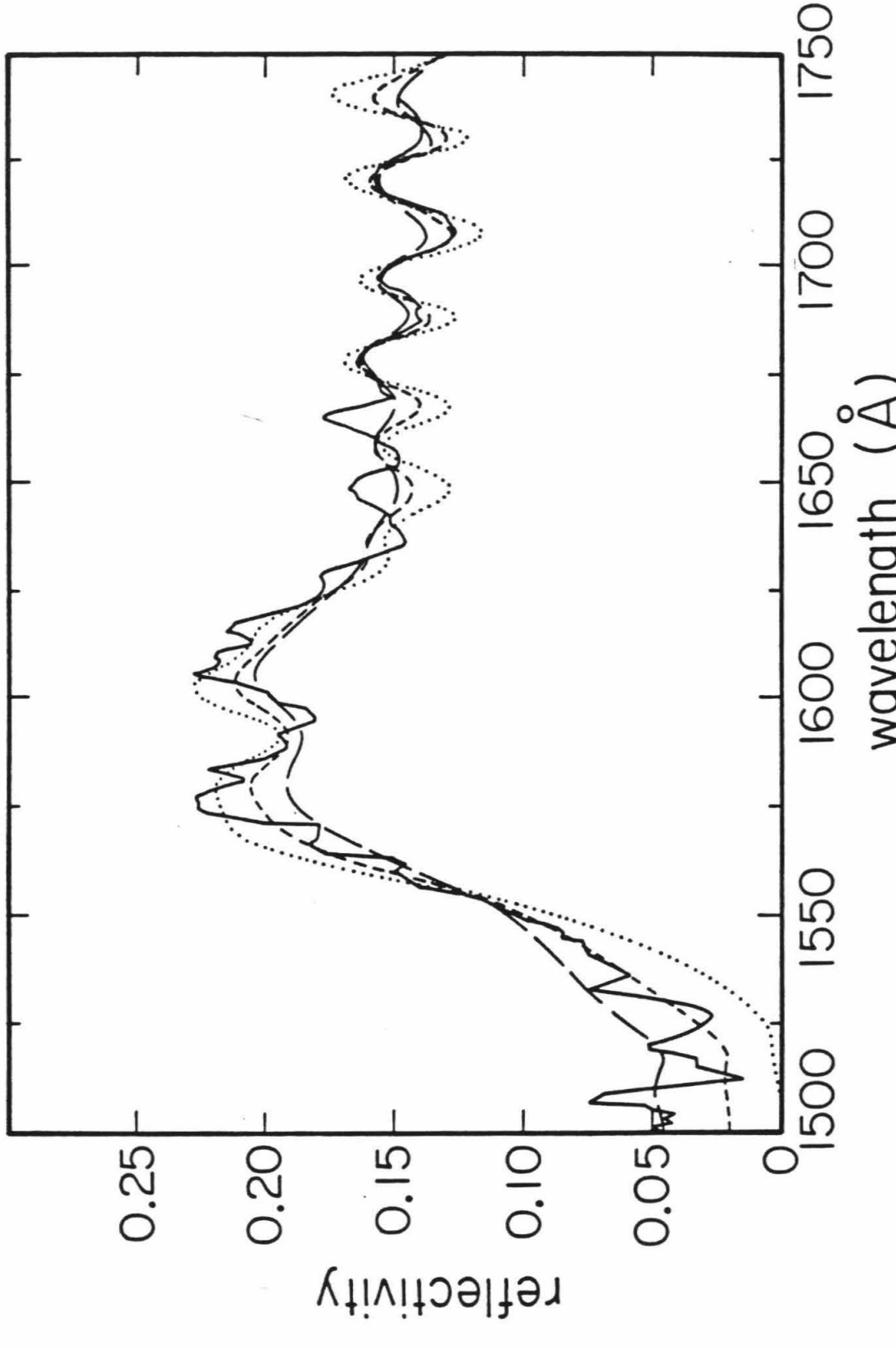
reflectivity
0.25
0.20
0.15
0.10
0.05
0
1500
1550
1600
1650
1700
1750
wavelength (Å)

spectrum for comparison. It is apparent that the "continuum level" (i.e. variations on a scale of $\gtrsim$ 50 Å) are extremely well accounted for by the least squares fitting process. Variations on a scale of $\lesssim$ 20 Å are much harder to fit. This is due to uncertainties in the fine structure of both the solar spectrum and the cross-sections used, as well as the noise in the data. Although all the models give similar results, we distinguish the best from the worst by their ability to fit these small scale variations. For instance, it may be seen that the fit for the H_s/H_a = 2.0 case is poor above 1700 Å, and the fit for the H_s/H_a = 0.5 case deteriorates below 1600 Å and has too much contrast, i.e. peak to valley amplitude. On a "quality of fit" scale from 1 (poor) to 5 (good), we would assign a 4 to the H_s/H_a = 1.0 case, a 3 to the H_s/H_a = 2.0 case, and a 2 to the H_s/H_a = 0.5 case.

Figure 2.4b shows how the comparison for the three cases of Figure 2.4a look in terms of the reflectivities p. The observed p is that of Figure 2.1b, and is obtained by dividing the observed $F_\oplus$ by the properly scaled solar flux, then smoothing this by the instrument function. The models are just the calculated values of p smoothed by the instrument function. There is a strong anticorrelation between the models and the data from 1640 to 1670 Å. This is caused by artifacts of the solar CI emission feature at 1657 Å. These artifacts could be the source of the claim by Clarke et al. (1982) of a CI emission feature on Jupiter. Another reason we choose to model $F_\oplus$ instead of p is that the curves in Figure 2.4b give a misleading impression of the signal-to-noise of the data, which of course actually increases strongly towards the long wavelength end of the spectrum.

In Figure 2.5 we show the mixing ratio profiles derived for the three cases of Figures 2.4a and 2.4b. Profiles with negative slopes, vertical lines, and positive slopes correspond to the cases H_s/H_a = 2.0, H_s/H_a = 1.0, and

Figure 2.5

Mixing ratios of the absorbing gases for the three cases of Figure 2.4 plotted against pressure and altitude (as measured in atmospheric scale heights above the tropopause). Negative slopes correspond to $H_s/H_a = 2.0$, vertical lines to $H_s/H_a = 1.0$, and positive slopes to $H_s/H_a = 0.5$. The lines for C_2H_4 are dashed to distinguish them from those for C_4H_2. The error bars plotted at the intersection regions are taken from Table 2.1.

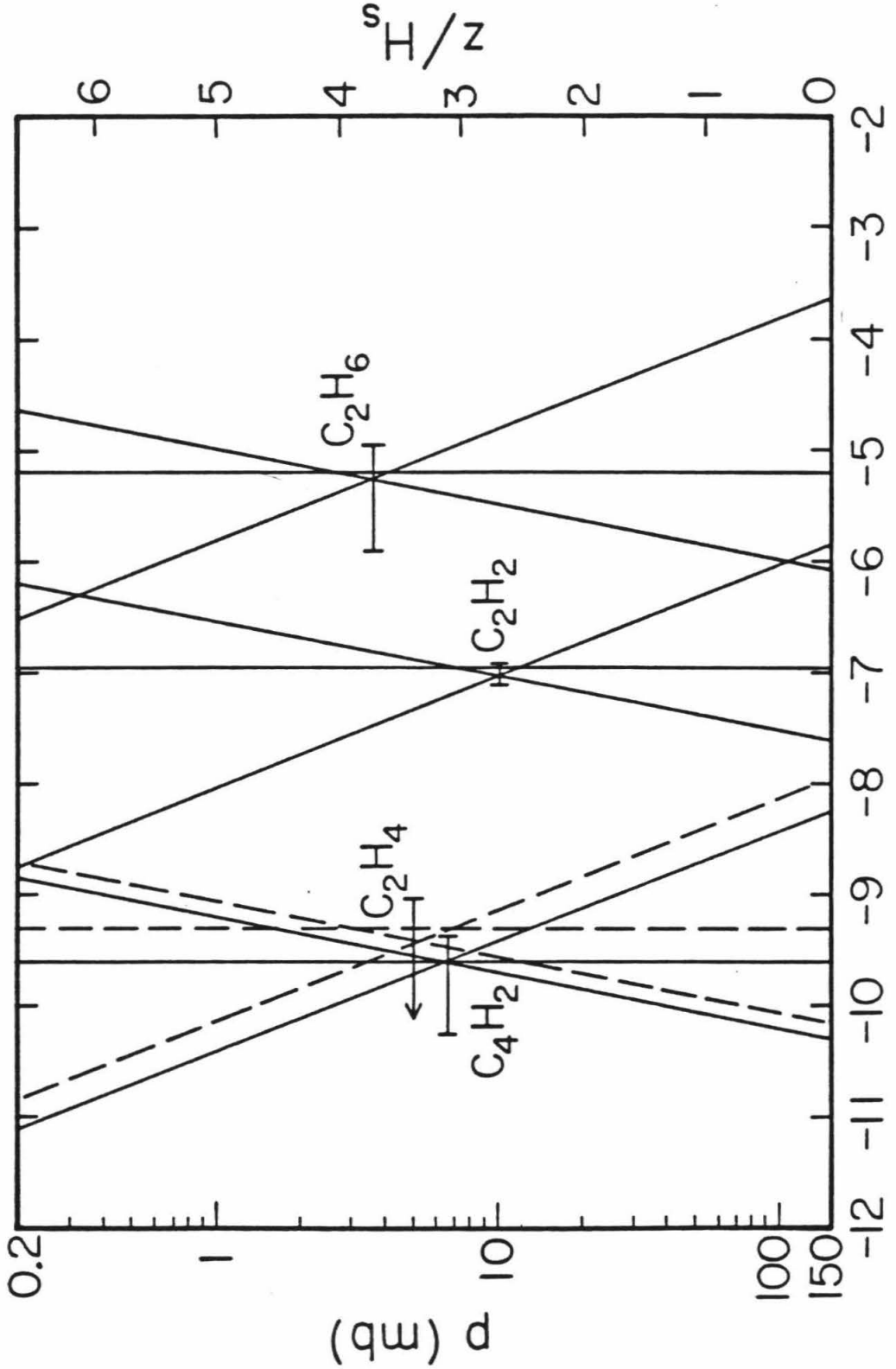
H_s/z
6
5
4
3
2
1
0
p (mb)
0.2
1
10
100
150
C_2H_6
C_2H_2
C_2H_4
C_4H_2
-2
-3
-4
-5
-6
-7
-8
-9
-10
-11
-12
log f_i

H_s/H_a = 0.5, respectively. Dashed lines are used for $f_{C_2H_4}$ profiles to distinguish them from $f_{C_4H_2}$ profiles. The significance of the error bars that are plotted at the intersection regions of the profiles is discussed below. For the absorbing gases, all three profiles intersect at a pressure of ~ 3 to 10 mbar, so this appears to be the least model-dependent region to assign the calculated homogeneous mixing ratio. The physical reason for this is illustrated in Figure 2.6. This figure shows the contribution to the reflectivity as a function of τ_t, i.e. it is the source function weighted by $e^{-\tau/\mu}$. The source function is composed of a term due to the scattering of diffuse flux and a term due to the first scattering of attenuated solar UV. The cases H_s/H_a = 0.5, 1.0 and 2.0 are presented, and it is seen that in each case a large contribution to the intensity comes from above τ_t = 0.5. The short dashes on each curve represent the level at which one-half the total reflectivity (~ 0.15) is attained. The pressures that correspond to the optical depths at a wavelength of 1650 Å are also shown in the figure.

To see the effect due to dust and NH_3, we calculate spectra for the three H_s/H_a ratios in which 1) all the mixing ratios are floated and in which 2) only f_{NH_3} is set equal to zero. These modifications do not affect the derived hydrocarbon mixing ratios by much, although both NH_3 and dust help improve the fits for the case H_s/H_a = 0.5 by lowering the contrast in the region above 1700 Å. The NH_3 accomplishes this by virtue of having its absorption bands ~ 180° out of phase with those of C_2H_2 in this spectral region, while the dust manages the same effect by adding continuum absorption and additional scattering.

The results for all nine models are presented in Table 2.1. We also list an index representing the quality of fit to small scale variations. It is seen that all the models give fairly similar results. The error bars represent 99% non-linear

Table 2.1. Absorber mixing ratios at P = 10 mbar and dayglow intensities derived from least squares fit

Model	H_s/H_a	Quality	$f_{C_2H_2}$ $\times 10^8$	$f_{C_2H_6}$ $\times 10^6$	$f_{C_4H_2}$ $\times 10^{10}$	$f_{C_2H_4}$ $\times 10^{10}$	f_{dust} $\times 10^{10}$	f_{NH_3} $\times 10^9$	$I_{dayglow}(kR)$
1	0.5	2	9.4 ± 0.9	3.2 ± 2.4	2.0 ± 1.4	$2.8 \pm {}^{3.3}_{2.8}$	—	—	$0.7 \pm {}^{3.3}_{0.7}$
2	1.0	4	11 ± 1	6.5 ± 5.1	2.6 ± 1.8	4.9 ± 4.0	—	—	$1.0 \pm {}^{2.6}_{1.0}$
3	2.0	3	9.1 ± 1.5	15 ± 12	3.7 ± 2.9	7.0 ± 5.4	—	—	$16 \pm {}^{2.4}_{1.6}$
4	0.5	2	8.7 ± 0.9	3.0 ± 2.4	1.8 ± 1.1	$1.6 \pm {}^{2.0}_{1.6}$	2.3 ± 1.4	—	$0.4 \pm {}^{3.5}_{0.4}$
5	1.0	4	10 ± 1	6.6 ± 4.7	2.9 ± 2.1	$3.3 \pm {}^{4.2}_{3.3}$	1.2 ± 1.2	—	$1.5 \pm {}^{3.0}_{1.5}$
6	2.0	3	8.1 ± 1.5	14 ± 12	3.3 ± 3.0	6.6 ± 5.7	0.24 ± 0.17	—	$1.7 \pm {}^{2.7}_{1.7}$
7	0.5	4	5.9 ± 0.8	2.7 ± 2.0	1.3 ± 1.0	$2.3 \pm {}^{3.3}_{2.3}$	4.8 ± 1.0	$2.0 \pm {}^{5.0}_{2.0}$	$1.7 \pm {}^{2.8}_{1.7}$
8	1.0	4	10 ± 1	6.6 ± 5.3	2.9 ± 2.0	$3.9 \pm {}^{4.9}_{3.9}$	$1.0 \pm {}^{1.4}_{1.0}$	$4.2 \pm {}^{6.7}_{4.2}$	$1.4 \pm {}^{2.4}_{1.4}$
9	2.0	3	7.9 ± 1.6	14 ± 14	3.1 ± 2.4	$7.2 \pm {}^{8.0}_{7.2}$	0.63 ± 0.24	$9 \pm {}^{20}_{9}$	$1.7 \pm {}^{2.6}_{1.7}$

Figure 2.6

The attenuated source function (with $\mu = \cos 20°$) plotted against for the cases H_s / H_a = 2.0, 1.0, and 0.5. The backscattered intensity (~ 0.15) is given by the area under each curve. The horizontal dashes on each curve mark the optical depth at which one-half the backscattered reflectivity is reached.

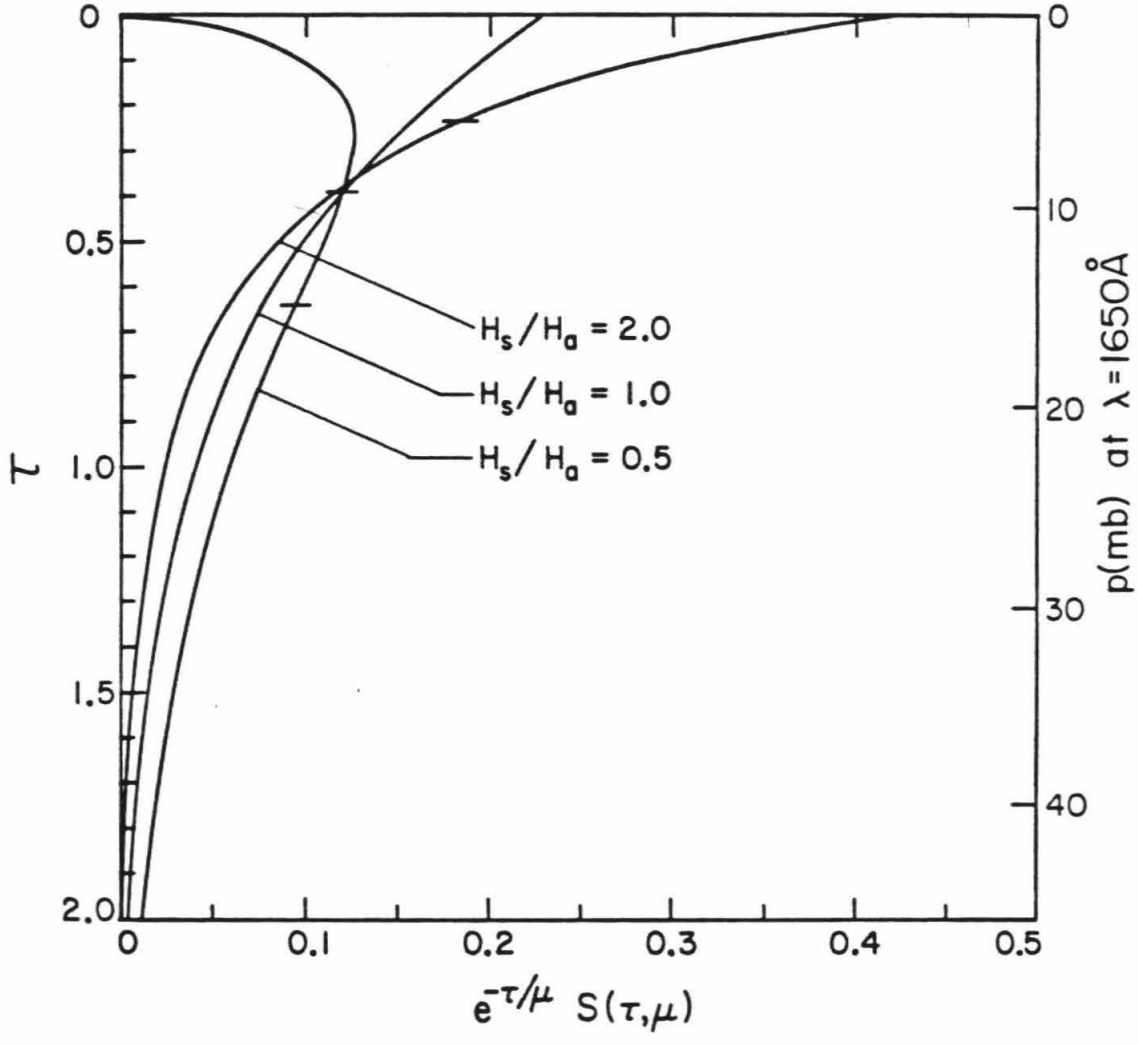
0
0.5
1.0
1.5
2.0
τ
0
0.1
0.2
0.3
0.4
0.5
$e^{-\tau/\mu}$ S(τ,μ)
H_s/H_a = 2.0
H_s/H_a = 1.0
H_s/H_a = 0.5
0
10
20
30
40
p(mb) at λ=1650Å

confidence level bounds and take into account that we really only have 240/9.6 ≈ 25 independent data points. On this basis, we can only give upper limits to the mixing ratios of C_2H_4, dust, NH_3, and the dayglow intensity. Surprisingly, it seems that some C_4H_2 is neccessary to obtain a good fit. We hold back from claiming a detection since there could be other absorbers not considered here that produce a similar effect. For that matter, the absorption spectra of the dust could possibly have a similar structure to that of C_4H_2 at these short wavelengths. Confirmation of C_4H_2 on Jupiter would require a less ambiguous detection, perhaps of the narrow infrared emission bands at 220 or 628 cm^{-1}.

To show the relative contributions of the absorbers at different wavelengths, we show in Figure 2.7 the optical depth of each absorber as a function of wavelength at a pressure of 10 mbar. Here we have used the mixing ratios derived for model #8, the homogeneous case ($H_s/H_a = 1.0$) with all mixing ratios floated (including f_{NH_3} and f_{dust}). This model was chosen because it gives upper limits to f_{dust} and f_{NH_3}. As can be seen from Table 2.1, choosing model #2 or model #5 would not significantly change the results. It is apparent from this figure that C_2H_6 is most important for the spectral shape below 1560 Å and C_2H_2 is most important above ~ 1640 Å. The minor absorber C_4H_2 plays a relatively important role between 1580 Å and 1650 Å. The minor absorber C_2H_4, however, has bands that overlap those of C_2H_2 in this spectral region, making it clear why only an upper limit for $f_{C_2H_4}$ was obtained. NH_3 plays almost no role in this spectra, and the effect of dust is minor. The total absorption optical depth at 10 mbar is seen to be mostly ~ 0.5, consistent with the results of Figures 2.5 and 2.6.

The ratio $f_{C_2H_6}/f_{C_2H_2}$ we get is 66± 53. This ratio is important for photochemical models of the upper atmosphere of Jupiter. The *IRIS* instrument

Figure 2.7

The wavelength dependence of the total optical depth and the individual absorber optical depths for C_2H_2, C_2H_6, C_4H_2, C_2H_4, and NH_3, at the level p = 10 mbar. The mixing ratios used are taken from Table 2.1, model #8.

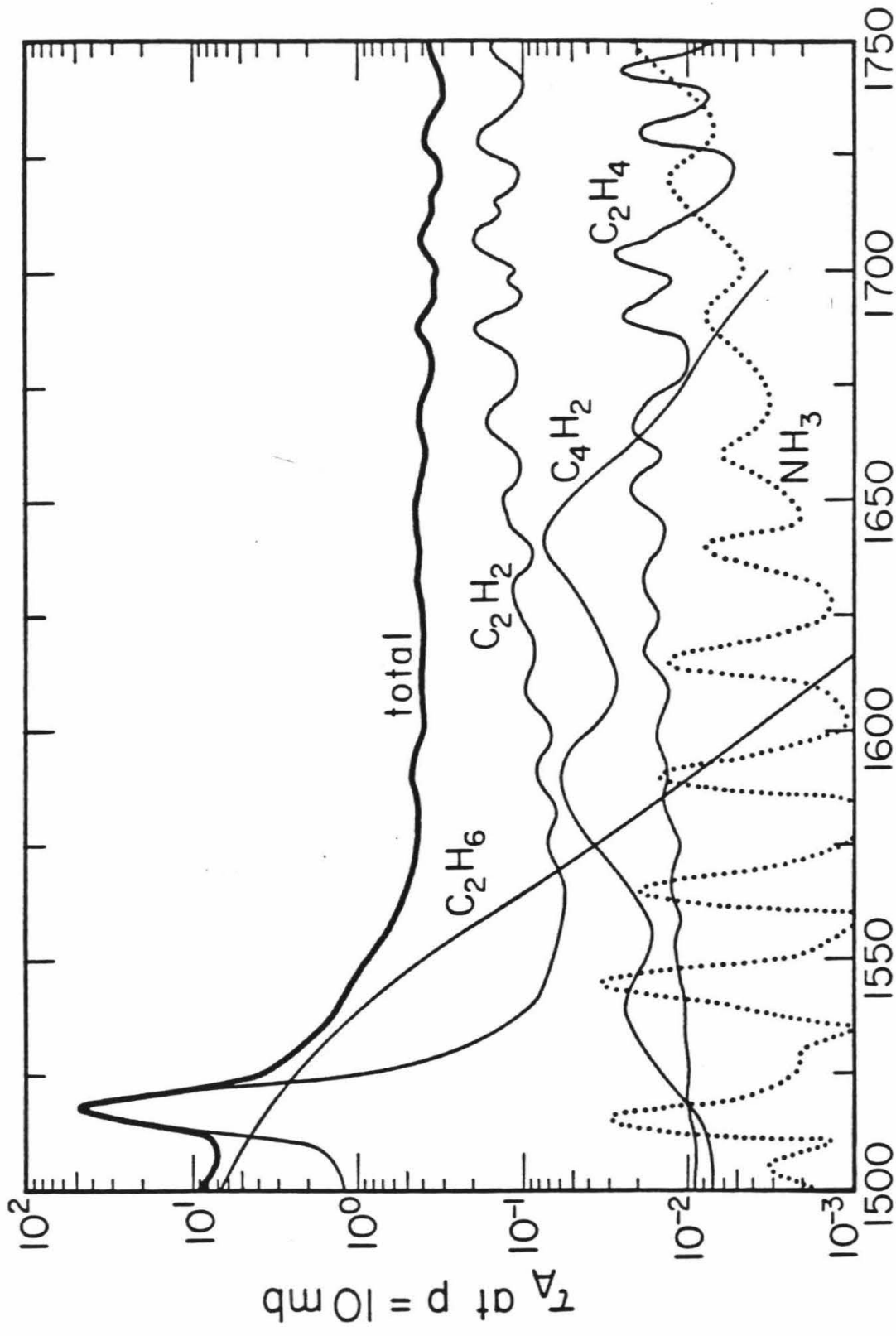
10^2
10^1
10^0
10^{-1}
10^{-2}
10^{-3}
τ_A at p = 10 mb
1500
1550
1600
1650
1700
1750
wavelength (Å)
total
C_2H_6
C_2H_2
C_4H_2
C_2H_4
NH_3

on *Voyagers* 1 and 2 observed C_2H_2 and C_2H_6 on Jupiter, and for the North Equatorial Belt found $f_{C_2H_2} = 3(-8)$ and $f_{C_2H_6} = 5(-6)$ at pressure level of ~ 15 to 90 mbar (Maguire 1981). In Figure 2.8 we plot our estimated mixing ratios and their errors, both in mixing ratio and in pressure, along with the *IRIS* values for C_2H_2 and C_2H_6. To the best we can determine, it appears that C_2H_6 is well-mixed. However, $f_{C_2H_2}$ appears to increase with decreasing pressure, consistent with a C_2H_2 scale height equal to twice the atmospheric scale height. From Figure 2.8 we also conclude that while the mixing ratio obtained in model #8 for $f_{C_2H_2}$ still applies at 10 mbar, the mixing ratios for the other components now apply at different pressure levels, from ~ 40 mbar for dust to ~ 3 mbar for C_2H_6.

A value for H_s/H_a of 0.5 is also consistent with the *IUE* observations in another way. Clarke et al. (1982) observed limb-darkening in a north-south scan of Jupiter in the spectral regions 1600 to 1650 Å, 1700 to 1750 Å, 1800 to 1850 Å, and 1900 to 1950 Å. In all these regions C_2H_2 is the major absorber. They found that in all cases the limb-darkening followed a roughly cosine dependence. For a backscattered reflectivity in the range of 0.15, as applies to this spectral region, there would be very little limb-darkening for a homogeneous atmosphere. Limb-darkening profiles for the cases H_s/H_a = 0.5, 1.0, and 2.0 are displayed in Figure 2.9 for values of $I/F \sim 0.15$ at $\mu = \mu_0 = 1.0$. It is seen that for H_s/H_a = 0.5 the dependence is most cosine-like, in agreement with the result of the *IRIS* comparison. However, this same cosine dependence could also be obtained if the mixing ratio of C_2H_2 generally increases from the equator toward the poles. For example, if the atmosphere were vertically homogeneous and the single-scattering albedo were to vary with latitude such that $\tilde{\omega}_0 \approx 0.6\cos(\text{latitude})$, the limb-darkening would be approximately cosine. So although we favor the inhomogeneous atmosphere with H_s/H_a = 0.5, we cannot rule out other possibilities. The upper limit derived for the Lyman band

Figure 2.8

The mixing ratios and upper limits to mixing ratios derived in this study. The horizontal error bars are from Table 2.1 and the vertical error bars are obtained from the dimensions of the intersection regions (see Figure 2.5). Also shown are the values obtained by *IRIS* experiment on *Voyagers* 1 and 2 (Maguire, 1981).

Figure 2.9

Limb darkening curves for the cases $H_e/H_a = 2.0$, 1.0, and 0.5 with I/F ($\mu = \mu_0 = \cos 20°$, $\varphi - \varphi_0 = 180°$) approximately equal to 0.15.

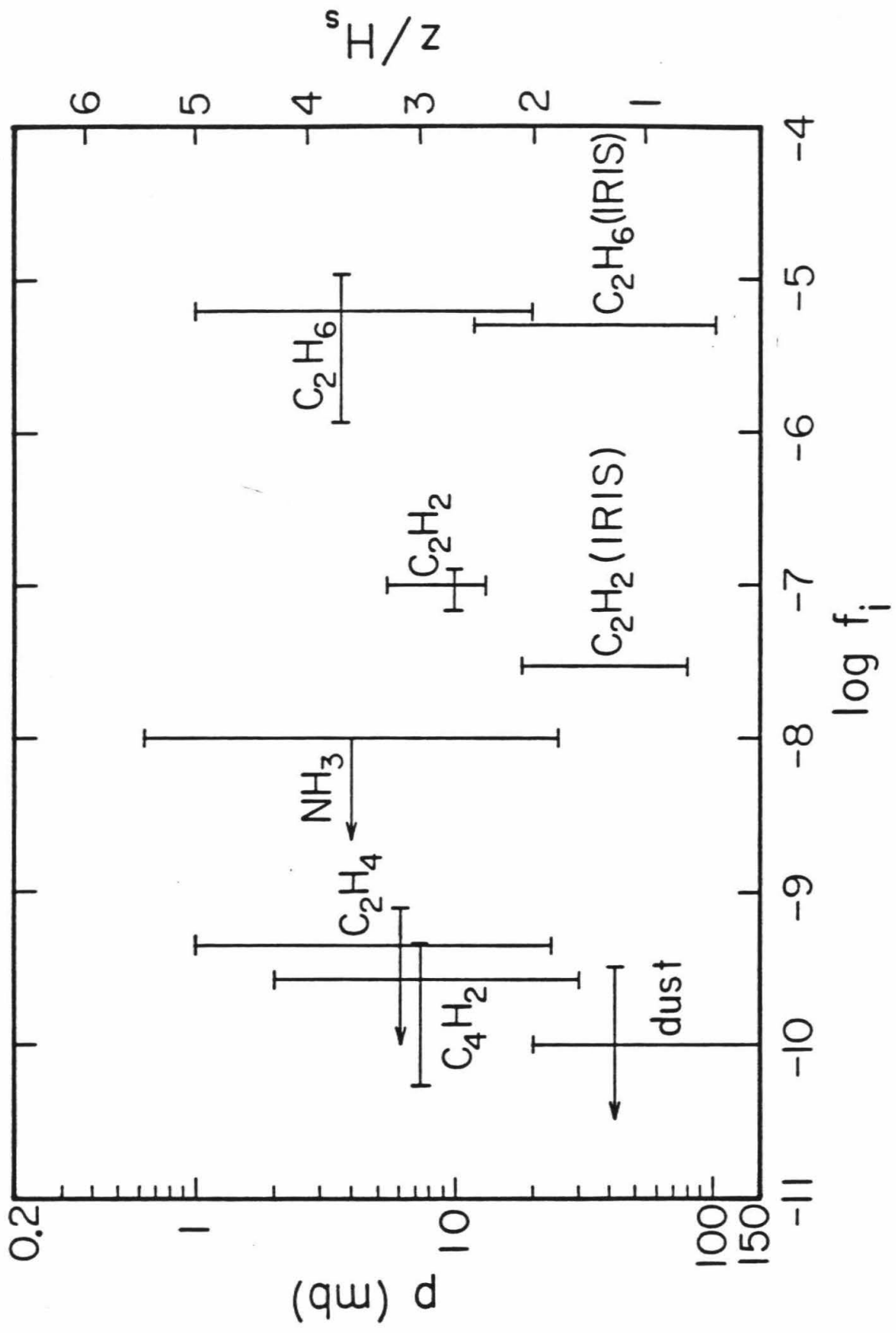
p (mb)
0.2
1
10
100
150
log f_i
-4
-5
-6
-7
-8
-9
-10
-11
H_s/z
1
2
3
4
5
6
C_2H_6(IRIS)
C_2H_6
C_2H_2
C_2H_2(IRIS)
NH_3
C_2H_4
C_4H_2
dust

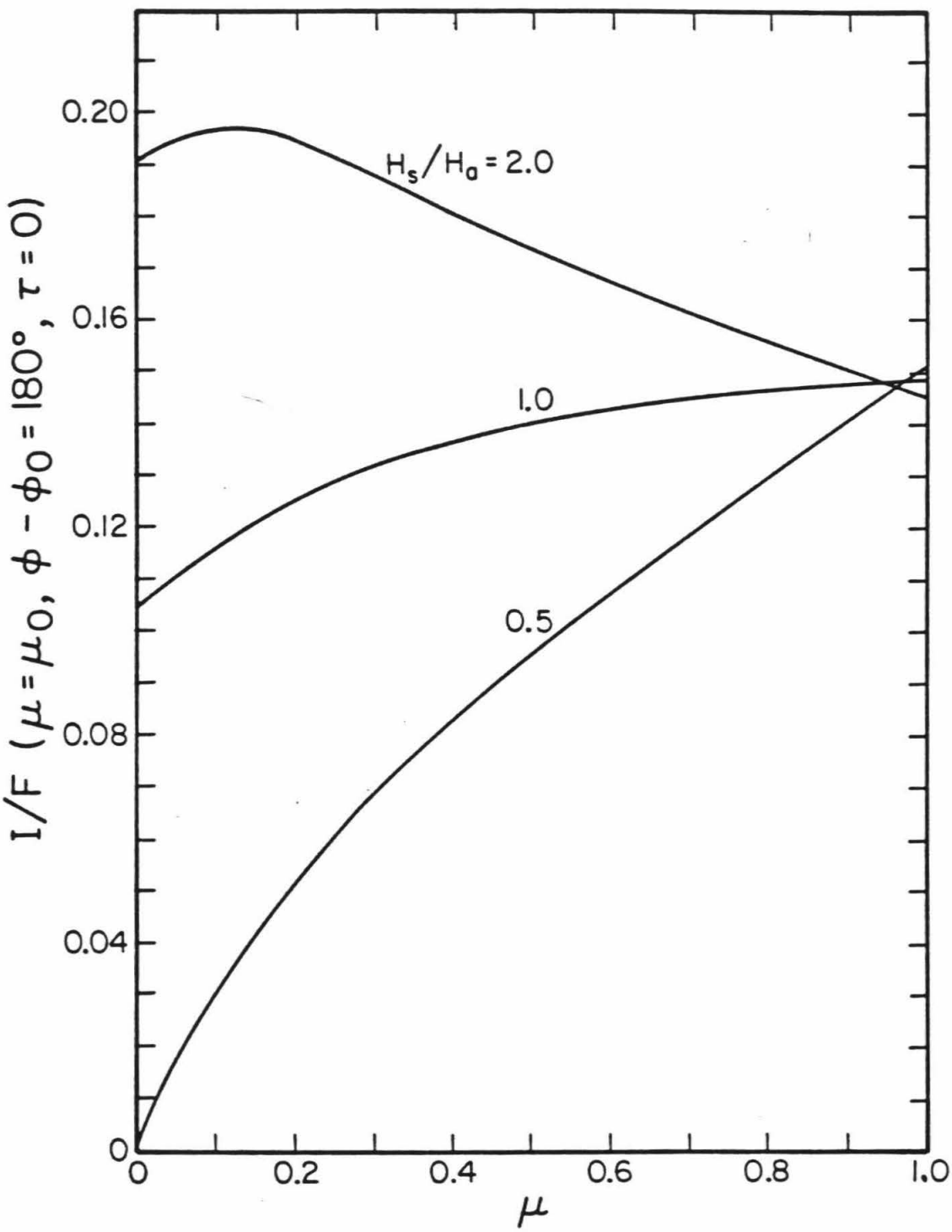
0.20
0.16
0.12
0.08
0.04
0
0
0.2
0.4
0.6
0.8
1.0
$H_s/H_a = 2.0$
1.0
0.5
$I/F\ (\mu=\mu_0,\ \phi-\phi_0=180°,\ \tau=0)$
μ

emission, 1.4± 2.4 kR is consistent with the 2.8 ± 1.0 kR observed by the ultraviolet spectrometer (*UVS*) experiment on *Voyagers* 1 and 2 (Broadfoot et al. 1981) for the total Werner and Lyman band emission.

2.5 Conclusions

From our analysis of the reflected spectrum of Jupiter from 1500 Å to 1740 Å we have obtained mixing ratios for C_2H_2, C_2H_6,C_4H_2, and upper limits on the mixing ratios of C_2H_4, NH_3, and dust in the Jovian atmosphere at ~ 10 mbar. It is possible that there is an appreciable amount of haze affecting the reflection spectrum, since very good model fits are obtained when dust is included. The scale height of C_2H_2 in this region is ~ 2 times the scale height of the bulk atmosphere, while it appears that C_2H_6 may be well-mixed. To improve on these results it will be neccessary to obtain limb profiles in not only a North-South direction, as has been done by Clarke et al. (1982), but also in an East-West direction. High quality measurements of this type would probably allow the determination of the scale height of each individual absorber.

We obtain a marginal value of $1.4 \pm {}^{2.4}_{1.4}$ kR for the H_2 Lyman band dayglow emission. The uncertainty is large because most of the spectrum we are modeling is due to reflected light. If there were enough signal to model below 1525 Å we could obtain a much better result. Our value is consistent, however, with the 2.8± 1.0 kR observed by the *UVS* experiment on *Voyagers* 1 and 2 (Broadfoot et al. 1981) for the total Werner and Lyman band dayglow emission.

Chapter 3

He 584 Å Resonance Reflection from Jupiter

3.1 Introduction

The ultraviolet spectrometer (*UVS*) experiments aboard *Voyagers* 1 and 2 and the ultraviolet photometer aboard *Pioneer* 10 observed He 584 Å emission from the disk of Jupiter. McConnell et al. (1980) report that on about March 3, 1979 (62/79), the *Voyager* 1 *UVS* instrument detected 5.5 Rayleighs ± 30% (1 Rayleigh = 1 R = 10^6 photons cm^{-2} s^{-1}) from the central region of the disk of Jupiter at a phase angle of about 15°. A similar observation was made by *Voyager* 2 *UVS* instrument which on about July 7, 1979 (188/79) detected 3.9 R ± 20% from the central region of the Jovian disk at a phase angle of about 17°. During the encounter of *Pioneer* 10 with Jupiter on December 3, 1973 (337/73) the ultraviolet photometer observed a disk-averaged intensity of 5.1 R (Carlson and Judge, 1974).

The *Voyager UVS* instrument has a resolution of ~33 Å, making identification of the He 584 Å relatively unambiguous. The *Pioneer* 10 instrument, however, is broad band and the possibility exists of contamination by other emissions at nearby wavelengths. The response of the 584 Å channel is down by a factor of 1000 at 1216 Å, so Lyman alpha will not contribute significantly. The next line in the helium series is at 537 Å, but the solar emission line is not very strong (Behring et al., 1976). Io torus emissions would only contribute to the background, and at the time of observation Io was ~8° away from the instrument aperture (Carlson and Judge, 1974). Only auroral emissions could significantly affect the observation. We have no way to estimate the auroral contribution to the He 584 Å intensity other than comparison with *Voyager* results. Since the *UVS* instrument saw no large auroral signal at

wavelengths less than ~ 700 Å, we will assume that the 5.1 R signal observed by *Pioneer* is entirely due to resonantly reflected solar 584 Å photons.

In this chapter these observations will be modeled to yield values for the eddy diffusion coefficient near the homopause in Jupiter's low latitude regions. The results obtained here will be compared with the results obtained by McConnell et al. (1980) and by Carlson and Judge (1976).

3.2 The Solar He 584 Å Line

The formation region on the sun of the 584 Å emission line is the chromosphere, at temperatures of between 10,000 and 50,000 K. The temperature of the scattering region on Jupiter is probably in the range of 200-500 K, and there is strong absorption by H_2 at this wavelength, so that only the central core of the solar line will be scattered. It has recently been determined by Phillips et al. (1982) that self absorption removes about 10% of the core of the solar line. Whether the self-reversed part of the core is narrow or broad is not known. In our modeling we ignore this effect and assume a Gaussian profile for the solar line, determined by its full width at half maximum (FWHM) and by the line-integrated intensity for the solar disk.

The total intensity of solar He 584 Å has been measured for many years, mainly by Hinteregger (Hinteregger, 1977; Hinteregger, 1979; Torr et al., 1979) and most of these measurements are plotted in Figure 3.1a. The scatter in the points and the increase from 1974 to 1979 is real and shows the effects of both day-to-day solar variability (due to solar rotation, creation and destruction of sunspots, flares, etc.) and the 11-year solar cycle. From this graph we estimate that the line-integrated fluxes of the solar disk at the Earth during the encounters of *Pioneer* 10 (*P*10), *Voyager* 1 (*V*1) and *Voyager* 2 (*V*2) with Jupiter were 1.4, 4.1, and 3.5×10^9 photons cm^{-2} s^{-1}, respectively, each with an

Figure 3.1

(a) Measurements of line-integrated He 584 Å solar flux (full disk) as a function of time. Filled circles are taken from Torr et al. (1979). Open circles and crosses are taken from Hinteregger (1977), and refer to active and quiet solar conditions respectively. Crosses are taken from Hinteregger (1979). Filled and open triangles are taken from Phillips et al. (1982) and refer to their rocket flight results (with ± 50% error) and AE-E and AE-C satellite data, respectively.

(b) Measurements of the solar He 584 Å line width as a function of time. Filled and open triangles are taken from Phillips et al. (1982) and represent measurements that are uncorrected and corrected for background radiation and self-reversal, respectively. The filled circle is taken from Doschek et al. (1974).

Also indicated in (a) and (b) are the times of the *Pioneer* and *Voyager* spacecraft encounters with Jupiter.

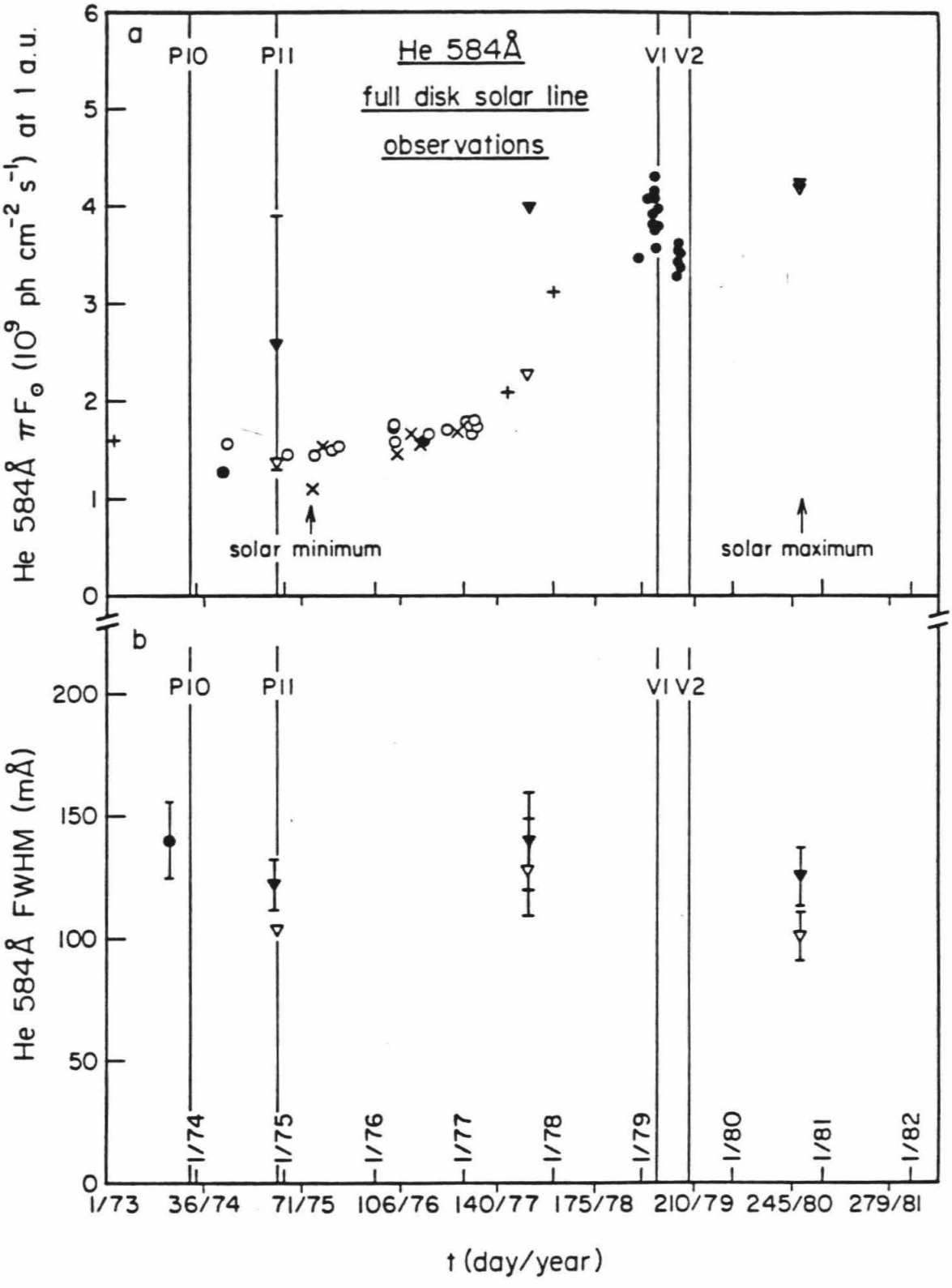
a
P10
P11
He 584Å
full disk solar line
observations
V1 V2
solar minimum
solar maximum
He 584Å πF₀ (10⁹ ph cm⁻² s⁻¹) at 1 a.u.
b
P10
P11
V1 V2
He 584Å FWHM (mÅ)
1/74
1/75
1/76
1/77
1/78
1/79
1/80
1/81
1/82
1/73
36/74
71/75
106/76
140/77
175/78
210/79
245/80
279/81
t (day/year)

uncertainty of approximately $\pm 3 \times 10^8$ photons cm^{-2} s^{-1}.

The width of the solar He 584 Å has been measured only on a few occasions and, unfortunately, none of these were close to the Voyager encounters. Recent work by Phillips et al. (1982) shows that correcting for self-absorption and background effects bring the linewidth estimates down to within the range 100-130 mÅ FWHM. Their results, from measurements made in 1974, 1977, and 1980, along with a measurement made by Doschek et al. (1974) in 1973, are plotted in Figure 3.1b. Using the corrected line-widths of Phillips et al. (1982) we estimate that the linewidth at the *P*10 encounter was 120 mÅ FWHM and the linewidth at the *V*1 and *V*2 encounters was 110 mÅ FWHM. Both these estimates are probably good to ± 15%.

Assuming a Gaussian lineshape, the line-center flux may be obtained by the relation

$$(\pi F_{\odot\lambda_0}) = \frac{(\pi F_\odot)}{\Delta\lambda_\odot} \cdot 2\left[\frac{\ln 2}{\pi}\right]^{\frac{1}{2}} = \frac{0.939(\pi F_\odot)}{\Delta\lambda_\odot} \quad , \tag{3.1}$$

where $\pi F_{\odot\lambda_0}$ is the line-center solar flux; $\pi F_\odot$ is the line-integrated solar flux; and $\Delta\lambda_\odot$ is the solar line width FWHM. From this formula we estimate the line-center solar fluxes in the He 584 Å line at the time of the encounters of *P*10, *V*1, and *V*2 with Jupiter to have been 1.1, 3.4, and 3.0×10^{10} ph cm^{-2} s^{-1} $Å^{-1}$, respectively, each with an uncertainty of ~ 20%.

3.3 Model Jovian Atmosphere

The absorption cross-section of H_2 at 584 Å is 6.0×10^{-18} cm^2 (Hudson, 1971). Assuming a scale height on the order of 50 km, an optical depth of unity will occur at an H_2 number density of about 3×10^{10} cm^{-3}. The homopause level for helium occurs at a number density $n_h \approx n_{H_2 h} \approx b_{He}/K_h$, where K_h is the eddy diffusion coefficient at the homopause and $b_{He} = a_{He} T^{s_{He}}$ is a coefficient

relating the molecular diffusion coefficient of helium to the number density of the atmosphere. From parameters given in Mason and Marrero (1970) we estimate $a_{He} = 5.99 \times 10^{17}$ and $s_{He} = 0.727$. For temperatures in the 200-500 K range b_{He} is from 3-6 $\times$ 10^{19} cm^{-1} s^{-1}. If K_h is between 10^5 and 10^8 cm^2 s^{-1}, then the helium homopause occurs at an H_2 number density of between 6×10^{14} and 3×10^{11} cm^{-3}. Therefore it appears that most of the scattering of the 584 Å line occurs between 2 and 10 scale heights above the homopause.

To obtain the concentration profile of helium we need to solve the continuity equation

$$\frac{\partial n}{\partial t} + \frac{\partial \varphi}{\partial z} = P - nL \quad . \tag{3.2}$$

For helium there is no chemical production or loss, and we assume steady state, so that the flux is constant, i.e.

$$\varphi = \varphi_o = -(D + K)\frac{dn_{He}}{dz} - \left[\frac{D}{H} + \frac{K}{H_{av}}\right] n_{He} - \left[\frac{(1 + \alpha)D + K}{T}\right]\frac{dT}{dz} n_{He} \quad . \tag{3.3}$$

Here φ is the flux of helium (positive upward); D is the molecular diffusion coefficient for helium ($D = b_{He}/n_{H_2}$); K is the eddy diffusion coefficient; n_{He} is the number density of helium; z is altitude; H ($= m_{He}g/kT$) is the scale height of helium; H_{av} ($= \bar{m}g/kT$) is the scale height of the bulk atmosphere (essentially the H_2 scale height); T is temperature; and α is the thermal diffusion coefficient for helium.

In previous studies it has usually been assumed that $\varphi_o = 0$, T = constant, and K = constant. Under these conditions Equation (3.3) is easily solved (Wallace and Hunten, 1973) to yield

$$n_{He}(z) = \frac{f_{He} b_{He}}{K} e^{-\frac{z-z_h}{H_{av}}} \left[1 + e^{+\frac{z-z_h}{H_{av}}}\right]^{1-m_{He}/\overline{m}} , \qquad (3.4a)$$

or equivalently,

$$n_{He}(n) = f_{He}\, n \left[1 + \frac{b_{He}}{K n}\right]^{1-m_{He}/\overline{m}} , \qquad (3.4b)$$

where n is the bulk atmosphere number density ($\approx n_{H_2}$); f_{He} is the mixing ratio of helium in the well-mixed region of the atmosphere, far below the homopause; m_{He} is the mass of helium; and $\overline{m}$ is the mean mass of the atmosphere (assumed to be constant, with $\overline{m} = m_{H_2}$).

In the region of the homopause, however, the temperature gradient of the atmosphere is quite high, perhaps as much as 1 K km^{-1} (Festou et al., 1981). Also, it is quite possible that the eddy diffusion coefficient varies near the homopause. For the case of an atmosphere in which temperature is proportional to altitude (linear-T) and K is proportional to n^{-p} where $0 \lesssim p < 1$, Equation (3.3) can be solved to yield

$$n_{He}(z) = \frac{f_{He} b_{He}}{K_h}\left[1 + \frac{(z - z_h)A}{T_h}\right]^{-(\overline{m}g/kA + 1)} \times$$

$$\times \left[1 + \left[1 + \frac{(z-z_h)A}{T_H}\right]^{\left\{(\overline{m}g/kA+1)(1-p)+s_{He}\right\}}\right]^{-\psi} , \qquad (3.5a)$$

or equivalently,

$$n_{He}(n) = f_{He} n \left[1 + \left[\frac{a_{He} T_{He}^{s_{He}}}{K_h n}\right]^{\left\{(1-p)+\frac{s_{He}}{(\overline{m}g/kA+1)}\right\}}\right]^{-\psi} , \qquad (3.5b)$$

where

$$\psi = \left\{ \frac{(m_{He}/\overline{m} - 1) + \alpha k A/\overline{m} g}{(1-p)(1 + kA/\overline{m} g) + s_{He} kA/\overline{m} g} \right\} . \qquad (3.6)$$

A is defined by

$$T = T_h + A(z - z_h) \qquad (3.7)$$

and p is defined by

$$K = K_n (\alpha_{He} T_h^{s_{He}}/K_h n)^p . \qquad (3.8)$$

Equation (3.5a) or (3.5b) allows us to create model atmospheres that test the effects of temperature gradients and variable eddy diffusion coefficients, as well as the effects of varying T_h and K_h.

3.4 Radiative Transfer

The He 584 Å line arises when helium atoms are excited from the ground state $1s^2\ ^1S_0$ to the excited state 1s 2p $^1P_1^o$ by absorbing a 584 Å photon and then decay back down to the ground state again by emitting a 584 Å photon in another direction. The phase function for resonant scattering is generally a combination of both Rayleigh and isotropic scattering (see Hamilton, 1947). For the case of He 584 Å it turns out that the scattering phase function is entirely Rayleigh. In our modeling we employ a Rayleigh phase function but we ignore polarization effects. Our backscattered intensities will therefore be low by $\lesssim 5\%$ (van de Hulst, 1980). As noted by Carlson and Judge (1976), the 1s 2p $^1P_1^o$ state of helium may decay to the 1s 2s $^1S_0$ state instead of the ground state, resulting in a single-scattering albedo (ω_{He}) for He 584 Å scattering equal to 0.9989. We ignore this effect in our modeling and assume $\omega_{He} = 1$. In a test of the most highly reflective model the error of this assumption was found to be $\lesssim 1\%$. We assume that all of the helium is in the parahelium (singlet) form. This should be a very good assumption even at low densities, since the reaction

$$He(1s\,2s\,{}^3S_1) + H_2 \rightarrow He(1s^2\,{}^1S_o) + H_2^+ + e \qquad (3.9)$$

is very fast, having a rate of $\sim 3 \times 10^{-11}$ cm^3 s^{-1} at room temperature (Hickman et al., 1977).

We assume monochromatic scattering (MS) as opposed to Voigt complete redistribution (VCR) or, most realistically, angle-averaged partial redistribution (AAPR). Since the solar photons are resonantly backscattered at $\tau_s \sim 1$, there is not a big difference between these three approximations. For one of the most reflective models, we tested relative line-integrated intensities and found MS–AAPR = 11.2% and AAPR–VCR = 4.5%. An isotropic phase function was used in all three of these cases. The line profiles generated by these three approximations are compared in Figure 3.2. Here it may also be seen how narrow the Jovian line is relative to the solar line.

The method of solution of the equation of radiative transfer was described in Chapter 1. For each model atmosphere tested, the He 584 Å was divided into 10 equal sections from line center out to five standard Doppler frequency units. Our standard Doppler unit was defined as

$$\Delta\lambda_D = \frac{\lambda_o^2}{c}\Delta\nu_D = \frac{\lambda_o}{c}\left[\frac{2kT}{m_{He}}\right]^{1/2}, \qquad (3.10)$$

with $T = 150$ K. Thus, for the He 584 Å line, $\Delta\lambda_D = 1.53 \times 10^{-3}$ Å and $\Delta\nu_D = 1.35 \times 10^{10}$ Hz. At the frequency midpoint of each section we calculate the optical depth and single-scattering albedo of the atmosphere at each of 149 altitude levels, ranging from $\tau \lesssim 10^{-3}$ to $\tau = 20$, by the following equations;

$$\tau_\lambda^i = \tau_a^i + \tau_{s\lambda}^i = \sigma_{H_2}\sum_{j=1}^{i} n_{H_2}(z_j)\Delta z_j + \sigma_{He\lambda}\sum_{j=1}^{i} n_{He}(z_j)\Delta z_j \qquad (3.11a)$$

and

Figure 3.2

Calculated He 584 Å line profiles for a highly reflective model of Jupiter. Intensity (10^6 photons cm^{-2} sec^{-1} $Å^{-1}$ sr^{-1}, at $\mu = \mu_0 = 0.9531$) is plotted against wavelength in standard Doppler units ($1x = 1.53 \times 10^{-3}$Å). The profiles show the differences between the three redistribution functions MS (monochromatic scattering), AAPR (angle-averaged partial redistribution), and VCR (Voigt complete redistribution). Also shown is the solar He 584 Å flux profile at Jupiter (10^6 photons cm^{-2} sec^{-1}).

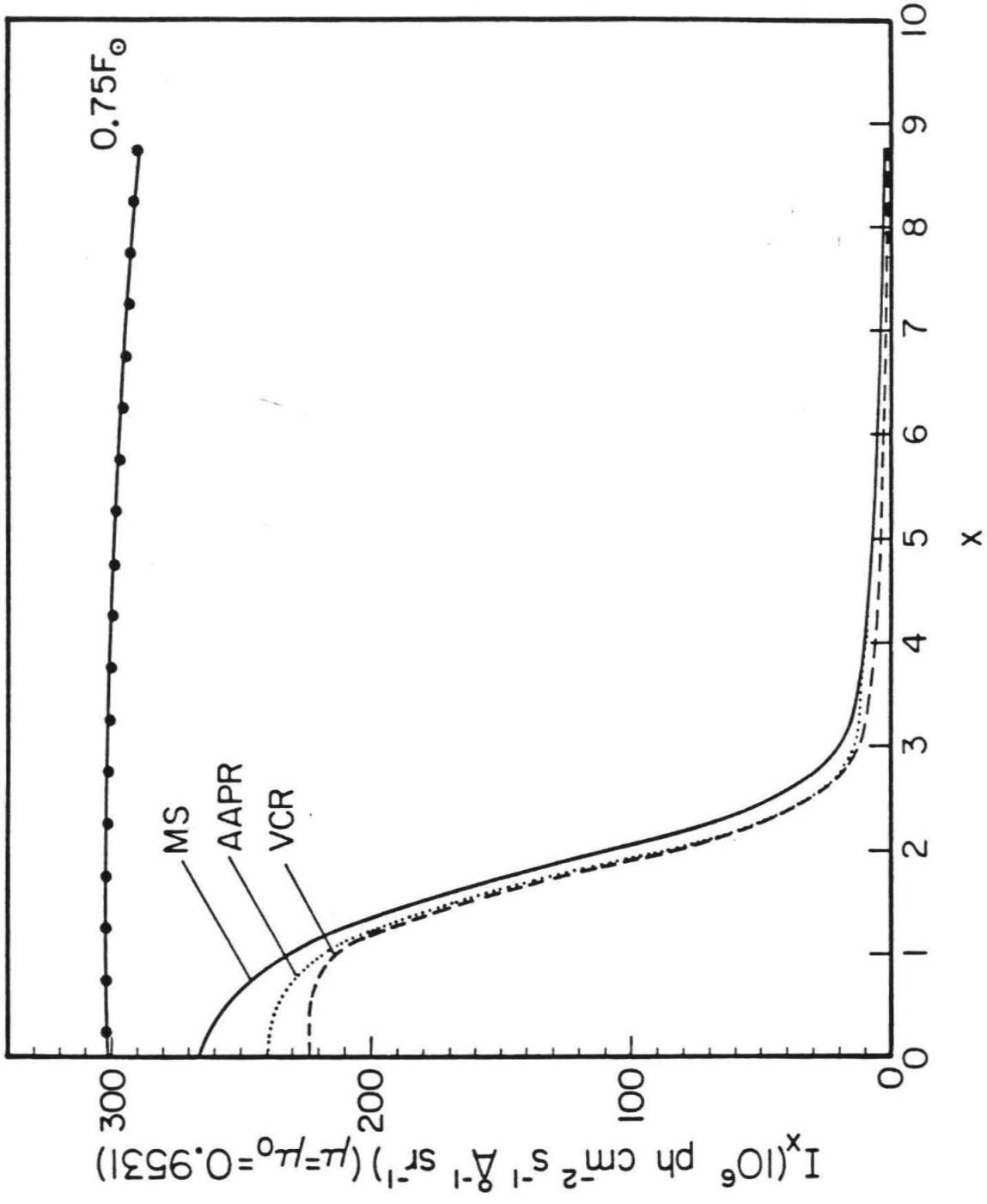
$I_x(10^6$ ph cm^{-2} s^{-1} Å^{-1} sr^{-1}) ($\mu=\mu_o$=0.9531)
0
100
200
300
0
1
2
3
4
5
6
7
8
9
10
x
0.75F$_\odot$
MS
AAPR
VCR

$$\tilde{\omega}^{i}_{o_\lambda} = \left[1 + \frac{\sigma_{H_2} n_{H_2}(z_i)}{\sigma_{He\lambda} n_{He}(z_i)}\right]^{-1} . \qquad (3.11b)$$

For a linear-T atmosphere, n_{H_2} is given by

$$n_{H_2}(z) = n_{H_2}(z_h)\left[1 + \frac{A(z - z_h)}{T_h}\right]^{-(\bar{m}g/kA + 1)} = n_{H_2}(T_h)\left[\frac{T}{T_h}\right]^{-(\bar{m}g/kA + 1)} . \qquad (3.12)$$

The values of $n_{He}(z)$ are given by equation (3.5a) or (3.5b), and $\sigma_{He\lambda}$ is given by

$$\sigma_{He\lambda} = \sqrt{\pi}\sigma_{He\lambda_o}\Phi\left[\frac{\Delta\nu_n}{\Delta\nu_D} , \frac{\nu - \nu_o}{\Delta\nu_D}\right] , \qquad (3.13)$$

where

$$\sigma_{He\lambda_o} = \frac{\pi e^2}{mc}\frac{f e^{+(\Delta\nu_n/\Delta\nu_D)^2}}{\sqrt{\pi}\Delta\nu_D} = 3.06 \times 10^{-13}\left[\frac{150}{T(K)}\right]^{1/2} e^{0.0169/T(K)} [\mathrm{cm}^2] , \qquad (3.14)$$

$$\Phi(\alpha, x) = \frac{\alpha}{\pi^{3/2}}\int_{-\infty}^{+\infty}\frac{e^{-u^2}}{(x - u)^2 + \alpha^2}du , \qquad (3.15)$$

and

$$\Delta\nu_n = \frac{A}{4\pi} = \frac{2\pi e^2}{mc\lambda_o^2}\frac{g_1}{g_2}f = 1.43 \times 10^8 \text{ Hz} . \qquad (3.16)$$

The equation of radiative transfer is then solved for each frequency. The solar flux used is given by

$$\pi F_{\odot\lambda}\left[\frac{\nu - \nu_o}{\Delta\nu_D}\right] = \pi F_{\odot\lambda}(x) = \frac{\pi F_{\odot\lambda_o}}{R^2} e^{-\left[\frac{x}{\Delta\nu_\odot/\Delta\nu_D}\right]^2} , \qquad (3.17)$$

where $R = 5.203$, $\pi F_{\odot\lambda_o} = 3.4 \times 10^{10}$ ph cm^{-2} s^{-1} Å, and $\Delta\nu_\odot = 5.79 \times 10^{11}$ Hz. These values of $\pi F_{\odot\lambda_o}$ and $\Delta\nu_\odot$ correspond to the conditions of the solar He 584 Å line at the time of the *V*1 encounter, as discussed in section 3.2. The lower boundary was placed at $\tau_{a_{max}} (= \tau_{H_{2_{max}}}) = 20$, and was given a Lambert reflectivity of zero. To compare with the Voyager observations of the center of the Jovian disk, we calculated the line-integrated intensities for $\mu = \mu_o = 0.9531$,

where μ is the cosine of the emission zenith angle, and $-\mu_o$ is the cosine of the solar zenith angle. The calculated backscattered intensity is expressed in Rayleighs via the relation

$$I_{584}(R) = \frac{4\pi}{10^6}\sum_{i=1}^{10} I_{\lambda_i}(\mu = \mu_o = 0.9531) \cdot 2\Delta\lambda_D \qquad (3.18)$$

We now proceed to the results of the calculations for various model atmospheres.

3.5 Results of Models

Based on the work of Festou et al. (1981) we define our standard model atmosphere as having T_h = 200 K and A = 0.75 K km^{-1}. We choose p = 0.5 and vary the value of K_h. With a lower boundary at $\tau_{a_{max}}$ = 20 the level of the homopause is given by

$$z_n = \frac{T_h}{A}\left[\left(\frac{\tau_{a_{max}}\overline{m}g}{\sigma_{H_2} n_h k T_h}\right)^{-kA/\overline{m}g} - 1\right] . \qquad (3.19)$$

Model atmospheres for the standard case with K_h = 10^5, 10^6, 10^7, and 10^8 cm^2 s^{-1} are shown in Figure 3.3. In this figure the z = 0 level corresponds to $\tau_{a_{max}}$ = 20. For these four cases the level of the homopause occurs at -297, -150, -41, and +39 km, respectively. The backscattered intensities calculated for these atmospheres are shown in Figure 3.4, along with the *V*1, *V*2, and *P*10 observations of I_{584}. The *V*2 and *P*10 values have been scaled by the line-center solar fluxes obtained in section 3.2 to for comparison with the model calculations. In addition the *P*10 value has been scaled up by 0.9531/0.6667 to account for limb-darkening, since this observation refers to the entire disk while the *V*1 and *V*2 observations and the model calculations refer to the disk center. This last scaling assumes that the limb-darkening is cosine-like, i.e. it assumes conservative scattering. Given the very high reflectivity observed by *P*10, this is

Figure 3.3

Model H_2 and He number density profiles, referred to a level z_0 at which $\tau_{H_2} = 20$. These models each have $T_h = 200$ K, $A = 0.75$ K km^{-1}, and $p = 0.5$. The value of K_h is 10^5,10^6,10^7,and 10^8 cm^2 s^{-1} for models 1,2,3, and 4, respectively. The open circles mark the levels at which the line center $\tau_{He} = 1$ for each helium profile.

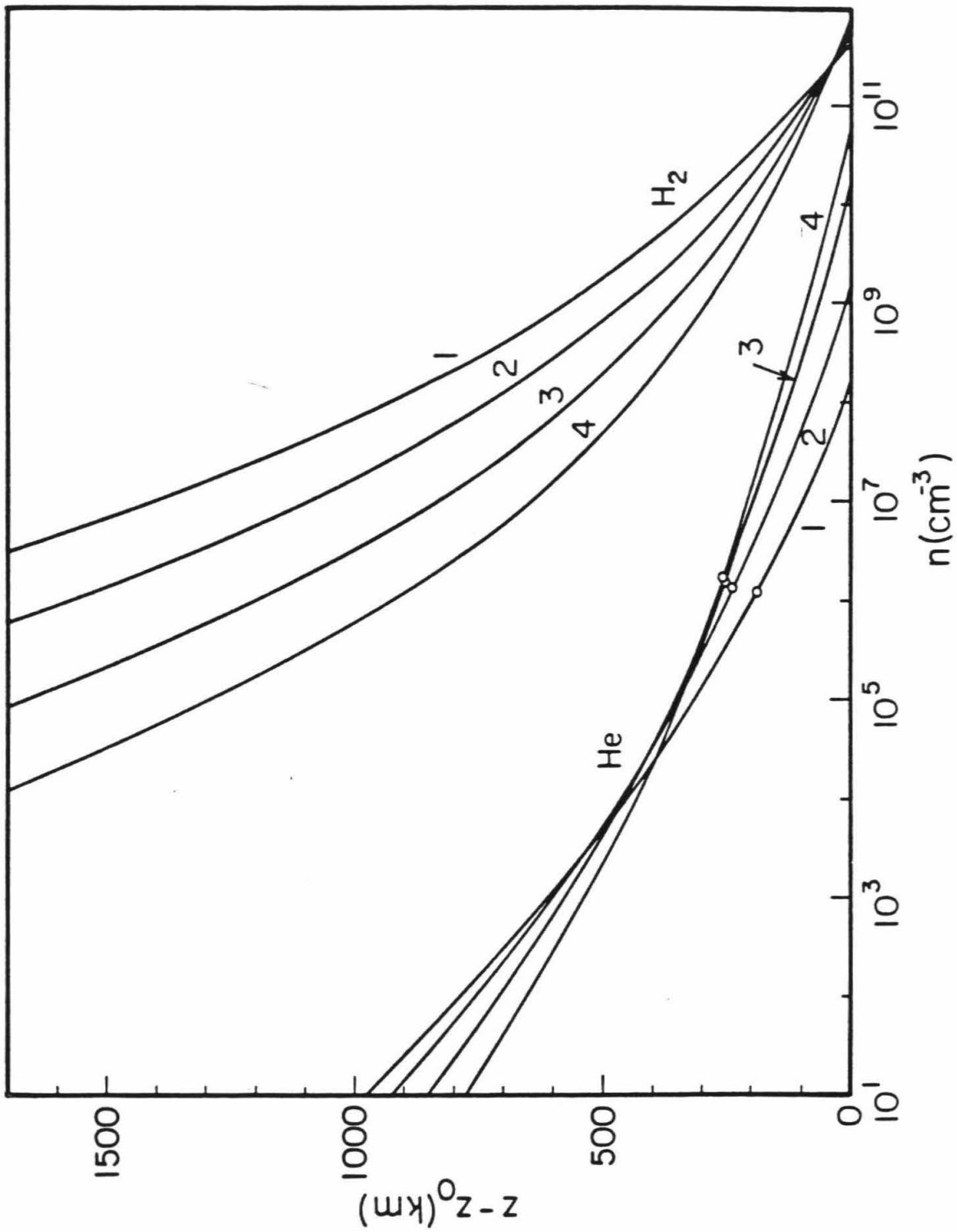
1500
1000
500
0
$z - z_o$(km)
10^1
10^3
10^5
10^7
10^9
10^{11}
n(cm^{-3})
H_2
He
1
2
3
4

Figure 3.4

Line-integrated He 584 Å intensity (Rayleighs) versus eddy diffusion coefficient at the homopause (K_h) for the standard model atmosphere. The model calculations are for $\mu = \mu_0 = 0.9531$. Also shown are the *Pioneer* 10 and *Voyager* 1 and 2 observations. The measurements by *P*10 (Carlson and Judge, 1976) and *V*2 (McConnell et al., 1980) have been scaled to the solar He 584 Å line conditions at the time of the *V*1 encounter with Jupiter.

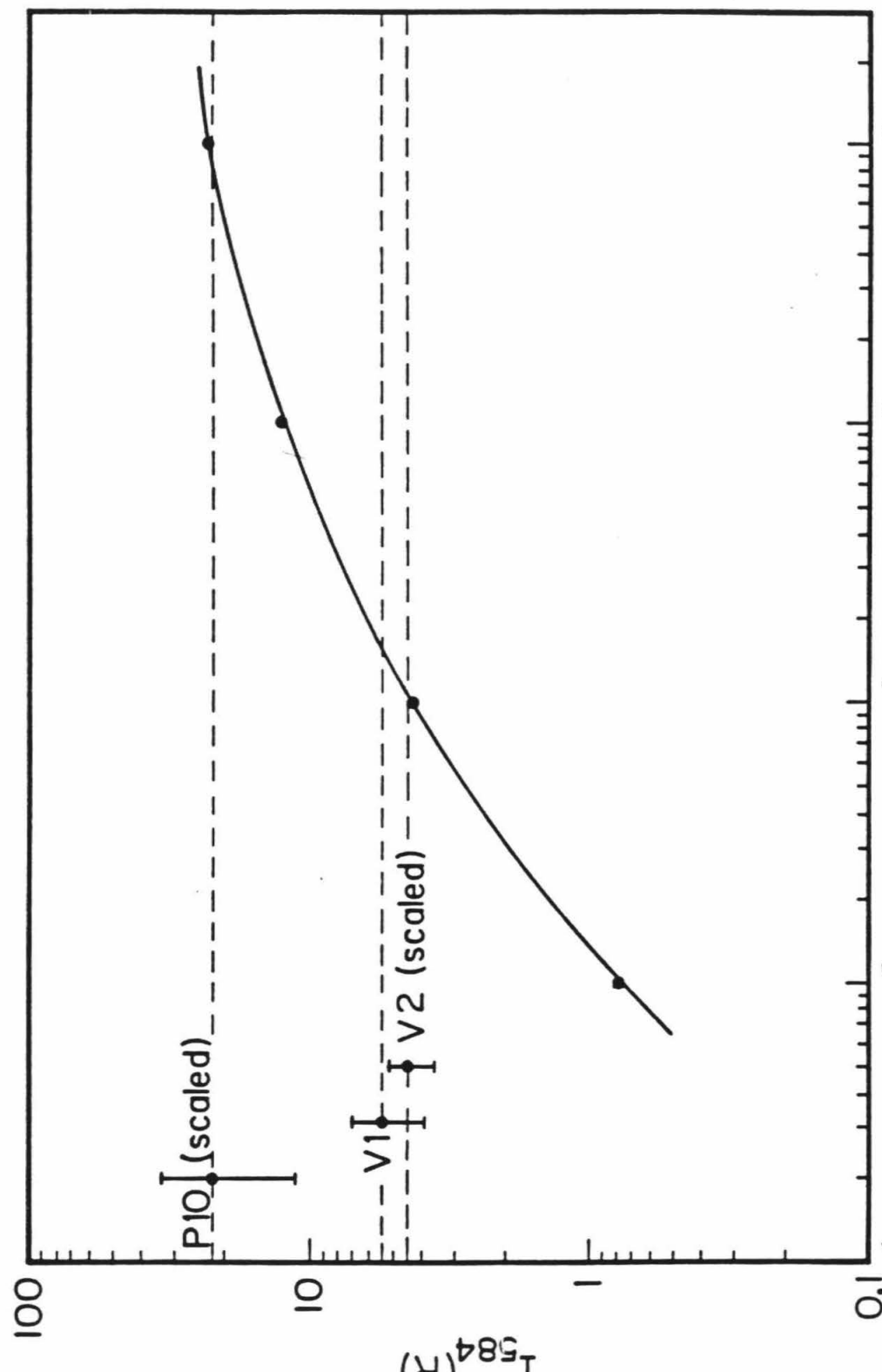
100
10
1
0.1
$I_{584}(R)$
P10 (scaled)
V1
V2 (scaled)
10^4
10^5
10^6
10^7
10^8
$K_h(cm^2\ s^{-1})$

probably a reasonable assumption.

From Figure 3.4 it can be seen that for the standard model atmosphere, i.e. $A = 0.75\ \mathrm{K\,km^{-1}}$, $T_h = 200$ K, and $p = 0.5$, the best estimate for K_h at the time of the $V1$ and $V2$ encounters is $1.3 \times 10^6\ \mathrm{cm^2\,s^{-1}} \pm 30\%$. At the time of $P10$ encounter the standard model atmosphere results in a value of $K_h \approx 10^8\ \mathrm{cm^2\,s^{-1}} \pm \sim 50\%$. To test the effects of variations on the standard model atmosphere, we tried cases in which $A = 0.50\ \mathrm{K\,km^{-1}}$, $A = 1.00\ \mathrm{K\,km^{-1}}$, $p = 0.6$, and $p = 0.7$, while holding K_h fixed at $1.0 \times 10^6\ \mathrm{cm^2\,s^{-1}}$. In each case the difference in brightness with the standard model was less than 7%. The variations were found to be $\Delta I_{584}(R) \sim 0.7\Delta A\ (\mathrm{K\,km^{-1}})$ and $\Delta I_{584}(R) \sim -1.4\Delta p$. It seems that I_{584} has only a second order dependence on the second order quantities p and A. This means that models assuming constant T and K (McConnell, 1980; Carlson and Judge, 1976) are probably quite accurate.

It is possible to obtain a simple, semi-analytic formula for I_{584} in the case of constant T and K. In Chapter 2 we found that for a Rayleigh scattering atmosphere in which the ratio of scatterer-to-absorber scale height was 0.5 that the reflectivity of the atmosphere was given by the empirical formula

$$\frac{I_\lambda}{F_\lambda} = \left[-0.273 \ln\left[1 - \tilde{\omega}_{1_\lambda}\right]\right]^2 \quad (\mu = \mu_0 = 0.9531)\ , \tag{3.20}$$

where πF_λ is the incident flux and $\tilde{\omega}_{1_\lambda}$ is the single-scattering albedo $\tilde{\omega}_{o_\lambda}$ at the level where the scattering optical depth is equal to one ($\tau_s = 1$). Of course the ratio of the scale heights of He to H_2 is only 0.5 well above the homopause, but for most cases this is the region where the scattering occurs. From Figure 3.2 it can be seen that the scattered line has FWHM $\simeq 3\Delta\lambda_D$. Defining

$$1 - \tilde{\omega}_{1_\lambda} = \left[1 + \frac{\sigma_{He\lambda} n_{He}(\tau_{He\lambda} = 1)}{\sigma_{H_2} n_{H_2}(\tau_{He\lambda} = 1)}\right]^{-1} , \tag{3.21}$$

we can approximate I_{584} by

$$I_{584}(R) \approx \left[0.273 \ln\left[1 + \frac{\sigma_{He\lambda_0} n_{He}(\tau_{He\lambda_0} = 1)}{\sigma_{H_2} n_{H_2}(\tau_{He\lambda_0} = 1)}\right]\right]^2 \cdot 3\Delta\lambda_D F_{\odot\lambda_0} \cdot \frac{4\pi}{10^6} . \tag{3.22}$$

Since the atmosphere is isothermal we have

$$n_{H_2}(z) = n_{H_2}(z_h) e^{-\left[\frac{z - z_h}{H}\right]} \tag{3.23}$$

and

$$n_{He}(z) = n_{He}(z_h) e^{-2\left[\frac{z - z_h}{H}\right]}$$

$$= \frac{f_{He}(z_h)}{n_{H_2}(z_h)} \cdot n_{H_2}^2(z) . \tag{3.24}$$

The level $\tau_{He\lambda_0} = 1$ is defined by $n_{He} = \left[\sigma_{He\lambda_0} \frac{H}{2}\right]^{-1}$, so that we have

$$\frac{\sigma_{He\lambda_0} n_{He}(\tau_{He\lambda_0} = 1)}{\sigma_{H_2} n_{H_2}(\tau_{He\lambda_0} = 1)} = \frac{1}{\sigma_{H_2}} \left[\frac{2\sigma_{He\lambda_0} f_{He}(z_h) K}{a_{He} T^{s_{He}} H}\right]^{1/2} , \tag{3.25}$$

where $n_{H_2}(z_h) = a_{He} T^{s_{He}}/K$ as before. Using already defined values and noting that $f_{He}(z_h) = \frac{1}{2} f_{He} = 0.055$ from Equation (3.4b), we arrive at

$$I_{584}(R) \approx 0.142 T^{0.5} \left[\ln\left(1 + 1.05 K^{0.5} T^{-1.11}\right)\right]^2 , \tag{3.26}$$

using the solar line parameters appropriate to $V1$ encounter. We have tested this formula for the four combinations of T = 150 K, T = 500 K, $K = 10^6$ cm^2 s^{-1}, and $K = 10^8$ cm^2 s^{-1}. We find that Equation (3.26) is accurate to within 10%, the accuracy being worst for the case T = 150 K, $K = 10^8$ cm^2 s^{-1}, as would be expected from our approximation of $H_{He}/H_{H_2} = 0.5$. Actually, for these low-T,

high-K conditions $\tilde{\omega}_1 \gtrsim 0.9$, so that Equation (3.20) overestimates I_λ/F_λ (see Chapter 2). This actually works to our advantage, since we expect I_λ/F_λ to be greater in these cases since H_{He}/H_{H_2} is closer to 1 than to 0.5 near the homopause.

Curves generated by equation (3.26) for T = 150 K, 500 K, and 1000 K as a function of K are shown in Figure 3.5 against the correctly scaled results of McConnell et al. (1980). They used an integral method of solution of the radiative transfer equation, assuming isotropic scattering and VCR. Also shown in Figure 3.5 are the scaled results of Carlson and Judge (1976) who also used an integral method and VCR but used a Rayleigh instead of isotropic phase function.

As seen in this figure, the results of all three calculations are fairly close, given the disparity of the methods used. The results of Carlson and Judge (1976) for T = 150 K are everywhere about 25% higher than our results. The results of McConnell et al. are similar to ours (within a factor of two everywhere) but their curves seem to have steeper slopes (dI_{584}/dK) than our curves do. This is mostly due to their use of isotropic scattering. For isotropic scattering we find that the analogue of Equation (3.20) is

$$\frac{I_\lambda}{F_\lambda} = \left[-0.276 \ln(1 - \tilde{\omega}_{1_\lambda})\right]^{2.266} \quad (\mu = \mu_o = 0.9531) \ . \tag{3.27}$$

Use of this equation gives an estimate of I_{584}

$$I_{584} = -0.145 T^{0.5} \left[\ln(1 + 1.05 K^{0.5} T^{-1.11})\right]^{2.266} \tag{3.28}$$

which agrees quite well with the results of McConnell et al. Again, this approximation does start to become inaccurate when scattering occurs near the homopause (since at the homopause $H_{He} > H_{H_2}/2$), which is true for high K and low T atmospheres.

Figure 3.5

Line-integrated He 584 Å intensity (Rayleighs) versus eddy diffusion coefficient for constant-K, constant-T atmospheres. The semi-analytical expression derived in the text is compared with the calculations of McConnell et al. (1980) and Carlson and Judge (1976), scaled to the solar He 584 Å line center flux obtained in section 3.2 for the time of the $V1$ encounter with Jupiter.

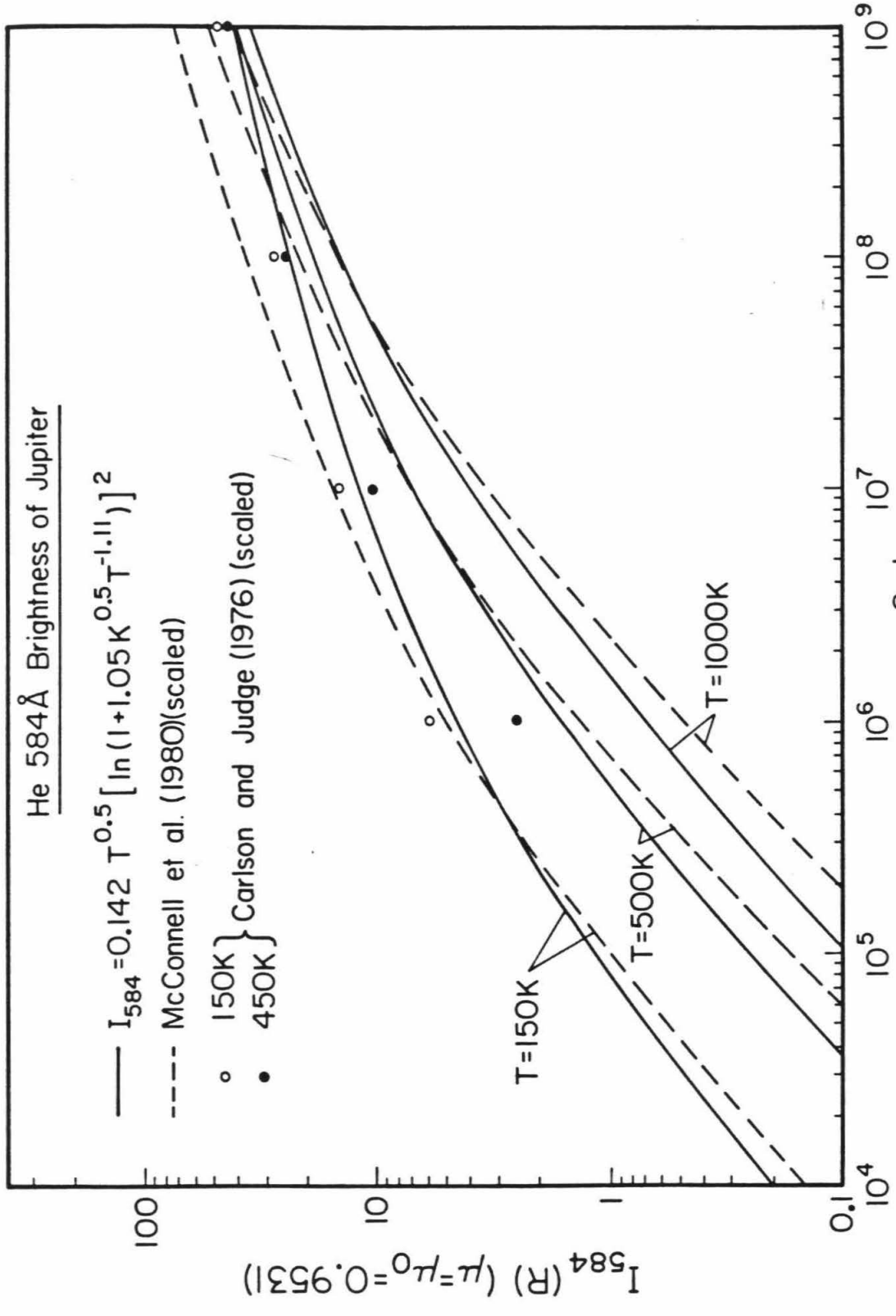
He 584Å Brightness of Jupiter
$I_{584}=0.142\ T^{0.5}\left[\ln(1+1.05K^{0.5}T^{-1.11})\right]^2$
McConnell et al. (1980)(scaled)
150K
450K
Carlson and Judge (1976) (scaled)
T=150K
T=500K
T=1000K
$I_{584}(R)$ $(\mu=\mu_0=0.9531)$
$K(cm^2\ s^{-1})$
100
10
1
0.1
10^4
10^5
10^6
10^7
10^8
10^9

3.6 Conclusions

We have modeled the scattering of the solar He 584 Å line by the upper atmosphere of Jupiter. We find that for a model atmosphere consistent with the temperature profile obtained by Festou et al. (1981) that the value of the eddy diffusion coefficient at the homopause (K_h) was 1.3×10^6 cm^2 s^{-1} ± 30% at the times of the *Voyager* encounters. If this temperature profile was the same during the *Pioneer* 10 encounter then $K_h \approx 10^8$ cm^2 s^{-1} ± 50% at that time. We find that the He 584 Å brightness of Jupiter is primarily sensitive to T_h and K_h. The second order quantities $A = \frac{dT}{dz}$ and $p = -\frac{d\ln K}{d\ln n_{H_2}}$ have only minor effects on the backscattered intensity. For the special case of constant T and K, a good approximation to the He 584 Å brightness of the central region of the disk of Jupiter is given by Equation (3.26).

The decrease in K_h between the *Pioneer* 10 encounter and the *Voyager* encounters is about two orders of magnitude. It is quite conceivable that there exists a link between K_h and the solar cycle. Presumably K_h is due to both turbulence and vertical winds. The component due to vertical winds could be part of a meridional circulation pattern. On the Earth it is known that meridional circulation in the thermosphere is dominated by the effects of Joule heating in the polar regions, resulting in upward flow near the poles and downward flow near the equator (Dickinson et al., 1975; Fuller-Rowell and Rees, 1980). Nishida and Watanabe (1981) have calculated that a single magnetic storm could input as much as 5×10^{24} ergs of Joule heat into the polar regions of Jupiter over a period of about a day. Since the frequency of magnetic storms follows the solar cycle, we might expect the circulation to be more vigorous during solar maximum than solar minimum. If we explicitly include a vertical wind in the flux Equation (3.3), we find a solution for a constant T, constant K

atmosphere similar to Equation (3.4b),

$$n_{\mathrm{He}}(n) = f_{\mathrm{He}} n \left[1 + \frac{n_h}{n}\right]^{1-\frac{m_{\mathrm{He}}}{m}} \cdot \exp\left[\frac{Hw(n)}{K}\right] , \tag{3.29}$$

where $n_h = b_{\mathrm{He}}/K$, for a wind profile given by

$$w(n) = \frac{2w_h}{(1 + n/n_h)} \tag{3.30}$$

with w_h the vertical wind at the homopause. With Equation (3.29) we can estimate I_{584} by

$$I_{584}(R) = 0.142 T^{0.5} \left[\ln\left[1 + 1.05 K^{0.5} T^{-1.11} e^{1.75\times 10^4 \cdot \frac{Tw_h}{K}}\right]\right]^2 \tag{3.31}$$

For T = 200 K, $K = 10^8$ cm^2 s^{-1}, and w_h = 0, conditions that may be appropriate to *P*10 encounter, we get I_{584} = 23.4 R which is close to the scaled *P*10 observation of ~22.4 R. If we hold T and K constant, we find that $w_h \simeq -58$ cm s^{-1} will result in $I_{584} \approx$ 5.0 R, the *V*1 and *V*2 observed value. So it is possible that the difference between the *Pioneer* and *Voyager* observations might be solely due to a difference in meridional circulation. This scenario is somewhat speculative but it can also be made consistent with the increase of observed Lyman-α emission by *V*1 and *V*2 over *P*10, since the enhanced circulation would bring more aurorally produced H to the equatorial regions. We will briefly consider this scenario again in Chapter 4, when we discuss the chemistry of the upper atmosphere of Jupiter.

Chapter 4

Hydrocarbon Photochemistry in the Upper Atmosphere of Jupiter

4.1 Introduction

Early studies by Strobel (1969, 1973, 1975) were the first to predict large abundances of the nonequilibrium hydrocarbon species C_2H_6 and C_2H_2 in the upper atmosphere of Jupiter. More recently, a study by Yung and Strobel (1980) used observations of C_2H_6 and C_2H_2 abundances and the Lyman α brightness to determine vertical mixing properties near the tropopause and near the homopause. Since this last work was done much new data have been obtained on the state of the upper atmosphere of Jupiter (e.g. see Chapters 2 and 3) and many reaction rates involving hdyrocarbons have been updated. In particular the photochemistry of C_2H_2 is much better understood (Okabe, 1981) so that we may now perform realistic calculations of the ethane to acetylene ratio near the tropopause.

In this chapter we use the constraints derived in previous chapters, along with those obtained by other authors, to choose an eddy diffusion profile which best represents the upper atmosphere of Jupiter near solar maximum conditions. We obtain profiles of all the C and C_2 hydrocarbons, as well as atomic hydrogen and helium, and estimate the effects of solar minimum conditions. We will also demonstrate that acetylene photochemistry is capable of yielding the observed amounts of absorbing "Danielson dust" through a slightly modified version of the scheme by Allen et al. (1980) for polyacetylene polymerization. The derived atomic hydrogen and methane profiles are tested with the radiative transfer model of Chapter 1 to make sure they result in a reasonable value for the Lyman α albedo. Finally, we conclude with a brief consideration of the ion-neutral chemistry in the auroral regions.

4.2 Model

The photochemical models presented in this chapter were obtained with the aid of a one-dimensional photochemical-diffusive computer program designed by M. Allen and Y.L. Yung (see Allen et al., 1981). This program solves the continuity equation for a species i

$$\frac{\partial n_i}{\partial t} + \frac{\partial \varphi_i}{\partial z} = P_i - L_i \tag{4.1}$$

in which n_i is the number density, φ_i is the vertical flux, P_i is the chemical production rate, and L_i is the chemical loss rate, all evaluated at altitude z and time t. The altitude z is measured from the visible cloud tops, which occur at a pressure level of ~ 600 mbar. In our models we assume steady-state conditions, so that $\partial n_i/\partial t \rightarrow 0$ and φ_i, P_i, and L_i are diurnal averages. The vertical flux φ_i is defined as it was in Chapter 3 by

$$\varphi_i = -(D_i + K)\frac{dn_i}{dz} - \left[\frac{D_i}{H_i} + \frac{K}{H_{av}}\right] n_i - \left[\frac{(1+\alpha_i)D_i + K}{T}\right]\frac{dT}{dz} n_i \tag{4.2}$$

where D_i is the molecular diffusion coefficient; K is the eddy (turbulent) diffusion coefficient; H_i and H_{av} are the species and bulk atmosphere scale heights, respectively; α_i is the thermal diffusion parameter; and T is the temperature.

The temperature profile used in all of our models is based on that derived by Festou et al.'s (1981) analysis of the stellar occultation experiment performed by the *Voyager* 2 ultraviolet spectrometer (*UVS*) instrument. This experiment occurred during the *Voyager* 2 encounter with Jupiter on July 9, 1979 and the derived temperature profile pertains to a latitude of ~ 17° north at a local time of ~ 1-2 hours before midday. This profile is shown in Figure 4.1 along with a profile of hydrostatic pressure. It may be seen that the temperature is fairly cool throughout the stratosphere and mesosphere but

Figure 4.1

Temperature and pressure as a function of altitude in the standard model atmosphere. Altitudes are measured from the visible cloud tops at a pressure level of ~ 600 mbar. Photochemical calculations begin at the tropopause, which occurs at a pressure level of ~ 150 mbar.

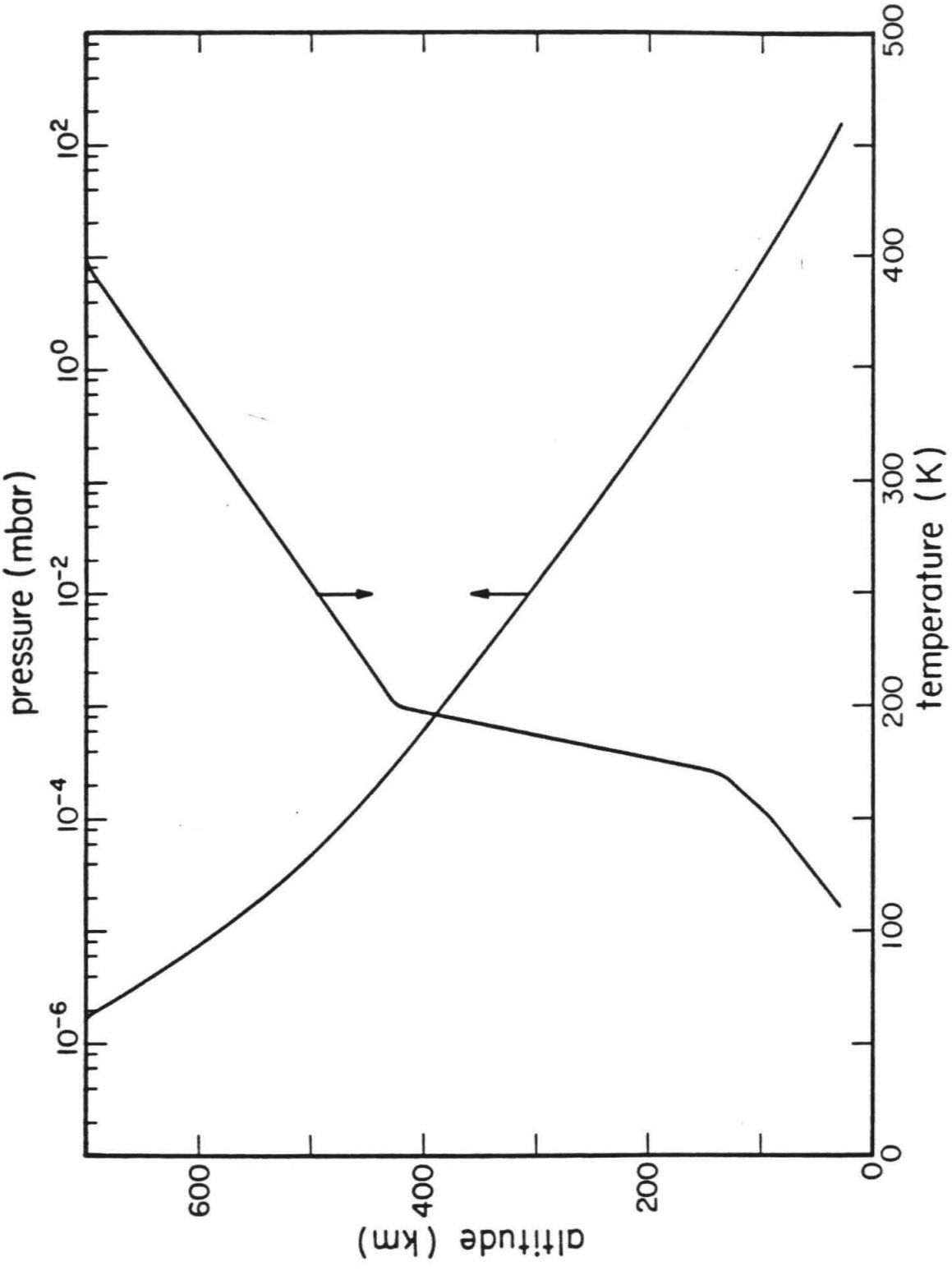
pressure (mbar)
10^{-6}
10^{-4}
10^{-2}
10^{0}
10^{2}
altitude (km)
0
200
400
600
temperature (K)
0
100
200
300
400
500

above that the temperature increases steeply and finally reaches an exospheric temperature of ~1100 K. Below about 130 km the temperature profile is obtained from *Voyager* infrared (*IRIS*) results for the north equatorial belt (Hanel et al., 1979; Maguire, 1981).

The gravity at 17° north is 2356 cm s^{-2} as given by Anderson (1976). Our calculations apply to the region from the tropopause at z = 30 km to z = 700 km (well above the homopause). We hold the gravity fixed over this interval. This introduces an error of ~10% in the calculated total number density at the top of the atmosphere. The centrifugal effect of Jupiter's rotation has a more important effect on the total number density, extending the atmosphere at the equator by a factor of 1.1 over a non-rotating Jupiter (Summers, 1982). The mean mass of the atmosphere changes from 2.22 amu below the homopause to 2.0 amu above due to the diffusive separation of helium. At very large altitudes the mean mass becomes 1.0, but this occurs at number densities ~ 10^6 cm^{-3}, far above the region we are considering.

The values of P_i and L_i in Equation (4.1) are determined by the set of chemical reactions chosen. Our standard model contains 17 species; helium (He), atomic hydrogen (H), molecular hydrogen (H_2), methylidyne (CH), ground state methylene ($^3CH_2$), excited methylene ($^1CH_2$), methyl (CH_3), methane (CH_4), ethynyl (C_2H), acetylene (C_2H_2), vinyl (C_2H_3), ethylene (C_2H_4), ethyl (C_2H_5), ethane (C_2H_6), methylacetylene (CH_3C_2H), butadiyne radical (C_4H), and diacetylene (butadiyne) (C_4H_2). The set of reactions involving these species is presented in Table 4.1 along with the rate coefficients or quantum yields and the references for these. This set includes all important reactions that involve only C and C_2 hydrocarbons. The quantum yields given for C_2H_2 photolysis represent the sum of the quantum yields for the path shown and for the path that results in the products C_2 + H_2. This was done since any C_2 produced will immediately

Table 4.1. Hydrocarbon reactions for the upper atmosphere of Jupiter. The units for two-body and three-body rate coefficients are $cm^3\ s^{-1}$ and $cm^6\ s^{-1}$, respectively. Three body rate coefficients are given by $k = \min(k_o, k_\infty/M)$, where M is the bulk atmospheric number density (molecules cm^{-3}) and k_o and k_∞ are the rate coefficients in the low and high pressure limits, respectively.

	Reaction			Quantum yield or rate coefficient q_{Ly_α}	q_{other}	Reference
R1	$^3CH_2 + h\nu$	→	$CH + H$	1.00	1.00	Okabe, 1978
R2	$CH_3 + h\nu$	→	$^1CH_2 + H$	1.00	1.00	Parkes et al., 1973; 1976
R3a	$CH_4 + h\nu$	→	$^3CH_2 + 2H$	0.51	0	Watanabe et al., 1953;
b		→	$^1CH_2 + H_2$	0.41	1.00	McNesby and Okabe, 1964;
c		→	$CH + H + H_2$	0.08	0	Calvert and Pitts, 1966; Gorden and Ausloos, 1967; Rebbert and Ausloos, 1972; Mount et al., 1977; Slanger, 1982
R4	$C_2H_2 + h\nu$	→	$C_2H + H$	$\lambda < 1500$ Å, 0.40	$\lambda > 1500$ Å, 0.18	Nakayama and Watanabe, 1964; Okabe, 1981; Laufer, 1982
R5a	$C_2H_4 + h\nu$	→	$C_2H_2 + H_2$	0.51	0.51	Zelikoff and Watanabe, 1953;
b		→	$C_2H_2 + 2H$	0.49	0.49	Back and Griffiths, 1967

R6	$C_2H_5 + h\nu$	→	$C_2H_4 + H$	1.00	1.00	Adachi et al., 1979
R7a	$C_2H_6 + h\nu$	→	$C_2H_4 + H_2$	0.13	0.56	Akimoto et al., 1965;
b		→	$C_2H_4 + 2H$	0.30	0.14	Calvert and Pitts, 1966;
c		→	$C_2H_2 + 2H_2$	0.25	0.27	Hampson and McNesby, 1965;
d		→	$CH_4 + {}^1CH_2$	0.25	0.02	Lias et al., 1970;
e		→	$2CH_3$	0.08	0.01	Mount et al., 1978
R8a	$C_4H_2 + h\nu$	→	$C_4H + H$	0.16	0.16	Georgieff and Richard, 1958; Heller and Milne, 1978;
b		→	$2C_2H$	0.04	0.04	Okabe, 1981; Yung et al., 1982b
R9	$H_2 + h\nu$	→	$2H$	1.00	1.00	Mentall and Gentieu, 1970; estimated
R10	$2H + M$	→	$H_2 + M$	$k_{10} = 3.3 \times 10^{-31}\ T^{-0.60}$		Trainor et al., 1973; Prather et al., 1978
R11	$H + CH_4$	→	$CH_3 + H_2$	$k_{11} = 3 \times 10^{-10}\ e^{-6560/T}$		Sepehrad et al., 1979
R12	$H + C_2H_2 + M$	→	$C_2H_3 + M$	k_{12}	$k_o = 6.4 \times 10^{-25}\ T^{-2}\ e^{-1200/T}$ $k_\infty = 9.2 \times 10^{-12}\ e^{-1200/T}$	Payne and Stief, 1976
R13	$H + C_2H_4 + M$	→	$C_2H_5 + M$	k_{13}	$k_o = 1.1 \times 10^{-23}\ T^{-2}\ e^{-1040/T}$ $k_\infty = 3.7 \times 10^{-11}\ e^{-1040/T}$	Michael et al., 1973; Lee et al., 1978

R14	$CH + H_2 + M \rightarrow CH_3 + M$	k_{14}	$k_o = 3.1 \times 10^{-30}\, e^{+457/T}$ $k_\infty = 2.6 \times 10^{-11}$	Butler et al., 1981; Yung et al., 1982
R15	$CH + CH_4 \rightarrow C_2H_4 + H$		$k_{15} = 1.0 \times 10^{-10}$	Butler et al., 1981; Yung et al., 1982b
R16a	$^1CH_2 + H_2 \rightarrow {}^3CH_2 + H_2$		$k_{16a} = 1.0 \times 10^{-12}$	Laufer, 1981a
b	$\rightarrow CH_3 + H$		$k_{16b} = 7.0 \times 10^{-12}$	
R17a	$^1CH_2 + CH_4 \rightarrow {}^3CH_2 + CH_4$		$k_{17a} + 1.6 \times 10^{-12}$	Laufer, 1981a
b	$\rightarrow 2CH_3$		$k_{17b} = 1.9 \times 10^{-12}$	
R18	$^3CH_2 + H + M \rightarrow CH_3 + M$	k_{18}	$k_o = 3.1 \times 10^{-30}\, e^{+457/T}$ $k_\infty = 1.5 \times 10^{-10}$	Yung et al., 1982b
R19	$2\,{}^3CH_2 \rightarrow C_2H_2 + H_2$		$k_{19} = 5.3 \times 10^{-11}$	Banyard et al., 1980; Laufer, 1981a
R20	$CH_3 + H + M \rightarrow CH_4 + M$	k_{20}	$k_o = 3.1 \times 10^{-29}\, e^{+457/T}$ $k_\infty = 1.5 \times 10^{-10}$	Troe, 1977; Patrick et al., 1980; Yung et al., 1982b
R21	$CH_3 + {}^3CH_2 \rightarrow C_2H_4 + H$		$k_{21} = 7.0 \times 10^{-11}$	Laufer, 1981a
R22	$2CH_3 + M \rightarrow C_2H_6 + M$	k_{22}	$k_o = 1.0 \times 10^{-26}\, e^{+506/T}$ $k_\infty = 5.5 \times 10^{-11}$	Callear and Metcalfe, 1976; van den Berg et al., 1976; Yung et al., 1982b

R23	$C_2H + H + M \rightarrow C_2H_2 + M$	k_{23}	$k_o = 3.1 \times 10^{-30}\, e^{+457/T}$ $k_\infty = 1.5 \times 10^{-10}$	Yung et al., 1982b
R24	$C_2H + H_2 \rightarrow C_2H_2 + H$	k_{24}	$1.2 \times 10^{-10}\, e^{-2000/T}$	Laufer, 1981b; Brown and Laufer, 1981
R25	$C_2H + CH_4 \rightarrow C_2H_2 + CH_3$	k_{25}	$2.5 \times 10^{-11}\, e^{-750/T}$	Laufer, 1981b; Brown and Laufer, 1981
R26	$C_2H + C_2H_2 \rightarrow C_4H_2 + H$	k_{26}	3.1×10^{-11}	Laufer, 1981b; Brown and Laufer, 1981
R27	$C_2H + C_2H_4 \rightarrow C_2H_2 + C_2H_3$	k_{27}	$3.4 \times 10^{-11}\, e^{-500/T}$	estimated, based on $C_2H + C_2H_6$
R28	$C_2H + C_2H_6 \rightarrow C_2H_2 + C_2H_5$	k_{28}	$3.4 \times 10^{-11}\, e^{-500/T}$	Laufer, 1981b; Brown and Laufer, 1981
R29	$C_2H_3 + H \rightarrow C_2H_2 + H_2$	k_{29}	1.5×10^{-11}	Keil et al., 1976
R30	$C_2H_3 + CH_3 \rightarrow C_2H_2 + CH_4$	k_{30}	3.0×10^{-12}	estimated
R31	$C_2H_3 + CH_4 \rightarrow C_2H_4 + CH_3$	k_{31}	$1.3 \times 10^{-13}\, e^{-2250/T}$	Yung et al., 1982b
R32	$2C_2H_3 \rightarrow C_2H_4 + C_2H_2$	k_{32}	5.3×10^{-12}	MacFadden and Currie, 1973

R33a b	$C_2H_5 + H$ $C_2H_5 + H + M$	→	$2CH_3$ $C_2H_6 + M$	$k_{33a} = 1.9 \times 10^{-10}\, e^{-440/T}$ k_{33b} $k_o = 5.5 \times 10^{-23}\, T^{-2}\, e^{-1040/T}$ $k_\infty = 1.5 \times 10^{-13}\, e^{-440/T}$	Halstead et al., 1970; Teng and Jones, 1972
R34	$C_2H_5 + CH_3$	→	$C_2H_4 + CH_4$	$k_{34} = 1.9 \times 10^{-12}\, e^{-200/T}$	Teng and Jones, 1972
R35a b	$C_2H_5 + C_2H_3$	→ →	$C_2H_6 + C_2H_2$ $2C_2H_4$	$k_{35a} = 5.0 \times 10^{-12}$ $k_{35b} = 2.0 \times 10^{-12}$	estimated
R36	$2C_2H_5$	→	$C_2H_6 + C_2H_4$	$k_{36} = 2.7 \times 10^{-12}$	Teng and Jones, 1972
R37	$^3CH_2 + C_2H_2 + M$	→	$CH_3C_2H + M$	k_{37} $k_o = 4.0 \times 10^{-26}\, e^{+634/T}$ $k_\infty = 2.2 \times 10^{-12}$	Terao et al., 1963; Laufer, 1981a; Yung et al., 1982b
R38	$CH_3C_2H + H$	→	$CH_3 + C_2H_2$	$k_{38} = 9.7 \times 10^{-12}\, e^{-1550/T}$	von Wagner and Zellner, 1972
R39	$C_4H + H_2$	→	$C_4H_2 + H$	$k_{39} = k_{24}$	estimated
R40	$C_4H + CH_4$	→	$C_4H_2 + CH_3$	$k_{40} = k_{25}$	estimated
R41	$C_4H + C_2H_2$	→	products	$k_{41} = k_{26}$	estimated

react with H_2 to produce C_2H + H. Diacetylene is included to complete the C_2H_2 photochemistry and to indicate the efficiency with which polyacetylenes may be produced (see Allen et al., 1980). Since reaction R8b leads to the recycling of C_2H_2 from C_4H_2, the ratio of the quantum yields of reaction R8a and R8b is crucial to the production of polyacetylenes and to the concentration of acetylene in the lower stratosphere. To our knowledge no measurements have been made of this ratio, so we have made a conservative estimate of 4 for it based on mass spectrometry cracking data for C_4H_2 (Heller and Milne, 1978). We estimate the total quantum yield for dissociation of C_4H_2 to be 0.2 in analogy with C_2H_2.

In the standard model CH_3C_2H is used as a catalyst in the reaction scheme

$$
\begin{array}{lcll}
{}^3CH_2 + C_2H_2 + M & \rightarrow & CH_3C_2H + M & \text{R37} \\
CH_3C_2H + H & \rightarrow & CH_3 + C_2H_2 & \text{R38} \\
\hline
\text{net} \quad {}^3CH_2 + H & \rightarrow & CH_3 & (4.3)
\end{array}
$$

The omission of other reactions for the formation and destruction of CH_3C_2H means that its calculated profile will not be very accurate. Reaction scheme (4.3) is included to provide an indirect mechanism for converting ${}^3CH_2$ into CH_3. This scheme acts as an accessory to the more important reaction R15b in producing methyl radicals from the primary products of methane photolysis. It has now been established that CH_4 does not photodissociate into CH_3 and H directly (Slanger, 1982).

The exclusion of C_3 and higher hydrocarbons could possibly affect the C and C_2 hydrocarbons through fast catalytic cycles, as illustrated by pathway (4.3), or by providing a net sink for carbon, either by heterogeneous processes such as the formation of dust particles or by escape of long-lived species across

the tropopause. However, since the atmosphere is strongly dominated by H_2, the formation of dust via polyacetylene polymerization (or any other mechanism) is inhibited and will not use up much of the carbon reservoir. The most abundant long lived hydrocarbons will be the alkanes since they are saturated with hydrogen. Higher alkanes such as propane (C_3H_8) and butane (C_4H_{10}) are produced very efficiently by three-body recombination of methyl radicals with ethyl or propyl radicals, e.g.

$$CH_3 + C_2H_5 + M \rightarrow C_3H_8 + M \qquad (4.4)$$

$$CH_3 + C_3H_7 + M \rightarrow C_4H_{10} + M \quad . \qquad (4.5)$$

The low-pressure limits for the rates of these reactions are very high (especially at low temperatures) due to the large number of vibrational modes available to C_3H_8 and C_4H_{10} (Yung et al., 1982b). However, the observed alkane abundances fall off roughly as

$$f_{C_nH_{2n+2}} \sim f^n_{CH_4} \quad . \qquad (4.6)$$

This formula holds relatively well for C_2H_6 and gives a good upper limit for C_3H_8. Thus the loss of alkanes across the tropopause is dominated by C_2H_6. In our models the flux of C across the tropopause due to C_2H_6 is $\sim 3 \times 10^9$ C-atoms cm^{-2} s^{-1}. This downward flux is balanced by an upward flux of CH_4.

The possibility of other fast catalytic cycles involving C_3 or higher hydrocarbons cannot be ruled out. It may be said, however, that the number of CC-bond forming reactions is quite small (see Table 4.1) and the abundances of C_3 and higher hydrocarbons are likewise expected to be small, so that their effect on the C, C_2 system is small.

In our study we do not consider the effect of ammonia photochemistry. Near the tropopause NH_3 will provide a source of H via the photodissociation

reaction

$$NH_3 + h\nu \rightarrow (\tilde{X}^2B_1)NH_2 + H \qquad (4.7)$$

(Strobel, 1975). The fate of NH_2 in the lower stratosphere is usually taken to be three-body recombination, either with H to recycle NH_3 or with itself to form hydrazine (N_2H_4) (Atreya et al., 1977). Another possible fate for NH_2 is the reaction

$$CH_3 + NH_2 + M \rightarrow CH_3NH_2 + M \quad . \qquad (4.8)$$

Methylamine (CH_3NH_2) is dissociated by photons up to ~ 2500 Å in wavelength and one of its many photodissociation products is HCN (Gardner, 1981) which has recently been detected on Jupiter (Tokunaga et al., 1981). The major effect of the coupling of the C and N chemistry will thus be too remove CH_3 and add H. Since the mixing ratio of NH_2 predicted by Atreya et al. (1977) is similar to the mixing ratio of CH_3 in the lower stratosphere of our models, the worst we might do by ignoring NH_3 photochemistry is to overestimate the abundance of C_2H_6 in the lower stratosphere by a factor of two.

The upper boundary condition for all species except H was a specification of zero flux. This implies that there are no sources or sinks above the upper boundary. For atomic hydrogen there is a source due to EUV and soft electron dissociation of H_2. Strobel (1973) estimated that the source due to EUV produced a downward flux of H of $\sim 7 \times 10^8$ cm^{-2} s^{-1}. The *Voyager* UVS instrument observed $\sim 2.8 \pm 1.0$ kR of dayglow intensity in the H_2 Werner and Lyman bands (1 kR = 10^6 ph cm^{-2} s^{-1}). If we assume that this emission is due to soft electron ($E \lesssim 100$ eV) impact on H_2, then the emission is optically thin and we can estimate the column production rate as

$$\int P_H dz = \frac{2\mu I_{W+L}(kR) \times 10^9}{4\pi} \approx 2 \times 10^8 \text{ cm}^{-2} \text{ s}^{-1} \quad . \tag{4.9}$$

In this expression μ is the cosine of the local zenith angle of the observer and I_{W+L} is the observed dayglow intensity. In all of our models we take the downward flux of H at the upper boundary to be 1×10^9 cm^{-2} s^{-1}.

For the lower boundary at the tropopause the mixing ratios of H_2, He, and CH_4 are held fixed at 0.89, 0.11, and 1.5×10^{-3}, respectively (Gautier et al., 1981; Gautier et al., 1982; Sato and Hansen, 1979). All the other species with the exception of C_2H_6 are allowed to move across the tropopause with a downward velocity given by K_t/H_t, where K_t and H_t are the eddy diffusion coefficient and the bulk atmospheric scale height, respectively, at the tropopause. This velocity is an estimate of the true velocity which is given by

$$w_{it} = -K_t \left(\frac{1}{n_{i_t}} \frac{dn_i}{dz}\bigg|_{z=z_t} + \frac{1}{H_t} + \frac{1}{T_t} \frac{dT}{dz}\bigg|_{z=z_t} \right) \quad . \tag{4.10}$$

For C_2H_6 we set $w_{C_2H_6 t} = -\frac{K_t}{T_t} \frac{dT}{dz}\Big|_{z=z_t}$, since we expect that ethane is well-mixed in the lower stratosphere and that a significant source of C_2H_6 exists just below the tropopause due to C_2H_2 photolysis. If there actually is a steep gradient in the ethane mixing ratio at the tropopause, the loss of C_2H_6 to the troposphere will be considerably greater than the loss which our models estimate, resulting in a decreased abundance of C_2H_6 in the lower stratosphere.

For the eddy diffusion profile we use the functional form of Chapter 3,

$$K(n) = K_h (n_h/n)^p \tag{4.11}$$

with the values $K_h = 1.3 \times 10^6$ cm^2 s^{-1} and $n_h = 2.17 \times 10^{13}$ cm^{-3}. Since $n = 1.04 \times 10^{19}$ cm^{-3} at the tropopause, we have

$$K_t(p) = 1.3 \times 10^6 \, (2.09 \times 10^{-6})^p \quad . \tag{4.12}$$

For our standard model we set $p = 0.6$, which gives $K_t = 508$ cm^2 s^{-1} and a diffusion time constant $\tau_d \approx H_t^2/K_t \approx 181$ years. We also try models with $p = 0.4$ and 0.5 which yield 6946 cm^2 s^{-1} and 1878 cm^2 s^{-1} for K_t and 13 years and 49 years for τ_d. From a study of temperature perturbations above cloud features Conrath et al. (1981) obtain a vertical mixing time near the tropopause of ~ 20 years (implying $K_t \sim$ 4600 cm^2 s^{-1}). This is only an order of magnitude estimate, however, and given that the observations refer to major cloud features (e.g. the great red spot and the white ovals) the actual planet-wide average might be considerably lower. In a recent study of the reflectivity of stratospheric NH_3 bands using the *International Ultraviolet Explorer* (*IUE*), Fricke et al. (1982) report that an eddy profile given by $K \approx (1-3) \times 10^{13}/n^{\frac{1}{2}}$ cm^2 s^{-1} near the tropopause fits the observations. This formula yields $K_t = (3-10) \times 10^3$ cm^2 s^{-1} or $\tau_d \approx 30-10$ years. However their results are also probably only good to within an order of magnitude since the ammonia profiles they use are strongly dependent on the NH_3 photochemistry. In Figure 4.2 we show the three eddy diffusion profiles used in our models.

The total absorption cross-sections for the major gases in our model are shown in Figure 4.3. The cross-sections are averaged over 50 Å-wide bins for wavelengths longer than 1250 Å. Below 1250 Å irregular bin sizes are used and cross-sections at solar emission lines wavelengths (1216 Å, 1026 Å, 991 Å, 997 Å, and 973 Å) are included separately. The solar fluxes for the standard model are taken from Mount et al. (1980). The diurnally-averaged values of these fluxes and the attenuated fluxes at different levels in the standard model atmosphere are shown in Figure 4.4. It may be seen that most of the solar flux below 1800 Å is absorbed above the tropopause.

Figure 4.2

Eddy diffusion profiles used in the photochemical models. The standard model atmosphere has the profile labelled $p = 0.6$.

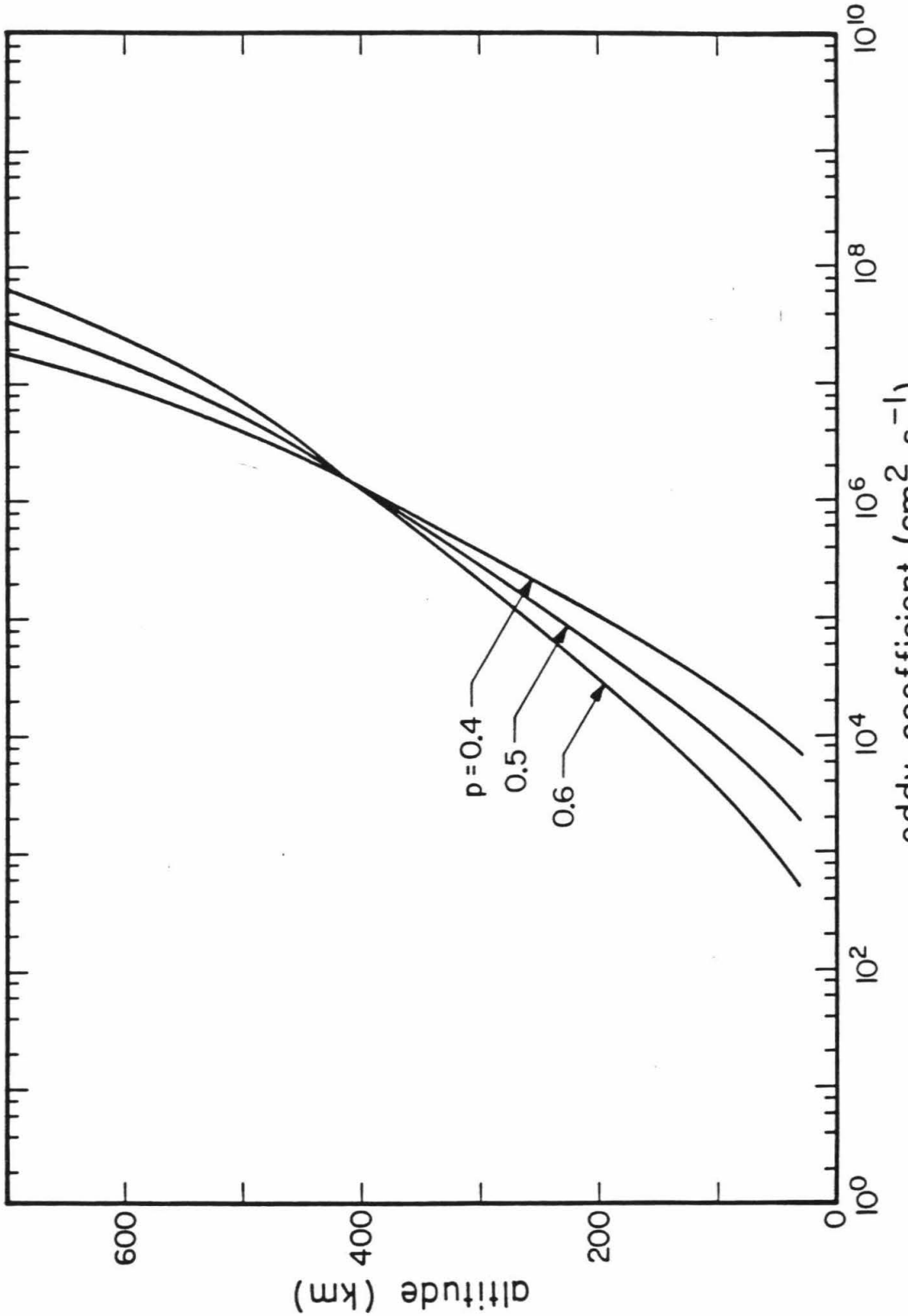
altitude (km)
600
400
200
0
10^0
10^2
10^4
10^6
10^8
10^{10}
eddy coefficient (cm^2 s^{-1})
p=0.4
0.5
0.6

Figure 4.3

Total absorption cross-sections for the major gases of the upper Jovian atmosphere. The cross-sections are averaged over 50-Å wide bins for wavelengths above 1250 Å. Below 1250 Å irregular bin sizes are used. Cross-sections at important solar emission features are included separately. References for the cross-sections are given in Table 4.1.

Figure 4.4

Diurnally-averaged solar fluxes (from Mount et al., 1980) used in the standard model atmosphere. Also shown are the attenuated solar fluxes at 330, 220, and 30 km above the cloud tops.

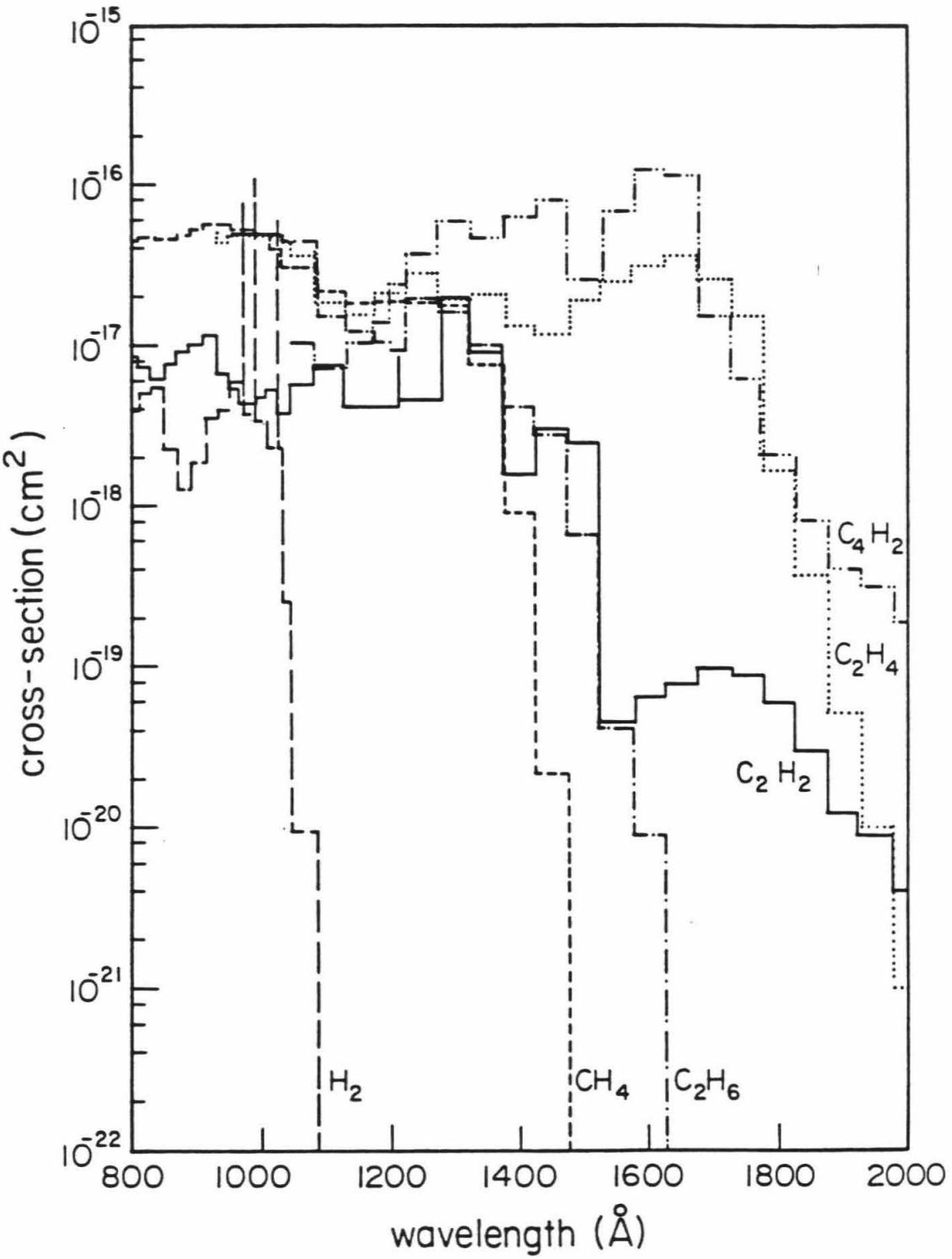
cross-section (cm²)
wavelength (Å)
10⁻¹⁵
10⁻¹⁶
10⁻¹⁷
10⁻¹⁸
10⁻¹⁹
10⁻²⁰
10⁻²¹
10⁻²²
800
1000
1200
1400
1600
1800
2000
H₂
CH₄
C₂H₆
C₂H₂
C₂H₄
C₄H₂

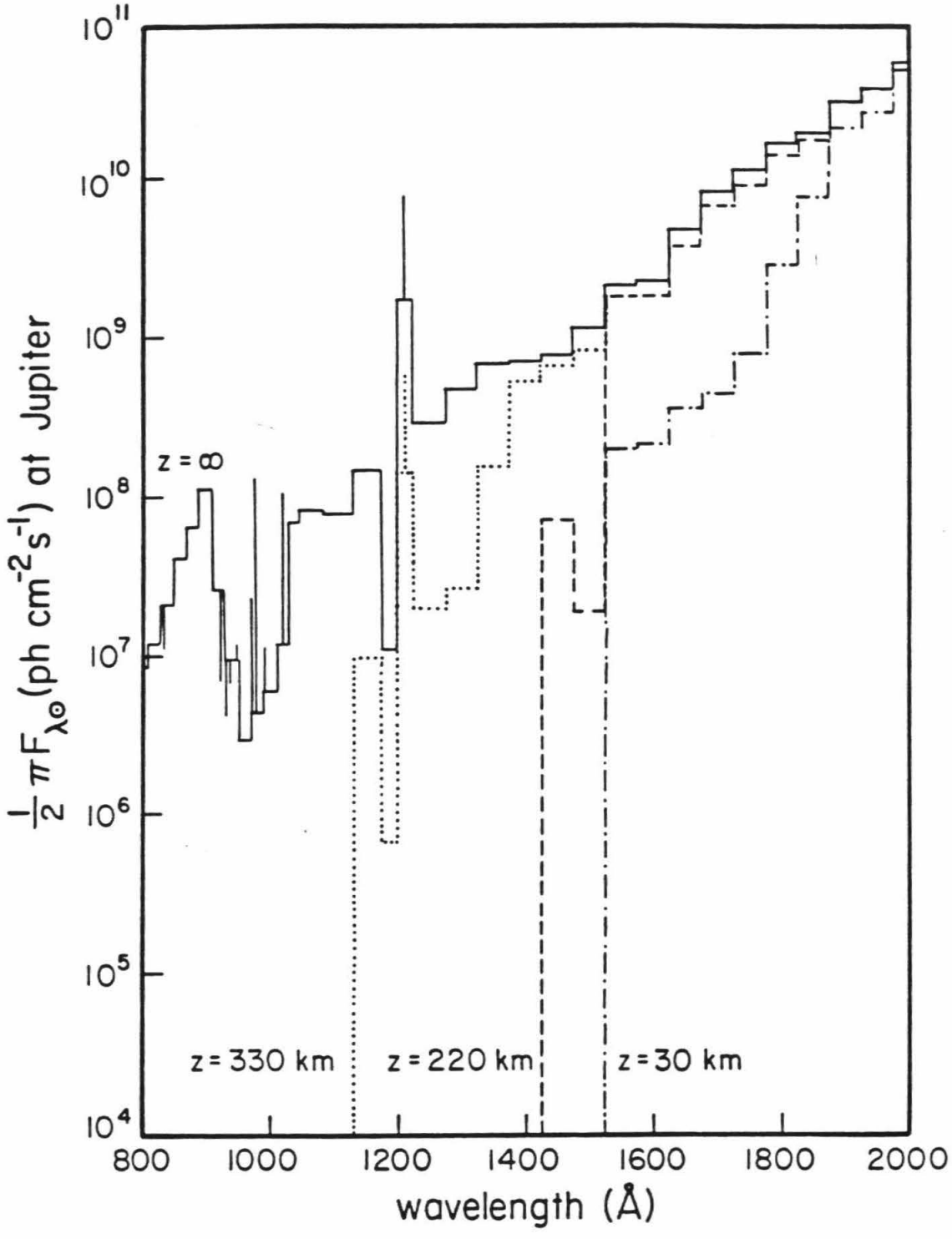
10^{11}
10^{10}
10^{9}
10^{8}
10^{7}
10^{6}
10^{5}
10^{4}
$\frac{1}{2}\pi F_{\lambda\odot}$(ph cm^{-2}s^{-1}) at Jupiter
z = 8
z = 330 km
z = 220 km
z = 30 km
800
1000
1200
1400
1600
1800
2000
wavelength (Å)

4.3 Standard Model Results

We define our standard model as the case in which the eddy diffusion profile is defined by $K = 1.3 \times 10^8 (2.17 \times 10^{13}/n)^{0.6}$. The resulting concentration and mixing ratio profiles for diurnally-averaged conditions are presented in Figures 4.5 and 4.6, respectively. The main features are 1) the homopause, occurring between ~ 400 and 450 km above the cloud tops for the major species; 2) the peak in the H concentration of $\sim 8 \times 10^9$ cm^{-3} occurring ~ 50 km below the homopause; 3) the nearly well-mixed behavior of C_2H_6 in the lower stratosphere with the C_2H_6/C_2H_2 ratio increasing towards the tropopause; and 4) the double peak in the C_2H_4 profile. The CH_3C_2H profile is probably not accurate since the C_3 hydrocarbon chemistry is not complete in our model. Since no loss processes for CH_3C_2H are included other than R38 it is likely that we overestimate its concentration.

The hydrocarbon photochemistry in the upper atmosphere of Jupiter ultimately begins with the photodissociation of CH_4. The carbon-containing fragments of this process are very short-lived chemically. They will undergo a series of reactions that will lead either to 1) the recycling of CH_4 via reaction R20 or 2) the synthesis of C_2 hydrocarbons via reactions R15, R19, R21, or R22. The only reactions which break the C-C bond and return C_2 hydrocarbons to methane are R7d, R7e, and R33a. Of these three reactions R7d and R7e are quite slow (due to shielding of C_2H_6 by CH_4, see Figure 4.3), while reaction R33 manages to return ~ 35% of the C_2 hydrocarbons produced by the reactions R15, R19, R21, and R22. The other ~ 65% represents a net chemical loss of methane to higher hydrocarbons.

Most of the reactions that are left in Table 4.1 are exchange reactions. These are important in determining the equilibrium concentrations of the major

Figure 4.5

Concentration profiles of all standard model atmosphere constituents.

Figure 4.6

Mixing ratio profiles of all standard model atmosphere constituents.

Figure 4.7

J-values of the major gases as a function af altitude in the standard model atmosphere.

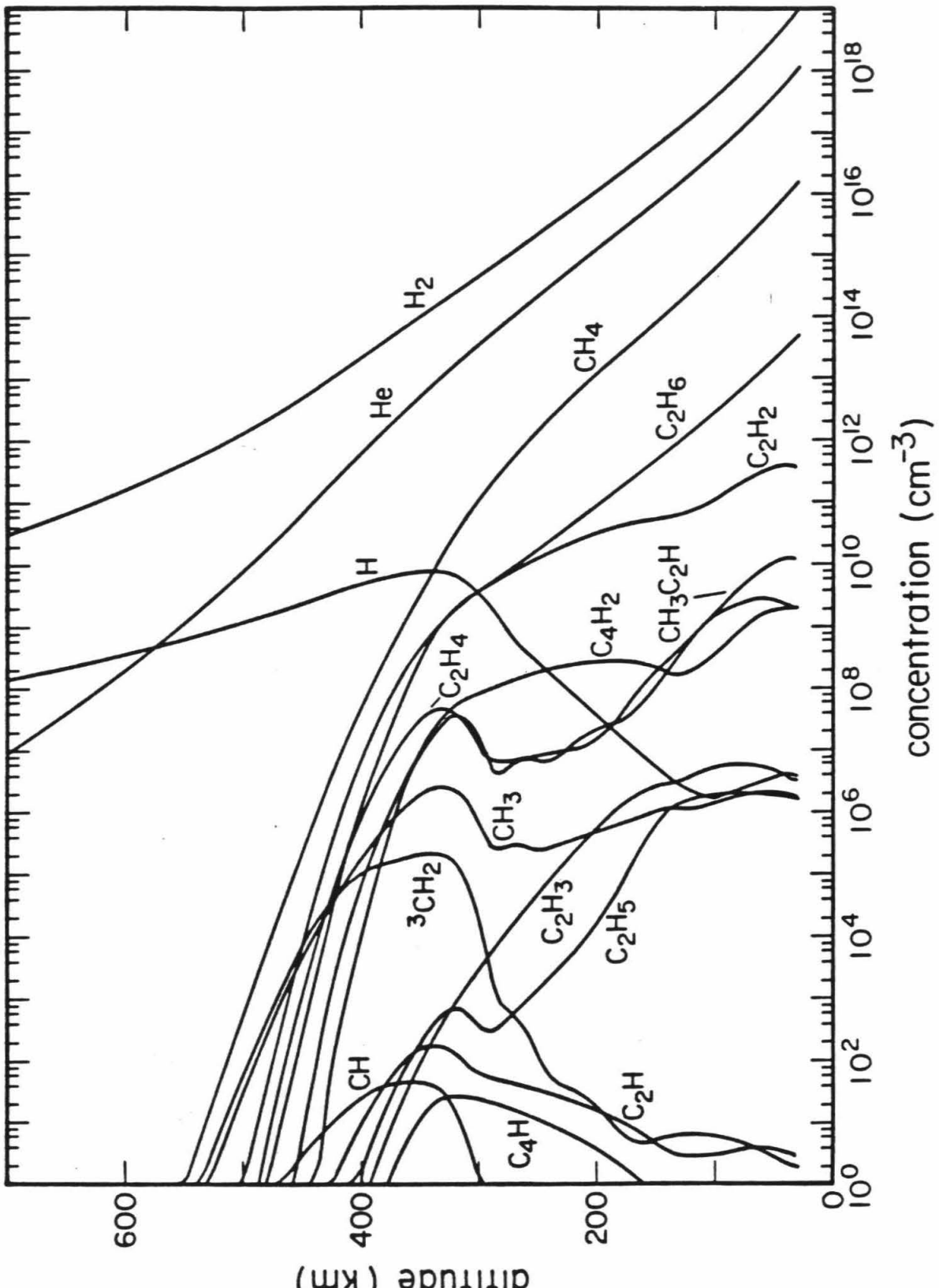
altitude (km)
600
400
200
0
10^0
10^2
10^4
10^6
10^8
10^{10}
10^{12}
10^{14}
10^{16}
10^{18}
concentration (cm^{-3})
H_2
He
H
CH_4
C_2H_6
C_2H_2
C_4H_2
CH_3C_2H
C_2H_4
CH_3
$^3CH_2$
C_2H_3
C_2H_5
CH
C_2H
C_4H

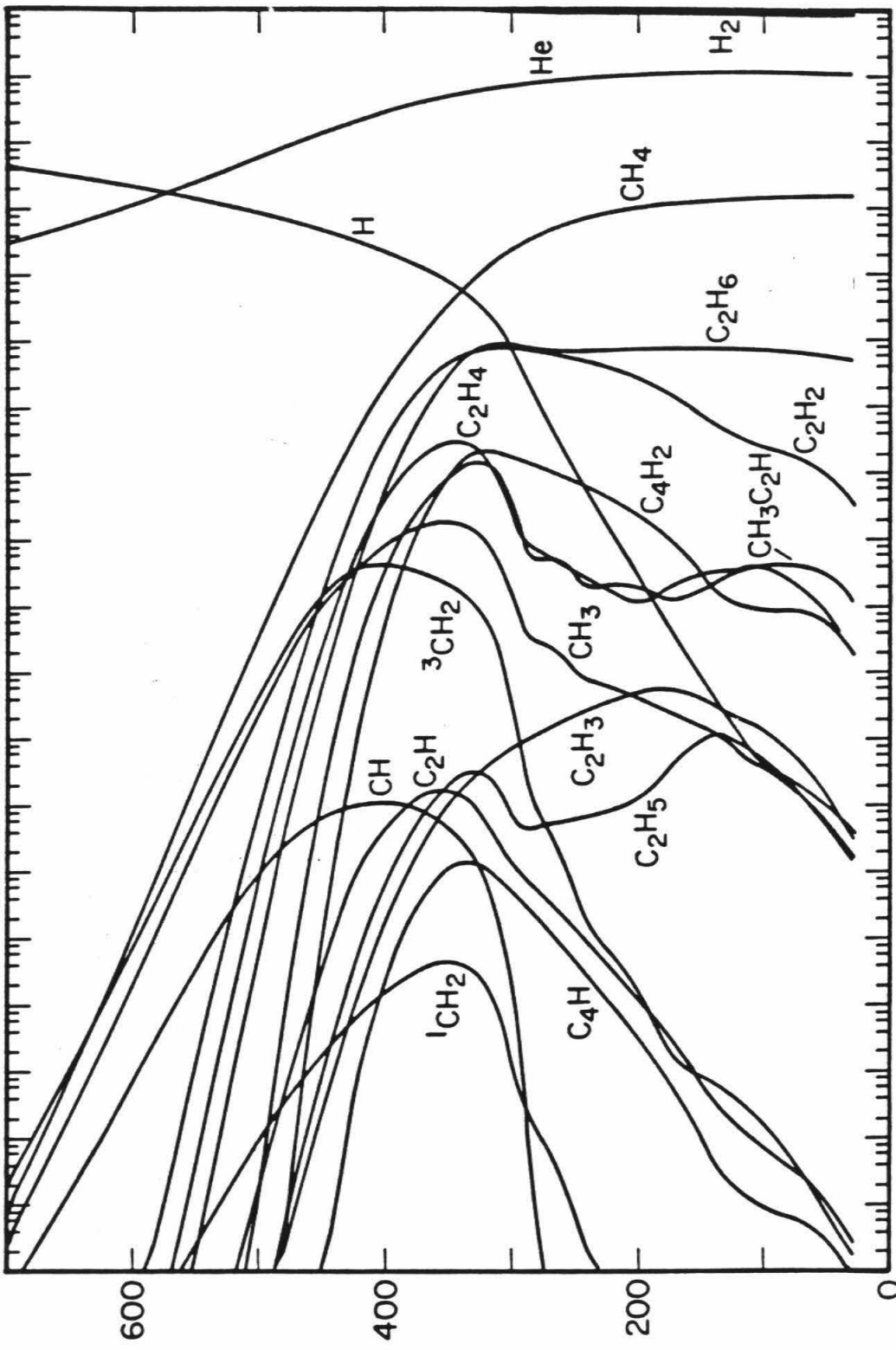
altitude (km)
0
200
400
600
mixing ratios
10^{-18}
10^{-16}
10^{-14}
10^{-12}
10^{-10}
10^{-8}
10^{-6}
10^{-4}
10^{-2}
10^{0}
H
He
H_2
CH_4
C_2H_6
C_2H_4
C_2H_2
C_4H_2
CH_3C_2H
CH_3
$^3CH_2$
CH
C_2H
C_2H_3
C_2H_5
$^1CH_2$
C_4H

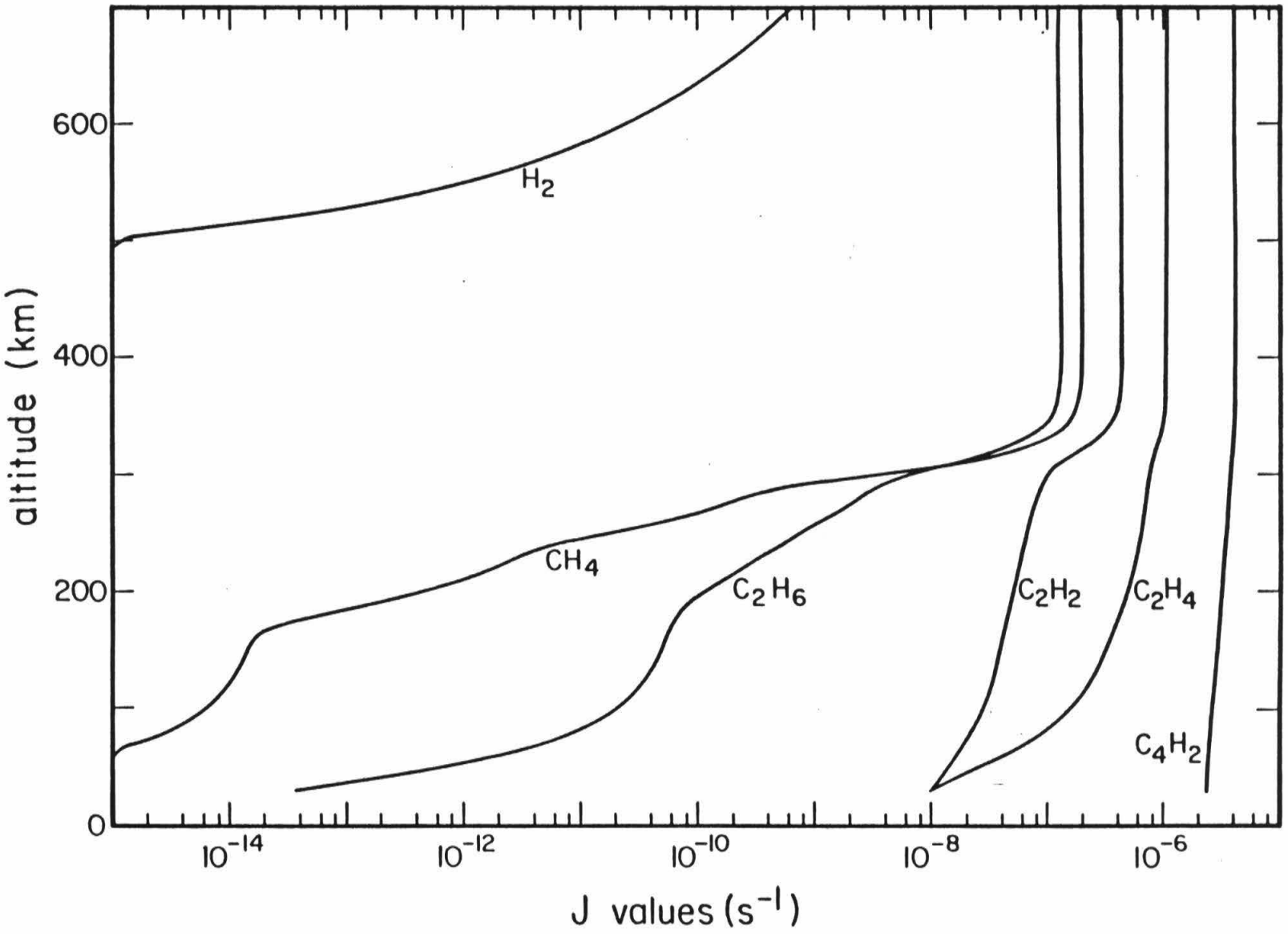
altitude (km)
600
400
200
0
H_2
CH_4
C_2H_6
C_2H_2
C_2H_4
C_4H_2
10^{-14}
10^{-12}
10^{-10}
10^{-8}
10^{-6}
J values (s^{-1})

C_2 species; C_2H_6, C_2H_2, and C_2H_4. However, almost all of the column production of C_2 hydrocarbons is balanced by a loss of C_2H_6 and C_2H_2 by transport across the tropopause. A small fraction is lost to the production of C_3 and higher hydrocarbons.

There are two important layers in the atmosphere that result from the hydrocarbon photochemistry; an upper layer in which CH_4 is dissociated by photons having wavelengths $\lesssim 1500$ Å, and a lower layer in which C_2H_2 is dissociated by photons having wavelengths between 1500 Å and 2000 Å. Figure 4.7 shows the J-values for total absorption by the major species as a function of altitude. Along with Figures 4.3 and 4.4, this figure shows the separation of the two layers. Photons having wavelengths $\lesssim 1500$ Å are essentially gone below ~ 300 km, while photons having wavelengths $\lesssim 2000$ Å are just beginning to be extinguished at the tropopause. Both of these layers can be understood in terms of a few simple chemical pathways and cycles.

In the upper layer the initial or primary synthesis of C_2 hydrocarbons begins with the photodissociation of methane. Ethylene is then produced via the pathways

$$\begin{array}{lcll} CH_4 + h\nu & \rightarrow & {}^3CH_2 + 2H & \text{R3a} \\ CH_4 + h\nu & \rightarrow & {}^1CH_2 + H_2 & \text{R3b} \\ {}^1CH_2 + H_2 & \rightarrow & CH_3 + H & \text{R16b} \\ CH_3 + {}^3CH_2 & \rightarrow & C_2H_4 + H & \text{R21} \\ \hline \text{net} \quad 2CH_4 & \rightarrow & C_2H_4 + 4H & \end{array} \tag{4.13}$$

and

$$\begin{array}{lcll} CH_4 + h\nu & \rightarrow & CH + H + H_2 & \text{R3c} \\ CH + CH_4 & \rightarrow & C_2H_4 + H & \text{R15} \\ \hline \text{net} \quad 2CH_4 & \rightarrow & C_2H_4 + 2H + H_2 & \end{array} \tag{4.14}$$

This ethylene is quickly lost either by photodissociation to become acetylene (R5a, R5b) or recycling to CH_4 via the pathway

$$\begin{array}{rcll} H + C_2H_4 + M & \rightarrow & C_2H_5 + M & R13 \\ C_2H_5 + H & \rightarrow & 2CH_3 & R33a \\ 2(CH_3 + H + M & \rightarrow & CH_4 + M) & R20 \\ \hline \text{net} \quad C_2H_4 + 4H & \rightarrow & 2CH_4 & \end{array} \qquad (4.15)$$

Production of C_2H_4 thus leads, because of its large J-value (see Figure 4.7), directly to producing C_2H_2.

Ethane is produced in the upper layer by

$$\begin{array}{rcll} 2(CH_4 + h\nu & \rightarrow & {}^1CH_2 + H_2) & R3b \\ 2({}^1CH_2 + H_2 & \rightarrow & CH_3 + H) & R16b \\ 2CH_3 + M & \rightarrow & C_2H_6 + M & R22 \\ \hline \text{net} \quad 2CH_4 & \rightarrow & C_2H_6 + 2H & \end{array} \qquad (4.16)$$

Like ethylene, ethane is lost by dissociation to acetylene (R7c; R7a and R7b followed by R5a and R5b) or by recycling to methane (R7a and R7b followed by ethylene recycling as shown in pathway (4.15) above. However, the J-value for ethane is less than that of ethylene by an order of magnitude or more (see Figure 4.7), so that ethane is long-lived in the upper atmosphere and is lost by diffusion to lower altitudes.

Of all the photons absorbed by CH_4 in the upper layer, 70% do not produce any C_2 hydrocarbons (i.e. these photons initiate "do nothing" cycles among the C compounds), 20% result in the production of C_2H_6, and 10% result in the production of C_2H_4.

Once acetylene is produced in the upper layer it is very difficult to get rid of by chemical means. This may seem surprising since C_2H_2 is undersaturated

by a factor of two-thirds and is literally in a bath of H_2. However there are very fast pathways for recycling C_2H_2. The two most important of these are

$$\begin{array}{rcll} H + C_2H_2 + M & \rightarrow & C_2H_3 + M & R12 \\ C_2H_3 + H & \rightarrow & C_2H_2 + H_2 & R29 \\ \hline \text{net} \quad 2H & \rightarrow & H_2 & \end{array} \tag{4.17}$$

and

$$\begin{array}{rcll} C_2H_2 + h\nu & \rightarrow & C_2H + H & R4 \\ C_2H + H_2 & \rightarrow & C_2H_2 + H & R24 \\ \hline \text{net} \quad H_2 & \rightarrow & 2H & \end{array} \tag{4.18}$$

When methylacetylene is included, cycle (4.3) is also very effective at recycling C_2H_2. Since it is recycled so efficiently, the concentration of acetylene builds up until its primary production can be balanced by a diffusion flux to lower altitudes.

In the lower layer acetylene undergoes photolysis and is efficiently recycled as it is in the upper layer. However, because of the lower temperatures near the tropopause, reaction R25 is able to successfully compete with reaction R24 in the recycling process. This results in the "secondary photolysis" of methane, i.e.

$$\begin{array}{rcll} C_2H_2 + h\nu & \rightarrow & C_2H + H & R4 \\ C_2H + CH_4 & \rightarrow & C_2H_2 + CH_3 & R25 \\ \hline \text{net} \quad CH_4 & \rightarrow & CH_3 + H & \end{array} \tag{4.19}$$

Most of the CH_3 produced in this way is recycled back to methane by reaction R20, but a significant fraction ($\sim$ 35%) combines with itself via reaction R22 to produce ethane. Since the average dissociation rate of C_2H_2 in the lower layer is comparable to the average dissociation rate of CH_4 in the upper layer, the total

amount of secondary photolysis is about equal to the total amount of primary photolysis. This source of CH_3 was not considered by Strobel (1969,1973,1975) since the photochemistry of C_2H_2 was not known at that time (Okabe, 1981).

Of all the photons absorbed by C_2H_2 in the lower layer, 80% have no effect on the hydrocarbons (i.e. C_2H_2 is recycled via reaction R24 or the CH_3 produced by reaction R25 is recycled to CH_4 by reaction R20) and 20% result in the production of C_2H_6.

The lower peak in the ethylene concentration profile is due to the three-body recombination of C_2H_2 and H by the pathway

$$\begin{array}{rrcll} & 2(H + C_2H_2 + M & \rightarrow & C_2H_3 + M) & R12 \\ & 2C_2H_3 & \rightarrow & C_2H_4 + C_2H_2 & R32 \\ \hline \text{net} & C_2H_2 + 2H & \rightarrow & C_2H_4 & \end{array} \qquad (4.20)$$

That reaction R32 is able to compete with reaction R29 as a loss process for C_2H_3 is due to the very low concentration of atomic hydrogen in the lower layer. The low concentration of H is due in turn to the high efficiency of pathway (4.17) as a catalytic cycle for recombining H atoms to form H_2. Since the J-value for C_2H_2 in the lower stratosphere is fairly constant (see Figure 4.7) and since H is in photochemical equilibrium the concentration of H in the lower stratosphere is given by

$$[H] \approx \frac{J_4}{k_{12}[M]} \approx \frac{10^{24}}{[M]} (cm^{-3}) \quad . \qquad (4.21)$$

The slight increase of H below an altitude of ~ 90 km is due to reaction R12 reaching the two-body limit.

The rate of all important reactions versus altitude are shown for the standard case in Figures 4.8 through 4.11. Figure 4.8 presents all of the major photodissociation reactions. It may be seen in this figure how R4, the

Figure 4.8

Major photodissociation reaction rates as a function of altitude in the standard model atmosphere.

Figure 4.9

Major three-body reaction rates as a function of altitude in the standard model atmosphere.

Figure 4.10 and Figure 4.11

Major two-body reaction rates as a function of altitude in the standard model atmosphere.

Figure 4.12

Time-constants for chemical loss for the major gases as a function of altitude in the standard model atmosphere. Also shown are the time-constant profiles for transport by eddy diffusion and by molecular diffusion for CH_4.

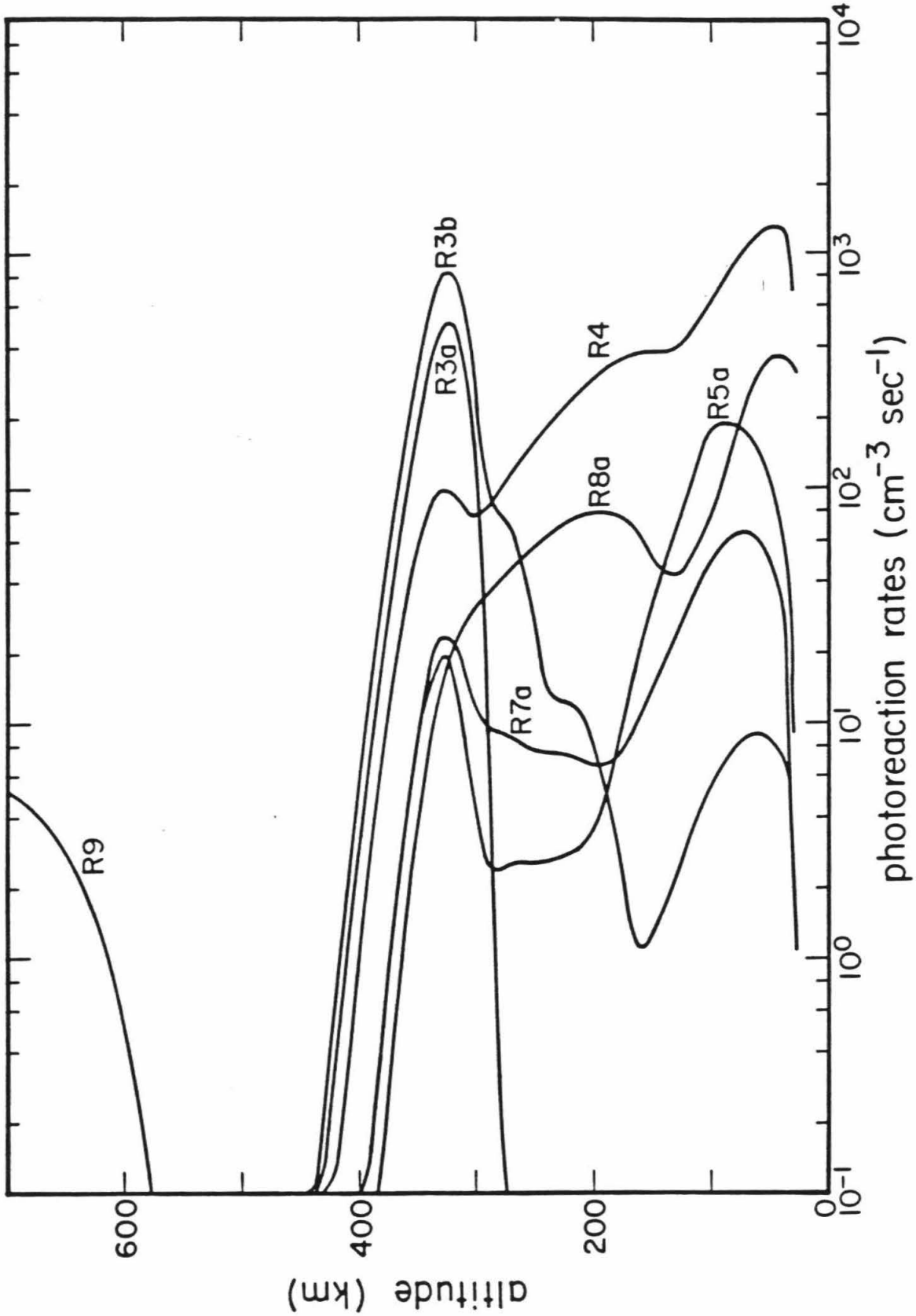
R9
R3b
R3a
R4
R5a
R8a
R7a
600
400
200
0
altitude (km)
10^{-1}
10^{0}
10^{1}
10^{2}
10^{3}
10^{4}
photoreaction rates (cm^{-3} sec^{-1})

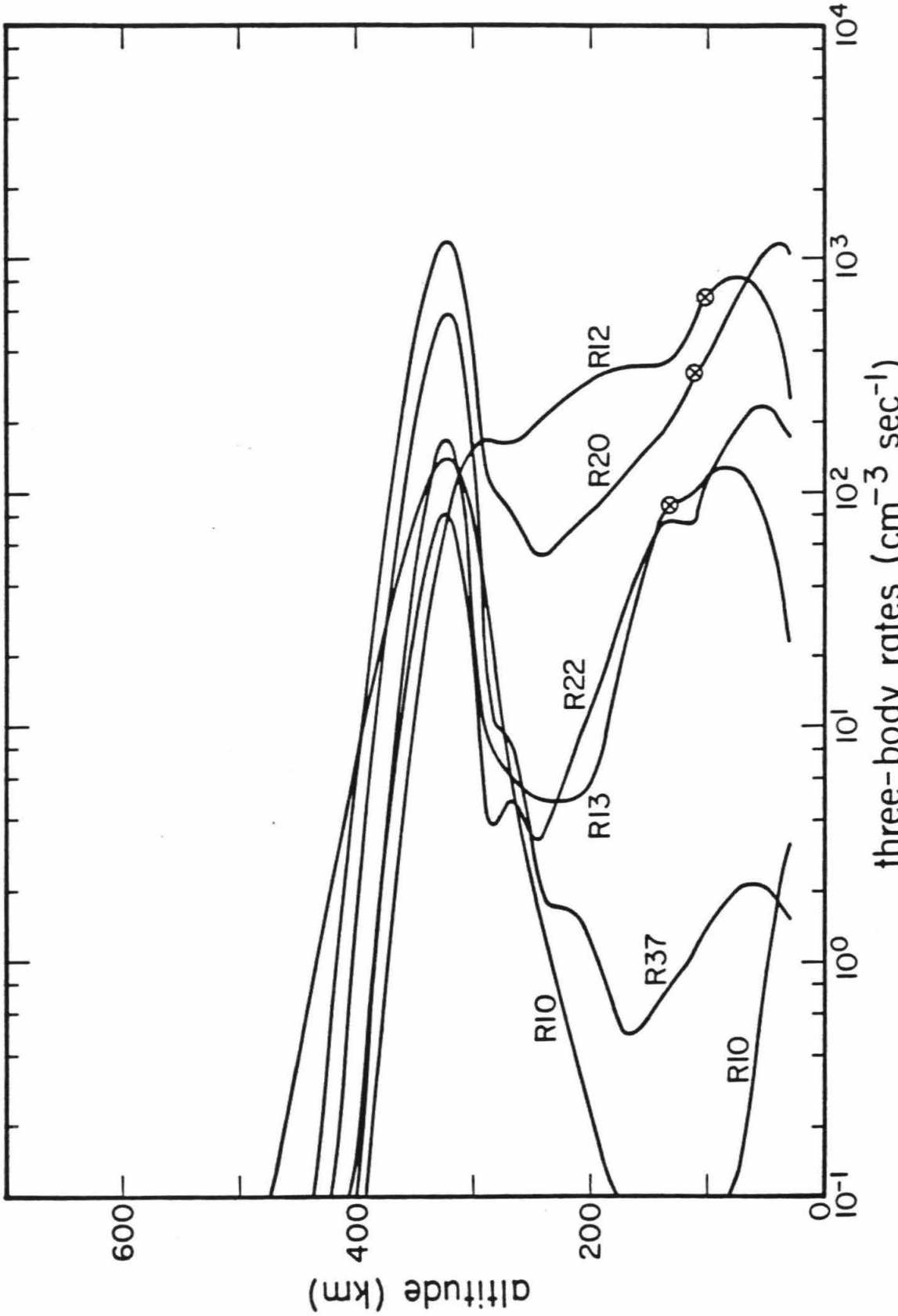
altitude (km)
600
400
200
0
three-body rates (cm^{-3} sec^{-1})
10^{-1}
10^{0}
10^{1}
10^{2}
10^{3}
10^{4}
R12
R20
R22
R13
R37
R10
R10

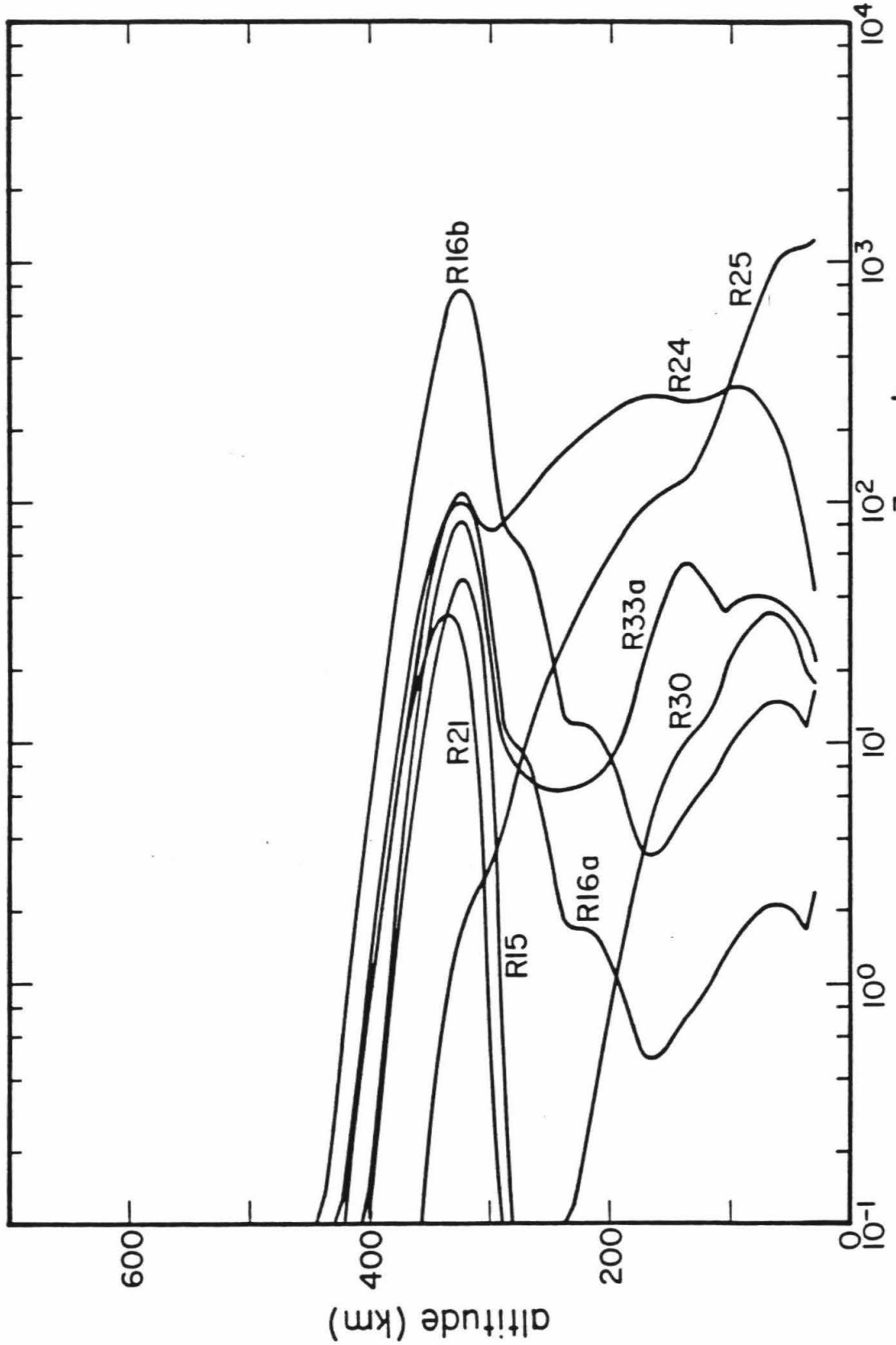
altitude (km)
600
400
200
0
two-body rates (cm^{-3} sec^{-1})
10^{-1}
10^{0}
10^{1}
10^{2}
10^{3}
10^{4}
R16b
R25
R24
R33a
R30
R21
R16a
R15

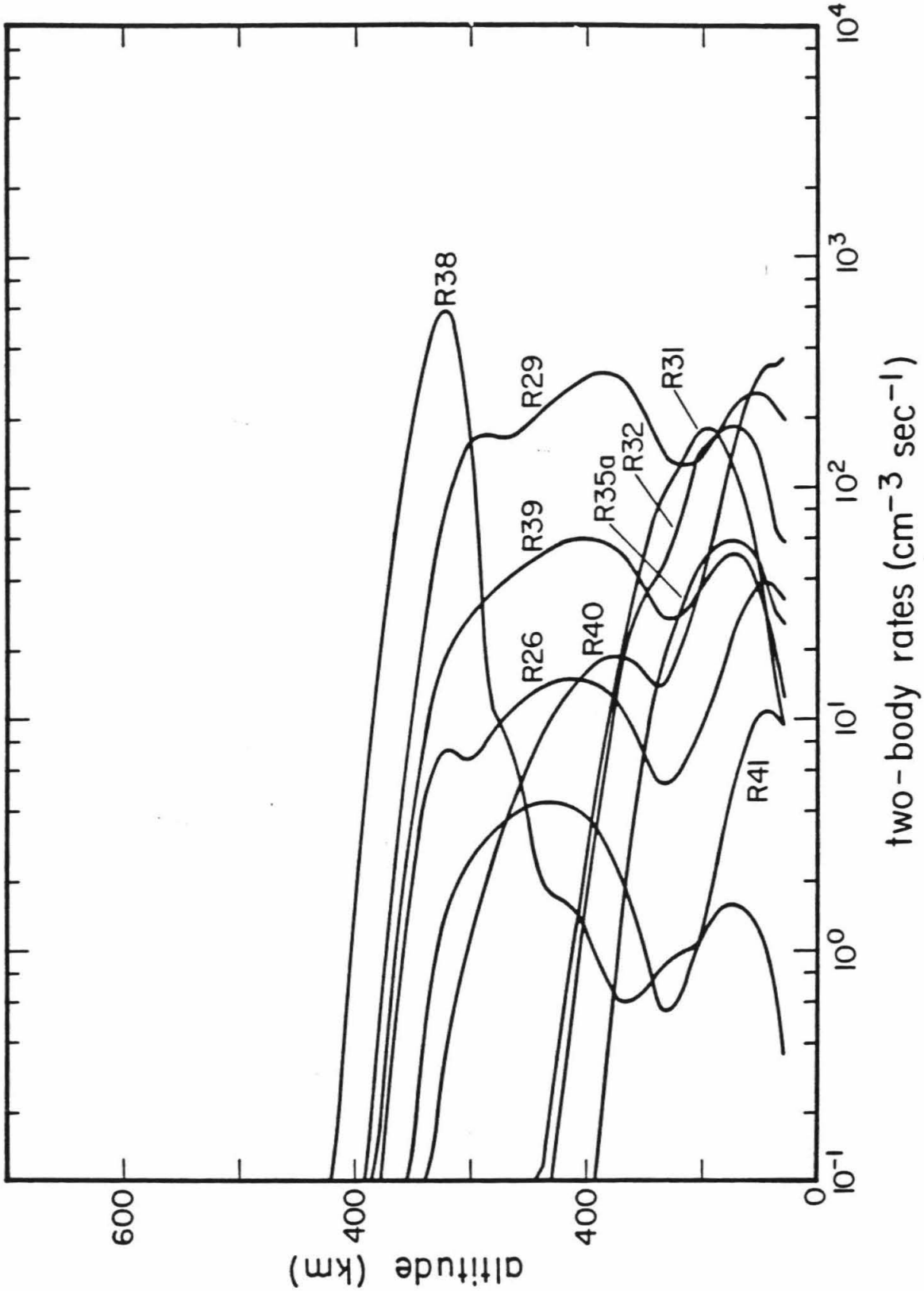
R38
R29
R31
R32
R35a
R39
R40
R26
R41
altitude (km)
two-body rates (cm^{-3} sec^{-1})
600
400
400
0
10^{-1}
10^{0}
10^{1}
10^{2}
10^{3}
10^{4}

altitude (km)
600
400
200
0
10^2
10^4
Jovian day
10^6
10^8
Jovian year
10^{10}
10^{12}
time scale (s)
H^2/D_{CH_4}
H
C_2H_4
C_4H_2
C_2H_2
H^2/K
C_2H_6
CH_4

dissociation rate of C_2H_2, dominates everywhere below the upper layer of CH_4 dissociation (R3a and R3b). The three-body reaction rates are shown in Figure 4.9. Notice how fast R12 is, the first half of the C_2H_2 recycling scheme (4.17). The circled x on the rate profiles of R12, R20, and R13 indicate the level at which the two-body limit is reached. The reactions R22 and R37 are everywhere at their two-body limits and reaction R10 is nowhere at its two-body limit. Figures 4.10 and 4.11 show the important two-body reactions. The dominance of reaction R25 over reaction R24 near the tropopause (mentioned above as the condition for secondary photolysis) can be seen in Figure 4.10.

The chemical loss time scales for the major species and the transport time scales for eddy diffusion and molecular diffusion of methane are presented in Figure 4.12. This figure shows that all the observed hydrocarbons are long-lived in comparison to a Jovian day. In addition, ethane and methane are seen to be long-lived with respect to transport throughout almost the entire atmosphere. It is not surprising to find that the major loss for the ethane produced in the lower layer is transport across the tropopause. Once in the troposphere the ethane is rapidly mixed to deeper levels where it is converted back to CH_4 by pyrolysis. This downward flux of C_2 hydrocarbons (acetylene also contributes $\sim 10\%$ to the total) amounts to $\sim 3 \times 10^9$ C atoms cm^{-2} s^{-1} in the standard model. If it were not balanced by an upward flux of methane from the troposphere, this flux would drain the C_2 hydrocarbons above the tropopause in ~ 3000 years.

4.4 Sensitivity to Eddy Diffusion Profile

Since C_2H_6 is long-lived with respect to vertical transport we expect it to be quite sensitive to changes in the eddy diffusion profile. Acetylene will also be affected by eddy profile changes, but not as much since its chemical lifetime is

less than the transport time scale (see Figure 4.12). Using the mixing ratio constraints obtained in Chapter 2 for the hydrocarbons C_2H_2, C_2H_6, C_4H_2, and C_2H_4, and the constraints obtained by the *Voyager IRIS* and *UVS* experiments (Maguire, 1981; Festou et al., 1981; Atreya et al., 1982) we may decide upon the eddy diffusion profile that best applies to the Jovian upper atmosphere during the time of the *Voyager* encounters. Figures 4.13 through 4.17 show the mixing ratio profiles of C_2H_6, C_2H_2, CH_4, C_4H_2, and C_2H_4 for the eddy diffusion profiles of Figure 4.2. It is recognized that no eddy diffusion fits all the constraints entirely. The C_2H_6 profile is best fit by the $p = 0.6$ case, while the C_2H_2 profile is best fit by the $p = 0.4$ case. The mixing ratios of C_2H_6, C_2H_2, and CH_4 at the homopause overestimate the constraints obtained by Festou et al. (1981) by anywhere from a factor of ~ 2 for the $p = 0.6$ case to a factor of ~ 10 for the $p = 0.4$ case. Atreya et al. (1981) found that an eddy diffusion profile with $p = 0.5$ and $K_t \sim 500$–1000 cm^2 s^{-1} gave the best fit to their data. This is fairly close to our eddy profile with $p = 0.5$. Since the hydrocarbon concentrations are changing very rapidly in the region of the homopause we do not feel that the magnitude of our overestimates is significant. The C_4H_2 constraint is best fit by either the $p = 0.4$ or $p = 0.5$ case, and the C_2H_4 upper limit is overestimated by all three cases. The peculiar shape of the C_2H_4 profile may account for this somewhat. Since the best constraint we have is that for the C_2H_2 mixing ratio, it would appear that the $p = 0.4$ case is the best choice for an eddy diffusion profile. Since there is a possibility that an undiscovered loss process for C_2H_2 exists in the lower stratosphere (e.g. some NH_3, PH_3 photochemistry or heterogeneous reactions with dust particles), we take the profile that fits all the constraints best, that is we choose the $p = 0.5$ case. This choice gives a ~ 50 year vertical mixing time, which is not too much longer than the dynamical estimate of 20 years obtained by Conrath et al. (1980). It also yields a

Figure 4.13

Ethane mixing ratio profiles obtained using the three eddy diffusion profiles of Figure 4.2. Also shown are the constraints obtained for $f_{C_2H_6}$ by Festou et al. (1981) (upper), Chapter 2 (middle), and Maguire (1981) (lower).

Figure 4.14

Acetylene mixing ratio profiles obtained using the three eddy diffusion profiles of Figure 4.2. Also shown are the constraints obtained for $f_{C_2H_2}$ by Festou et al. (1981) (upper), Chapter 2 (middle), and Maguire (1981) (lower).

Figure 4.15

Methane mixing ratio profiles obtained using the three eddy diffusion profiles of Figure 4.2. Also shown is the constraint obtained for f_{CH_4} by Festou et al. (1981).

Figure 4.16

Diacetylene mixing ratio profiles obtained using the three eddy diffusion profiles of Figure 4.2. Also shown is the constraint obtained for $f_{C_4H_2}$ in Chapter 2.

Figure 4.17

Ethylene mixing ratio profiles obtained using the three eddy diffusion profiles of Figure 4.2. Also shown is the constraint obtained for $f_{C_2H_4}$ in Chapter 2.

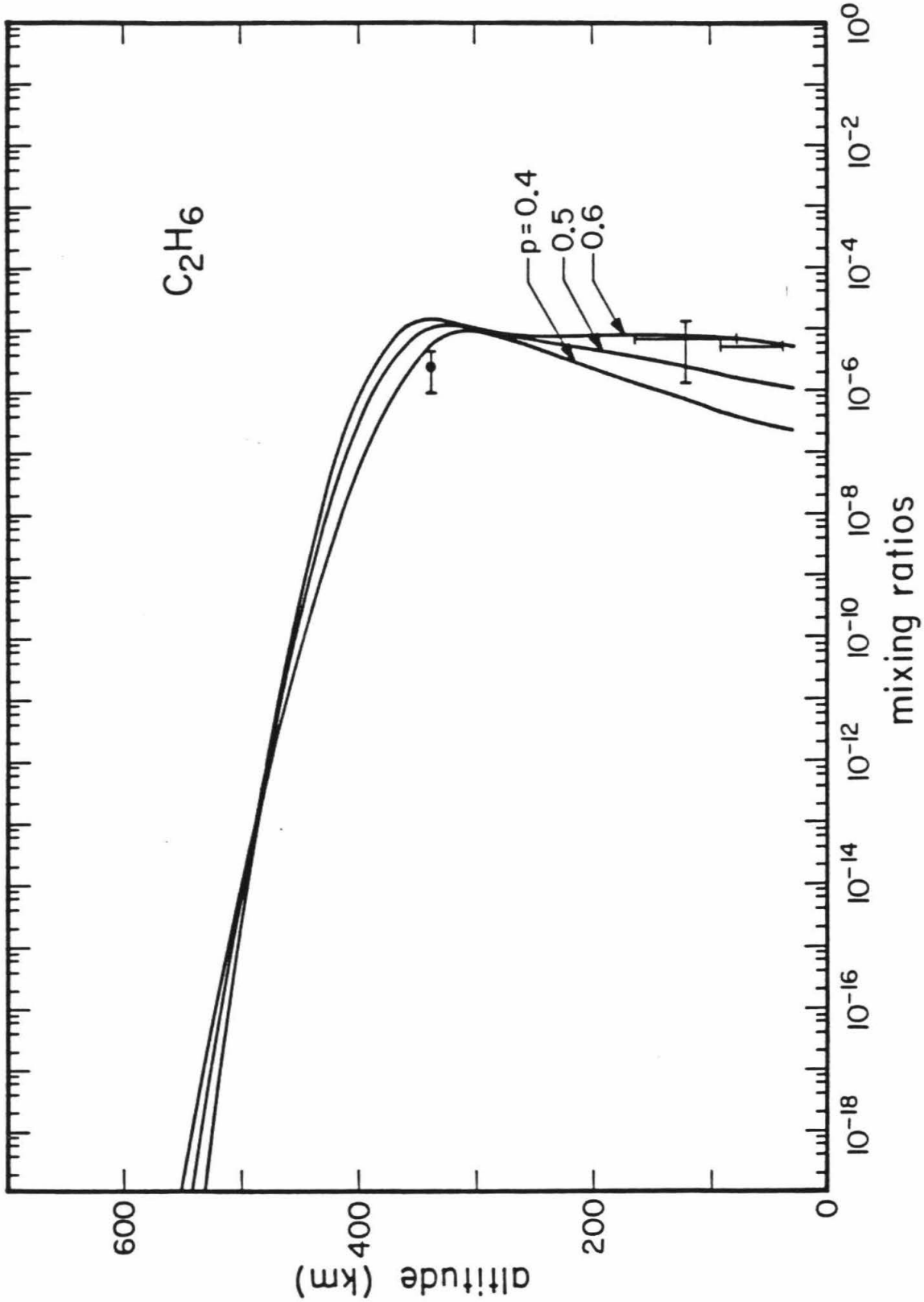
C_2H_6
p=0.4
0.5
0.6
altitude (km)
0
200
400
600
mixing ratios
10^{-18}
10^{-16}
10^{-14}
10^{-12}
10^{-10}
10^{-8}
10^{-6}
10^{-4}
10^{-2}
10^{0}

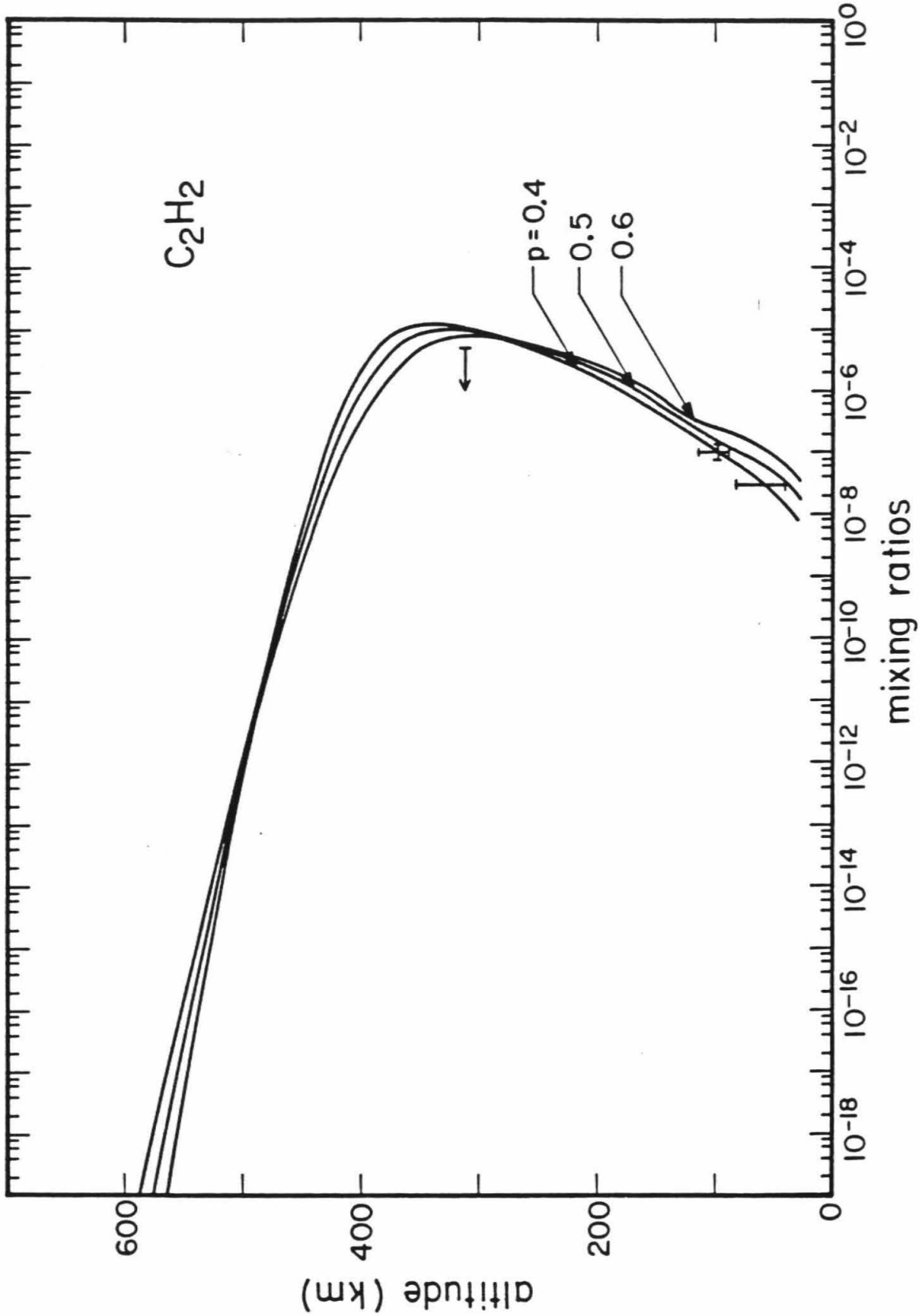
C_2H_2
p=0.4
0.5
0.6
altitude (km)
mixing ratios
0
200
400
600
10^{-18}
10^{-16}
10^{-14}
10^{-12}
10^{-10}
10^{-8}
10^{-6}
10^{-4}
10^{-2}
10^{0}

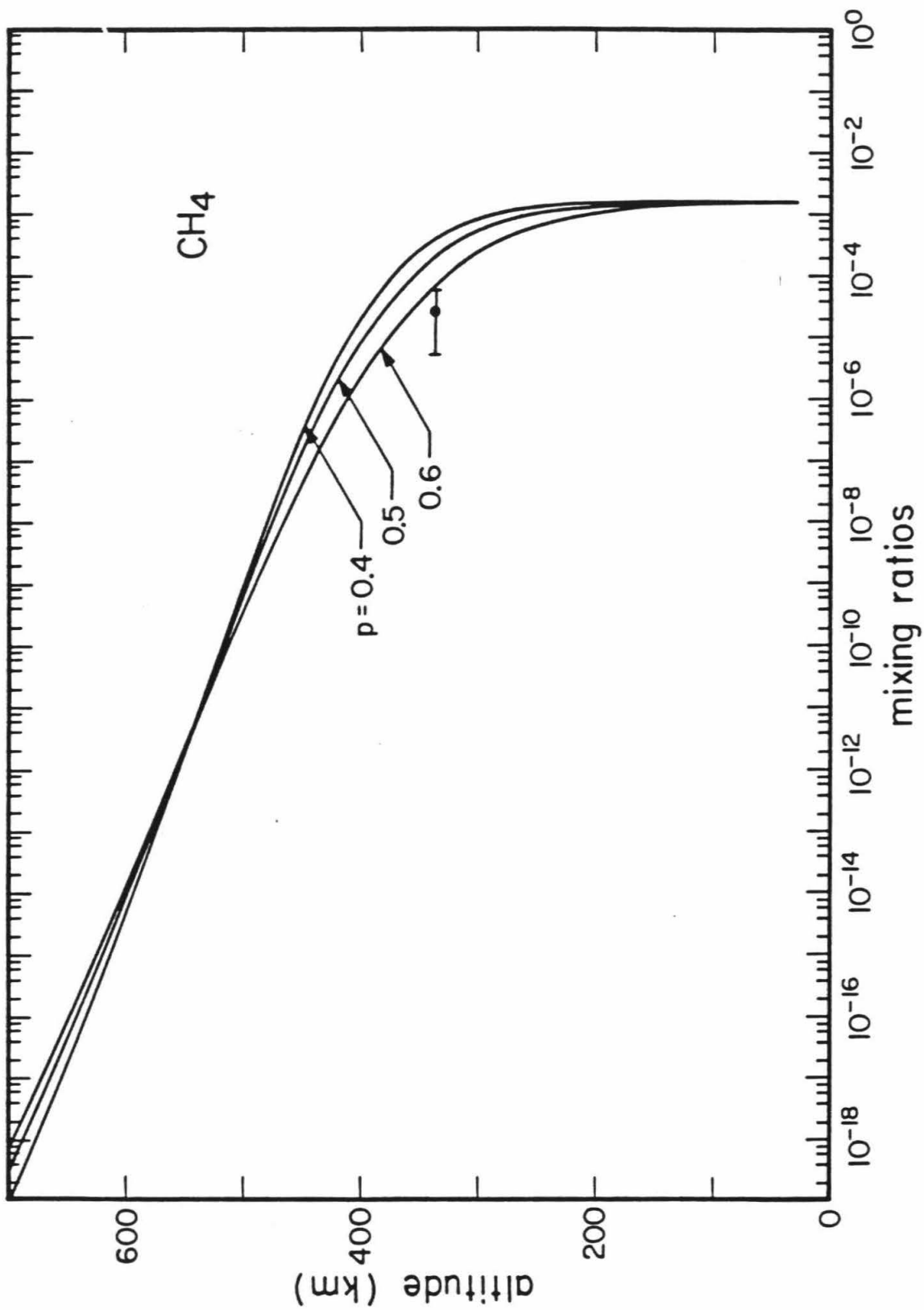
CH4
p = 0.4
0.5
0.6
altitude (km)
0
200
400
600
mixing ratios
10^0
10^-2
10^-4
10^-6
10^-8
10^-10
10^-12
10^-14
10^-16
10^-18

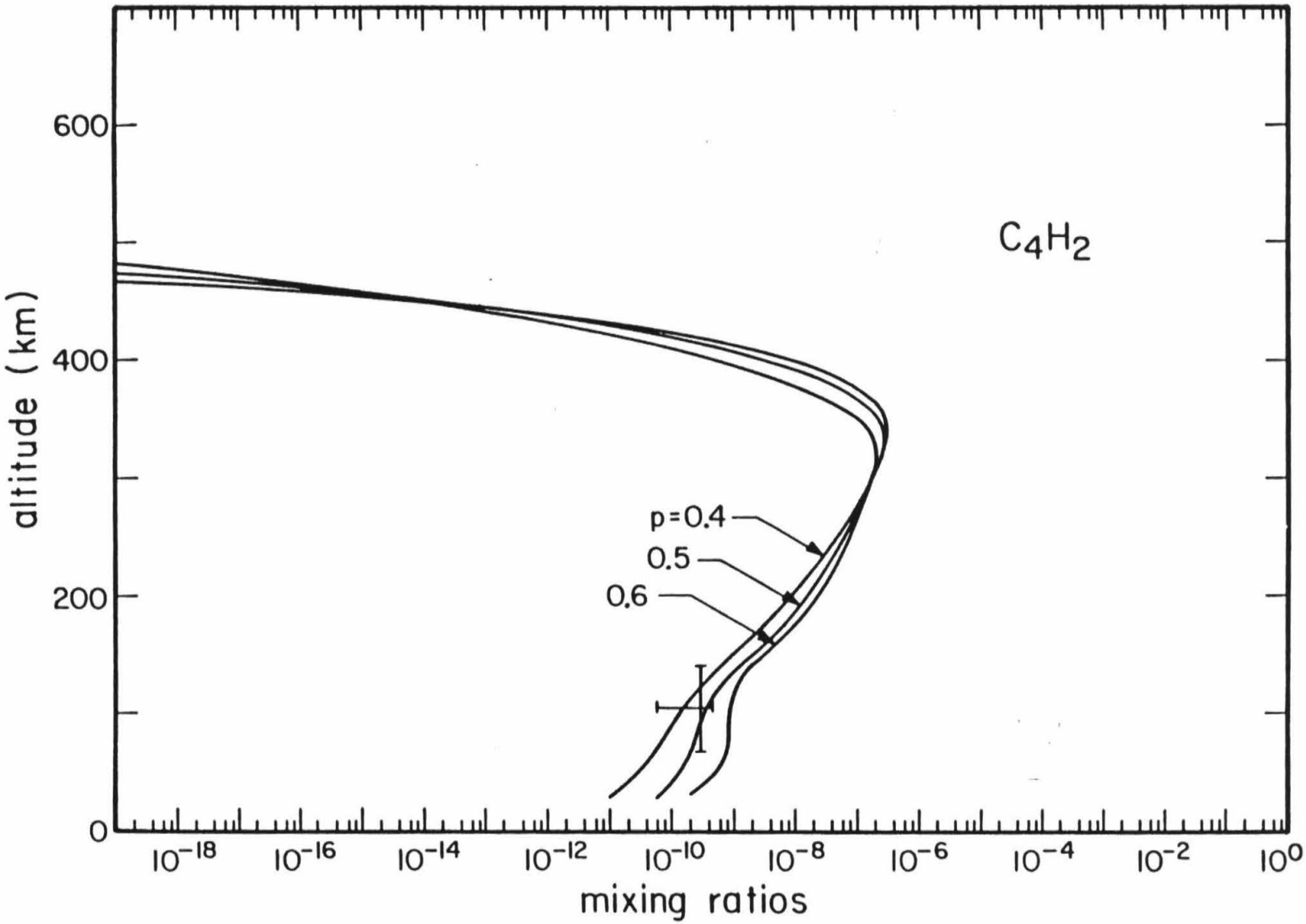
600
400
200
0
altitude (km)
C_4H_2
p=0.4
0.5
0.6
10^{-18}
10^{-16}
10^{-14}
10^{-12}
10^{-10}
10^{-8}
10^{-6}
10^{-4}
10^{-2}
10^{0}
mixing ratios

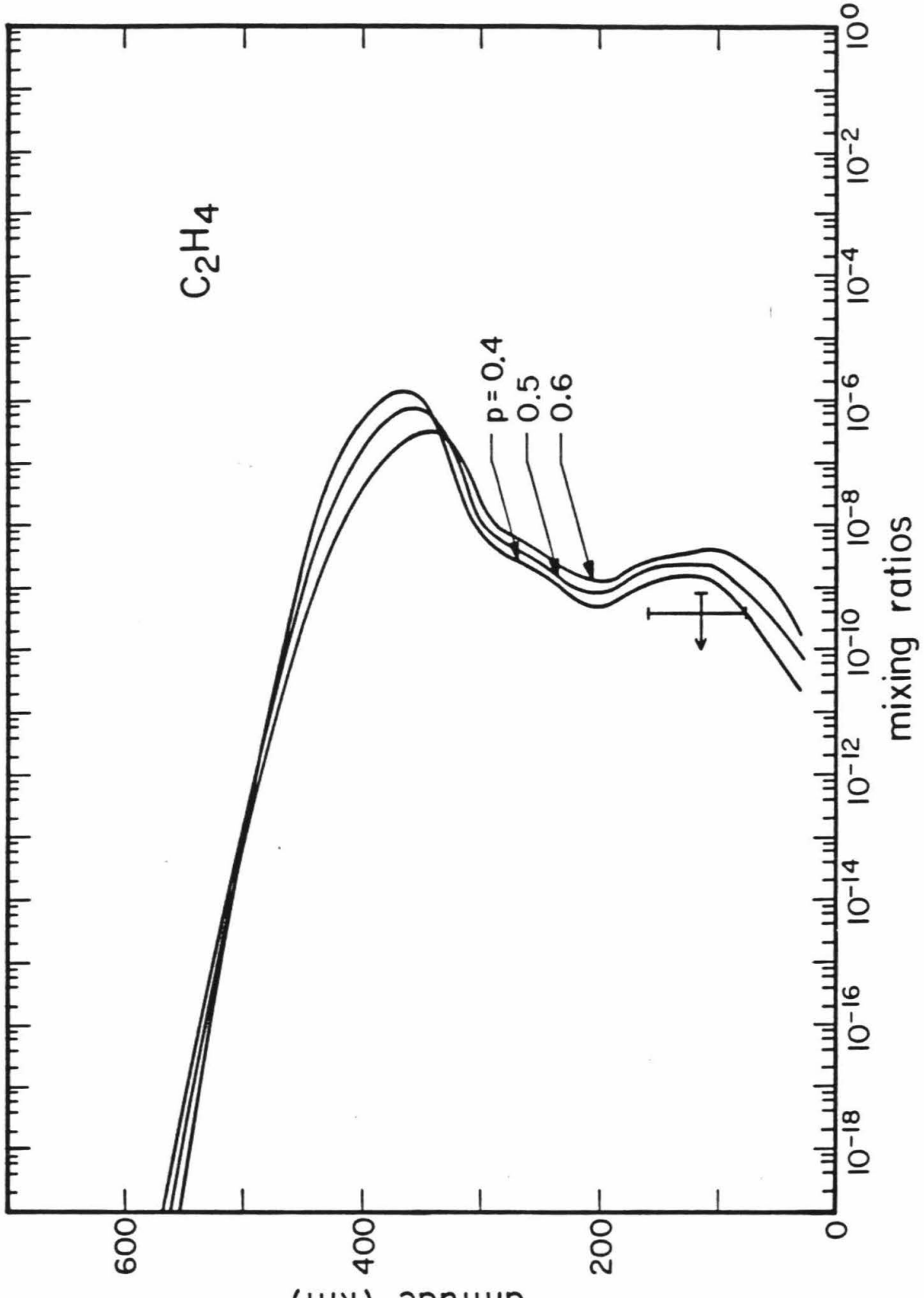
C_2H_4
p = 0.4
0.5
0.6
altitude (km)
mixing ratios
0
200
400
600
10^{-18}
10^{-16}
10^{-14}
10^{-12}
10^{-10}
10^{-8}
10^{-6}
10^{-4}
10^{-2}
10^{0}

C_2H_6/C_2H_2 ratio of 14 at ~10 mbar which is just within the range of 66 ± 53 obtained in Chapter 2.

4.5 Sensitivity to CH_3C_2H and Solar Flux

To test the sensitivity of our model calculations to pathway (4.3) we removed CH_3C_2H from the model in a variation of the standard case. The results of this run are compared with the standard case in Figure 4.18. The main effect of pathway (4.3) is to convert $^3CH_2$ into CH_3, so it is clear why the CH_3 and C_2H_6 profiles are diminished. Methane is also diminished because of reaction R20, while C_2H_2 is increased in the upper layer by reaction R35 and diminished in the lower layer by the loss of pathway (4.3) as a recycling mechanism. This indicates that if we have overestimated the actual CH_3C_2H concentrations in the standard model (as we discussed earlier) that we could improve our fit to the observed constraints in the lower atmosphere. Further investigation of this point will require a much more detailed model than our current one.

The effect of a reduced solar flux on the standard model was tested by replacing the Mount et al. (1980) fluxes with those obtained by Rottman (1981) which refer to solar minimum conditions. The comparison between this run and the standard model is shown in Figure 4.19. Not surprisingly, the lower dissociation rates lead to lower production rates for the C_2 hydrocarbons. This case is also able to fit the observed constraints better than the standard model. Looking back at Figure 4.12 shows that the chemical lifetime of C_2H_2 near the tropopause is comparable to a solar cycle, so perhaps the proper solar flux to use would be an average of the flux over a solar cycle.

4.6 Production of Danielson Dust

The column rate of reaction R41 gives an upper limit to total column

Figure 4.18

Comparison of *CH*3, C_2H_2, C_2H_6, and CH_4 mixing ratio profiles for the standard model atmosphere and a model with CH_3C_2H removed. Also shown are the constraints obtained for $f_{C_2H_2}$, $f_{C_2H_6}$, and f_{CH_4} by Festou et al. (1981) (upper), Chapter 2 (middle), and Maguire (1981) (lower).

Figure 4.19

Comparison of C_2H_2, C_2H_6, and CH_4 mixing ratio profiles for the standard model atmosphere and a model which uses the solar minimum fluxes of Rottman (1981). Also shown are the constraints obtained for $f_{C_2H_2}$, $f_{C_2H_6}$, and f_{CH_4} by Festou et al. (1981) (upper), Chapter 2 (middle), and Maguire (1981) (lower).

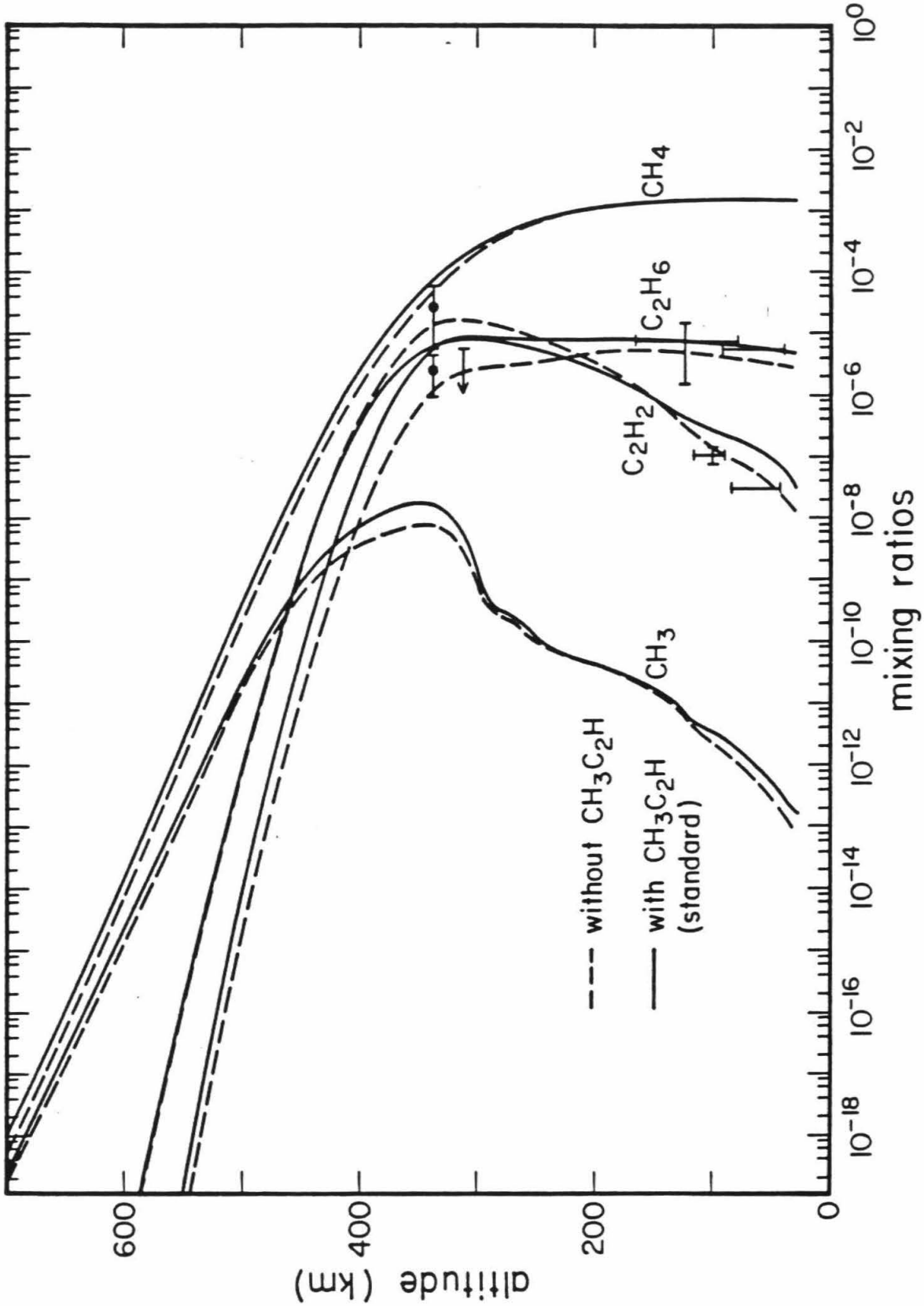
altitude (km)
0
200
400
600
mixing ratios
10^{-18}
10^{-16}
10^{-14}
10^{-12}
10^{-10}
10^{-8}
10^{-6}
10^{-4}
10^{-2}
10^{0}
CH_4
C_2H_6
C_2H_2
CH_3
--- without CH_3C_2H
— with CH_3C_2H (standard)

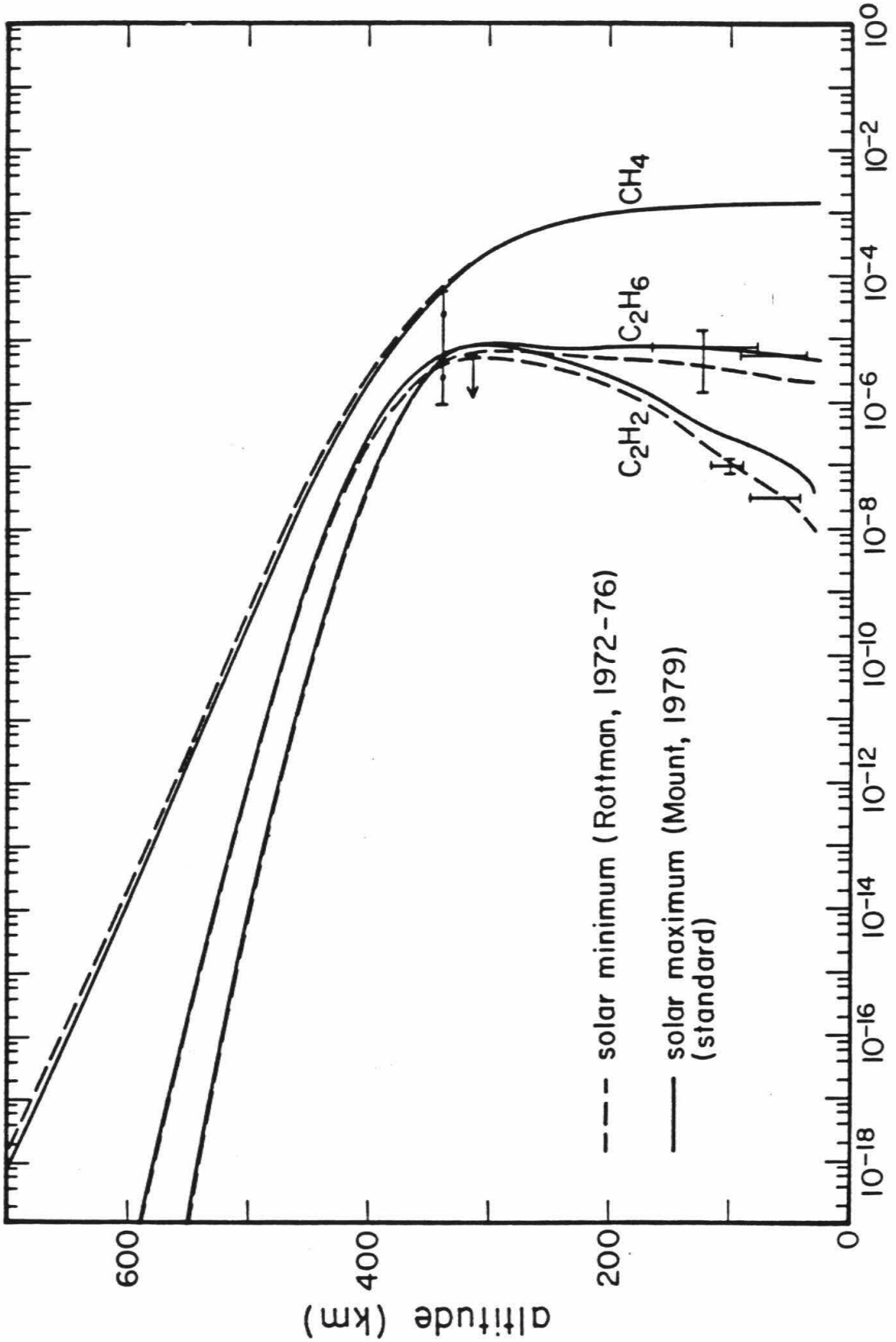
altitude (km)
0
200
400
600
10^{-18}
10^{-16}
10^{-14}
10^{-12}
10^{-10}
10^{-8}
10^{-6}
10^{-4}
10^{-2}
10^{0}
mixing ratios
CH_4
C_2H_6
C_2H_2
--- solar minimum (Rottman, 1972-76)
— solar maximum (Mount, 1979) (standard)

production rate of long-chain polyacetylenes, a possible precursor of Danielson dust. Denoting the column production rate by P we estimate

$$P_{\rm dust} \lesssim P_{41} \frac{m_{c4h2}}{m_{\rm dust}} \quad . \tag{4.22}$$

The column loss of dust will be the downward flux at the tropopause, $\varphi_{\rm dust} \approx n_{\rm dust} w_d$.

Assuming spherical dust particles of radii $r_{\rm dust}$, the extinction optical depth of the dust above the tropopause is given by

$$\tau_{\rm dust} \lesssim \frac{H_{\rm dust} P_{41} m_{c4h2} Q_{ext}}{w_d \rho_{\rm dust} r_{\rm dust}} \tag{4.23}$$

where $H_{\rm dust}$ is the dust scale height, $\rho_{\rm dust}$ is the density of individual dust particles, and Q_{ext} is the ratio of the extinction cross-section to the geometric cross-section. From our standard model $P_{41} \approx 1 \times 10^8$ cm^{-2} s^{-1} and $w_d \approx 3 \times 10^{-4}$ cm s^{-1}. Estimating $H_{\rm dust} \approx 100$ km, $\rho_{\rm dust} \approx 1$ g cm^{-3}, $Q_{ext} \approx 1$, and $r_{\rm dust} \approx 1$ μm, we get $\tau_{\rm dust} \lesssim 3$. This represents a column mass of dust of $\lesssim 4 \times 10^{-4}$ g cm^{-2} or $\lesssim 6 \times 10^{-4}$ of the mass of carbon above the tropopause. The upper limit obtained in Chapter 2 for $\tau_{\rm dust}$ was $0.2^{+0.3}_{-0.2}$, so it is at least conceivable that the Danielson dust observed on Jupiter is produced by the polyacetylene scheme of Allen et al. (1980). Analysis of *Pioneer* 10 and 11 polarimetry data by Stoll (1980) yielded haze particle radii of ~ 0.16 μm at 4400 Å. Stoll also found the particles to be conservative scatterers at that wavelength with an index of refraction of ~ 1.5 and a total optical depth of ~ 0.2 at a pressure level of 200 mbar. For these parameters $Q_{ext} \approx Q_{sca} \approx 0.5$ and Equation (4.23) results in $\tau_{dust} \lesssim 9$ at 4400 Å, consistent with Stoll's result. The nephelometer on the *Galileo* probe and more UV studies such as Hord et al. (1979) and West (1981) may help improve our knowledge of the Danielson dust on Jupiter.

4.7 Column H-Abundance and Lyman-α Dayglow

The column abundance of H atoms in the standard model is 1.0×10^{17} cm^{-2}. The column of H atoms above the $\tau = 1$ level for CH_4 absorption of Lyman-α in the standard model is $\sim 8 \times 10^{16}$ cm^{-2}. Using the frequency redistribution program of Chapter 1 we obtain a disk-averaged ($\mu = \mu_0 = 2/3$) Lyman-α brightness of 7.7 kR with the standard model. This calculation assumed angle-averaged partial frequency redistribution (AAPR) with an isotropic phase function. Actually Lyman-α scattering by H atoms has a phase function which is one-half Rayleigh scattering and one-half isotropic scattering (Hamilton, 1947). This difference should cause our estimate to be low by ~5-10%. The solar Lyman-α profile used in the calculation was that of Vidal-Midjar (1975), normalized to give a line center flux of 5.1×10^{11} ph cm^{-2} s^{-1} Å^{-1} at one astronomical unit. The disk-averaged Lyman-α flux observed by the *Voyager UVS* instrument was ~14 kR. The column of hydrogen doesn't change much among our calculated model atmospheres so we are likely to be low by about a factor of two in all cases. Given the uncertainty in the chemistry, the *UVS* data, the solar line profile, and the method of averaging, we don't feel that this result is too bad. It is possible, however, that we are underestimating the downward flux of H atoms at the top of the atmosphere. Yung and Strobel (1980) found that by increasing this downward flux of hydrogen that they were able to obtain 14 kR of disk-averaged Lyman-α emission. This extra flux of H could be derived from the auroral regions, where there is a large column production of H atoms due to ion-neutral reactions (Yung et al., 1982a), if there is significant meridional transport from pole to equator. Just such a meridional circulation was invoked in Chapter 3 as a possible explanation for the large decrease in K_h between the *Pioneer* and *Voyager* encounters.

4.8 Auroral Chemistry

Early results from the *Voyager IRIS* experiment have indicated that the C_2H_6/C_2H_2 ratio increases by a factor of ~3 from the equator to the pole. This behavior may indicate the importance of auroral processes in the hydrocarbon chemistry at higher latitudes. The ion-neutral chemistry involved is very complex (see Prasad and Huntress, 1980, for example). However, if the aurorae penetrate the homopause (Yung et al., 1982a; Caldwell et al., 1980), the following scheme may help produce extra C_2H_6:

$$
\begin{aligned}
2(e_p + H_2 &\rightarrow H_2^+ + e_s + e_p) \\
2(H_2^+ + H_2 &\rightarrow H_3^+ + H) \\
2(H_3^+ + CH_4 &\rightarrow CH_5^+ + H_2) \\
2(CH_5^+ + e_s &\rightarrow CH_3 + H_2 \\
2CH_3 + M &\rightarrow C_2H_6 + M \\
\hline
\text{net} \quad 2CH_4 &\rightarrow C_2H_6 + 2H
\end{aligned}
\qquad (4.24)
$$

This scheme would depend on the dissociative recombination of CH_5^+ occurring at a faster rate than reactions with C_2H_6 or C_2H_2, and also on the products being CH_3 and H_2 rather than CH_4 and H. While the latter condition is likely to be true based on the structure of CH_5^+ (Hiraoka and Kebarle, 1975), the former condition is fairly unlikely. The reactions

$$CH_5^+ + C_2H_6 \rightarrow C_2H_7^+ + CH_4 \qquad (4.25)$$

$$CH_5^+ + C_2H_2 \rightarrow C_2H_3^+ + CH_4 \qquad (4.26)$$

are likely to be very fast, probably at close to gas-kinetic rates.

As higher order protonated hydrocarbon species such as $C_2H_7^+$ and $C_2H_3^+$ form, proton-transfer reactions become less important, probably because the differences in the proton affinity of the higher hydrocarbons is small. Reactions

that eliminate molecules such as H_2 or CH_4 begin to dominate, e.g.

$$C_2H_3^+ + CH_4 \rightarrow C_3H_5^+ + H_2 \quad . \tag{4.27}$$

The elimination of H_2 or saturated hydrocarbons in these types of reactions may represent a possible dust forming mechanism, especially since the abundance of dust seems to increase from the equator towards either pole (Hord et al., 1979). However, so much of the relevant chemistry is unknown, most importantly the products of dissociative recombination, that the question of the auroral chemistry must be left open at this point.

4.9 Conclusions

We have presented several self-consistent chemical models for the upper atmosphere of Jupiter. It appears that fairly reasonable estimates of the profiles of major constituents may be obtained even when higher hydrocarbon, ammonia, and phosphine chemistry are neglected. The "best fit" eddy diffusion profile we obtain is $K = 1.3 \times 10^6 (2.17 \times 10^{13}/n)^{0.5}$ cm^2 s^{-1}, applicable to the time of the *Voyager* encounters. Given the time constant of the observable species in the lower stratosphere, we predict that the abundances measured by *Galileo* instruments in this region will be slightly higher than they are now (assuming encounter begins prior to 1990). With increased sensitivity of ground-based IR instruments it may be possible to obtain C_2H_6 abundances as a function of latitude (Kostiuk et al., 1981).

When these new studies are completed we will need to revise and expand the chemical models presented here. Until this time, these models may serve as reasonable estimates of the structure of the Jovian upper atmosphere.

Appendix

Auroral processes occur when a beam of high energy particles, usually electrons or ions, is decelerated through numerous elastic and inelastic collisions with atmospheric atoms and molecules. If the particles are of high enough energies, it is convenient to introduce the "continuous-slowing-down approximation" (CSDA) (Peterson and Green, 1968), that is if $\Delta E << E$, then for a small distance Δs along the path of the particle, we have

$$\frac{\Delta E}{\Delta s} \rightarrow \mu \frac{dE}{dz} = n(z)\, L(E,z) \tag{A1}$$

where n is the neutral atmospheric number density and L is the loss-function, which is given by

$$L(E,z) = \sum_i \sum_j \sigma_{ij}(E)\, w_{ij}\, f_i(z) \tag{A2}$$

The loss-function is just the sum of the cross-sections (σ_j) of all of the processes that cause the particle to lose energy (i.e. ionization of atmospheric atoms and molecules, dissociation of atmospheric molecules, etc.) weighted by the average energy lost by the particle during the process (w_j).

From Equation (A1) we see that the energy of a single particle at the level z is given by

$$E(z) = E_0 - \int_z^\infty L(E,z)\, n(z)\, dz / \mu \quad . \tag{A3}$$

The total number of process j events caused by this single particle during its flight is given by Olivero et al. (1973) as

$$N_{ij}(E_0,z) = \int_{w_{ij}}^{E_0} \frac{f_i(z)\sigma_{ij}(E)dE}{L(E,z)} + \int_0^{E_{max}} N_{ij}(T,z)\, n_e(E_0,T)\, dT \quad . \tag{A4}$$

The first term on the right gives the number of events due to the particle itself while the second term on the right gives the number of events due to energetic

electrons released when the particle ionizes atmospheric atoms or molecules. Here $E_{max} = E_o - I$, where I is the ionization energy. If the primary particle happens to be an electron, however, $E_{max} = (E_o - I)/2$, so that the primary can be identified as the more energetic electron. The secondary electron differential number density (electrons unit volume^{-1} unit energy^{-1}) and energy are given by $n_e(E_o,T)$ and T, respectively.

It may be appreciated that the solution of Equation (A4) is quite difficult, particularly if the mixing ratios vary strongly with height. The contribution of the secondary electrons to N_{ij} is usually of the same order of magnitude as the contribution by the primary particle. When a large flux of primary particles is considered, with a large range of initial energies and directions, the problem becomes extremely difficult.

We would like to obtain an estimate of the volume excitation rate profile of a particular process (e.g. Lyman α production) as a result of a large flux F of high energy particles moving through an atmosphere. We consider only those excitations by the primary particles and neglect secondary electrons. By making the approximation

$$\frac{dF}{F} \approx \frac{dE}{E_o} \quad , \tag{A5}$$

we represent the loss of energy of each individual particle by a loss in the total flux of constant energy primaries instead, such that the total particle energy flux at each level is the same in both cases. This approximation, though unphysical, allows us to convert the energy dependence of Equation (A1) into a dependence on altitude only. Inserting Equation (A5) into Equation (A1) we get

$$\frac{dF}{F} = n(z)\frac{L(E_o,z)}{E_o}\frac{dz}{\bar{\mu}} \quad , \tag{A6}$$

where $\bar{\mu}$ is the average of the cosines of the angles of incidence of the particle

flux. From Equation (A6) we have

$$F(z) = \bar{\mu} F_\infty \exp\left[-\frac{1}{E_o \bar{\mu}} \int_z^\infty n(z)\, L(E_o,z)\, dz\right] \quad . \tag{A7}$$

The volume excitation rate is given by

$$P_{ij}(E_o,z) = \sigma_{ij}(E_o)\, F_\infty\, n_i(z) \exp\left[-\frac{1}{E_o \bar{\mu}} \int_z^\infty n(z)\, L(E_o,z)\, dz\right] \quad . \tag{A8}$$

For Jupiter, since H_2 is the major gas in the region of the atmosphere we are interested in (H takes over at densities less than $\sim 10^6$ cm^{-3}), the loss-function $L(E_o,z)$ is approximately constant. Equation (A8) then simplifies to

$$P_{ij}(E_o,z) = \sigma_{ij}(E_o)\, F_\infty\, n_i(z) \exp\left[-\frac{L(E_o)}{E_o \bar{\mu}} N(z)\right] \tag{A9}$$

Instead of using an arbitrary value for $\bar{\mu}$, we could integrate the above expression over a distribution of μ. For a distribution which is isotropic over the downward hemisphere we obtain

$$P_{ij}(E_o,z) = \sigma_{ij}(E_o)\, F_\infty\, n_i(z) E_2\left[\frac{L(E_o)}{E_o} N(z)\right] \quad , \tag{A10}$$

where $E_2(x) = \int_1^\infty e^{-xt} t^{-2} dt$ is the second exponential integral.

We consider two basic types of atmospheres: isothermal and linear-T. For each of these atmospheres, we can derive simple expressions based on Equation (A9) that give the maximum volume production rate, the number density at the level of maximum production, the altitude of this level, and the column production rate, for the case $n_i(z) = f_i n(z)$.

Isothermal atmospheres

For an isothermal atmosphere in hydrostatic equilibrium, we have

$$T = T_o \quad , \tag{A11a}$$

$$n(z) = n(z_o)e^{-(z-z_o)/H_o} \quad , \tag{A11b}$$

and

$$N(z) = n(z_o)H_o e^{-(z-z_o)/H_o} \quad , \tag{A11c}$$

where $H_o = kT_o/\overline{m}g$. From Equation (A9) we have

$$\max P_{ij}(E_o) = \left[\frac{1}{e}\right] \frac{\sigma_{ij}(E_o)\overline{\mu}E_o F_\infty f_i}{L(E_o)H_o} \quad , \tag{A12a}$$

$$n_{P_{\max}} = \frac{\overline{\mu}E_o}{L(E_o)H_o} \quad , \tag{A12b}$$

$$z_{P_{\max}} = z_o + H_o \ln\left[\frac{n(z_o)L(E_o)H_o}{\overline{\mu}E_o}\right] \quad , \tag{A12c}$$

and

$$\int_z^\infty P_{ij}(E_o,z')dz' =$$

$$\frac{\sigma_{ij}(E_o)\overline{\mu}F_\infty E_o f_i}{L(E_o)}\left\{1 - \exp\left[-\frac{L(E_o)}{E_o\overline{\mu}} n(z_o)H_o e^{-(z-z_o)/H_o}\right]\right\} \quad . \tag{A12d}$$

Linear-T atmospheres

Linear-T atmospheres are defined by

$$T(z) = T(z_o) + A(z - z_o) \quad , \tag{A13a}$$

$$n(z) = n(z_o)\left[1 + \frac{A(z - z_o)}{T(z_o)}\right]^{-(\overline{m}g/kA + 1)} \quad , \tag{A13b}$$

and

$$N(z) = n(z_o)H(z_o)\left[1 + \frac{A(z - z_o)}{T(z_o)}\right]^{-\overline{m}g/kA} \quad . \tag{A13c}$$

For this type of atmosphere we find

$$\max P_{ij}(E_o) = \sigma_{ij}(E_o) F_\infty f_i n(z_o)$$

$$\times \exp\left[\left(1 + \frac{kA}{\overline{m}g}\right)\left[\ln\left\{\left(1 + \frac{kA}{\overline{m}g}\right)\left[\frac{E_o\overline{\mu}}{L(E_o)n(z_o)H(z_o)}\right]\right\} - 1\right]\right] , \qquad \text{(A14a)}$$

$$n_{P_{max}} = n(z_o)\left[\left(1 + \frac{kA}{\overline{m}g}\right)\left[\frac{E_o\overline{\mu}}{L(E_o)n(z_o)H(z_o)}\right]\right]^{(1+kA/\overline{m}g)} , \qquad \text{(A14b)}$$

$$z_{P_{max}} = z_o + \frac{T(z_o)}{A}\left[\left\{\left(1 + \frac{kA}{\overline{m}g}\right)\left[\frac{E_o\overline{\mu}}{L(E_o)n(z_o)H(z_o)}\right]\right\}^{-kA/\overline{m}g} - 1\right] , \qquad \text{(A14c)}$$

and

$$\int_z^\infty P_{ij}(E_o, z')dz' = \frac{\sigma_{ij}(E_o)\overline{\mu}F_\infty E_o f_i}{L(E_o)}$$

$$\times \left\{1 - \exp\left[-\frac{L(E_o)n(z_o)H(z_o)}{E_o\overline{\mu}}\left[1 + \frac{A(z - z_o)}{T(z_o)}\right]^{-\overline{m}g/kA}\right]\right\} \qquad \text{(A14d)}$$

The above expressions give very good estimates of the production rates due to the primary particles only. Unfortunately, there is no simple expression for including the effects of secondary electrons, since to calculate n_e in the second term on the right-hand side of Equation (A4) requires knowledge of the differential cross-section for ionization ($S(E,T)$). From Miles et al. (1972),

$$n_e(E_o, T) = \sum_i \int_{2T+I_i}^{E_o} \frac{S_i(E,T)}{L(E)} dE \quad . \qquad \text{(A15)}$$

Numerous studies have been made of the impact of high energy electrons into various neutral gases. It is generally found that the ratio of total production rates to primary production rates for most processes is in the range 1 to 2. Given the uncertainty in cross-sections and in the energy spectrum and fluxes of the primary particles, Equations (A9) through (A14) become quite useful

estimates. As an example Figure A1 shows a comparison between this approximation and the correct solution of Equation (A4) by Heaps et al. (1973). The Heaps et al. calculation is for an initial differential electron flux of

$$\Phi = \mu F_0 \frac{E}{\alpha^2} e^{-E/\alpha} \quad , \tag{A16}$$

with $\mu = 1$, $F_0 = 1 \times 10^{11}$ el cm^{-2} s^{-1}, and $\alpha = 2$ keV. Since our approximation is only for monoenergetic beams, we approximate Φ by two beams, each containing one half of the total flux F_0, at $E = \alpha$ and $E = 3\alpha$. The model atmosphere is approximately isothermal at $T \approx 150$ K. Taking the loss function and Lyα cross-section for electrons on the H_2 from Miles et al. (1972), we obtain from Equation (A9) that

$$P_{Ly\alpha} = 1(25)e^{-z/26}$$

$$\times \left\{2.5(-18)\exp\left[-200e^{-z/26}\right] + 1(-18)\exp\left[-50e^{-z/26}\right]\right\} \quad . \tag{A17}$$

This expression compares very well with the more accurate calculation by Heaps et al. (1973).

Thus, the simple expressions given here can be used to give a fairly accurate estimate of production rate profiles resulting from auroral processes. This method is limited to situations in which the primary energies are large enough that CSDA is applicable and Equation (A5) is a good approximation.

Figure A1

Comparison of Lyman-α production rate profiles obtained by Heaps et al. (1973) by solving Equation (A4) with that obtained using the much simpler Equation (A17).

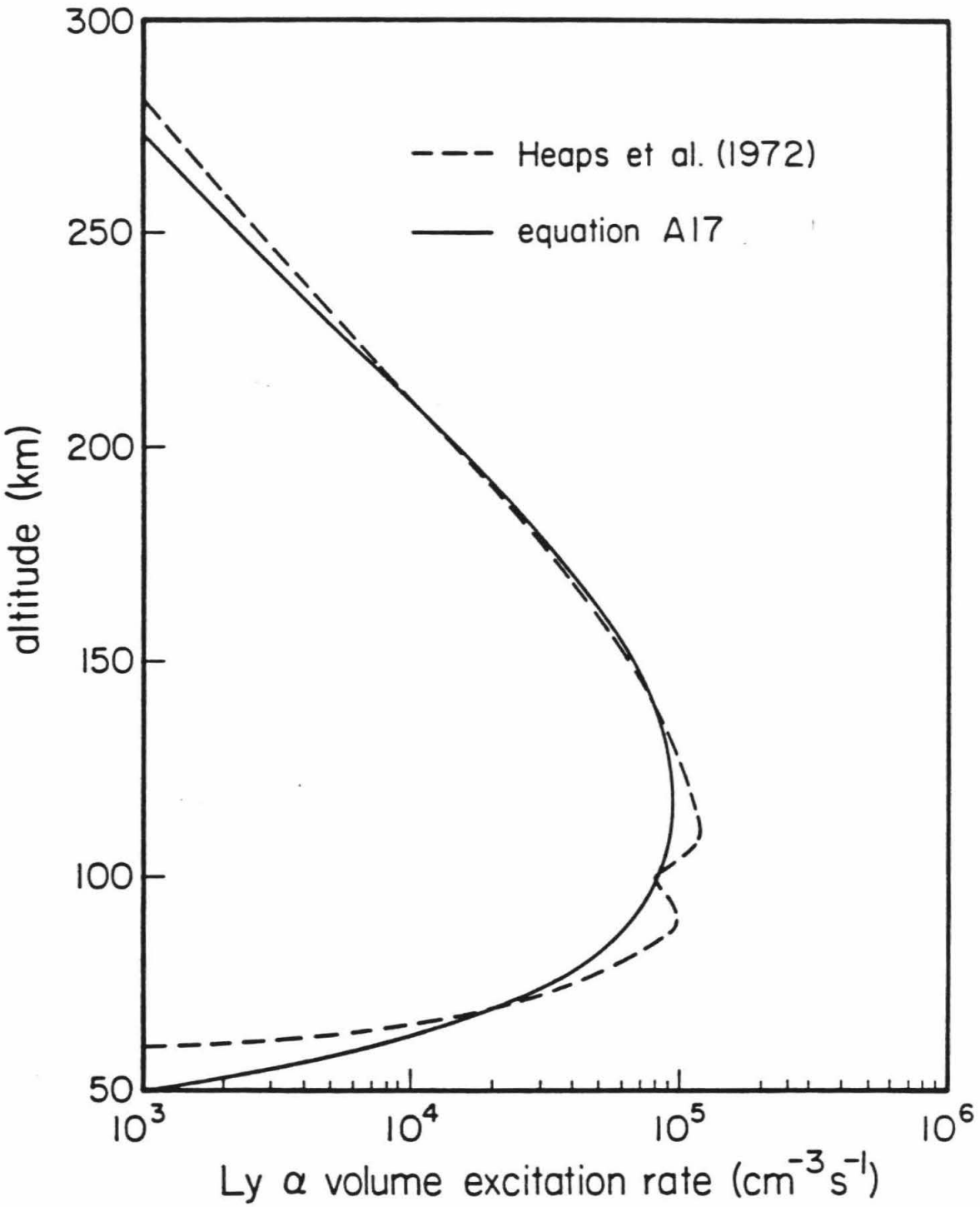
300
250
200
150
100
50
altitude (km)
Heaps et al. (1972)
equation A17
10^3
10^4
10^5
10^6
Ly α volume excitation rate ($cm^{-3}s^{-1}$)

Bibliography

Adachi, N., Basco, N., and James, D.G.L. (1979). A quantitative study of alkyl radical reactions by kinetic spectroscopy III. Absorption spectrum and rate constants of mutual interaction for the ethyl radical, *Intern. J. Chem. Kinet.* **XI**, 995-1005 (1979).

Adams, T.F., Hummer, D.G., and Rybicki, G.B. (1971). Numerical evaluation of the redistribution function $R_{II-A}(x,x')$ and of the associated scattering integral, *J. Quant. Spectros. Radiat. Trans.* **11**, 1365-1376.

Akimoto, H., Obi, K., and Tanaka, I. (1965). Primary process in the photolysis of ethane at 1236 Å, *J. Chem. Phys.* **42**, 3864-3868.

Allen, M., Pinto, J.P., and Yung, Y.L. (1980). Titan: aerosol photochemistry and variations related to the sunspot cycle, *Astrophys. J. Lett.* **242**, L125-L128.

Allen, M., Yung, Y.L., and Waters, J.W. (1981). Vertical transport and photochemistry in the terrestrial mesosphere and lower thermosphere (50-120 km), *J. Geophys. Res.* **86**, 3617-3627.

Anderson, J.D. (1976). The gravity field of Jupiter, in *Jupiter*, T. Gehrels ed., University of Arizona Press, Tucson, pp. 113-121.

Atreya, S.K., Donahue, T.M., and Kuhn, W.R. (1977). The distribution of ammonia and its photochemical products on Jupiter, *Icarus* **31**, 348-355.

Back, R.A. and Griffiths, D.W.L. (1967). Flash photolysis of ethylene, *J. Chem. Phys.* **46**, 4839-4843.

Banyard, S.A., Canosa-Mas, C.E., Ellis, M.D., Frey, H.M., and Walsh, R. (1980). Keten photochemistry. Some observations on the reactions and reactivity of triplet methylene, *J.C.S. Chem. Comm.*, 1156-1157.

Behring, W.E., Cohen, L., Feldman, U., and Doschek, G.A. (1976). The solar spectrum: Wavelengths and identifications from 160 to 770 Angstroms, *Astrophys. J.* **203**, 521-527.

Broadfoot, A.L., Sandel, B.R., Shemansky, D.E., McConnell, J.C., Smith, G.R., Holberg, J.B., Atreya, S.K., Donahue, T.M., Strobel, D.F., and Bertaux, J.L. (1981). Overview of the Voyager ultraviolet spectrometry results through Jupiter encounter, *J. Geophys. Res.* **86**, 8259-8284.

Brown, R.L. and Laufer, A.H. (1981). Calculation of activation energies for hydrogen-atom abstractions by radicals containing carbon triple bonds, *J. Phys. Chem.* **85**, 3826-3828.

Butler, J.E., Fleming, J.W., Goss, L.P., and Lin, M.C. (1981). Kinetics of CH radical reactions with selected molecules at room temperature, *Chem. Phys.* **56**, 355-365.

Caldwell, J., Tokunaga, A.T., and Gillett, F.C. (1980). Possible infrared aurorae on Jupiter, *Icarus* **44**, 667-675.

Callear, A.B. and Metcalfe, M.P. (1976). Oscillator strengths of the bands of the $\tilde{B}^2A_1' - \tilde{X}^2A_2''$ system of CD_3 and a spectroscopic measurement of the recombination rate. Comparison with CH_3, *Chem. Phys.* **14**, 275-284.

Calvert, J.G. and Pitts, Jr., J.N. (1966). *Photochemistry*. John Wiley and Sons, Inc., New York.

Carlson, R.W. and Judge, D.L. (1974). Pioneer 10 ultraviolet photometer observations at Jupiter encounter, *J. Geophys. Res.* **79**, 3623-3633.

Carlson, R.W. and Judge, D.L. (1976). Pioneer 10 ultraviolet photometer observations of Jupiter: The helium to hydrogen ratio, in *Jupiter*, T. Gehrels ed., University of Arizona Press, Tucson, pp. 418-440.

Clarke, J.T., Moos, H.W., Atreya, S.K., and Lane, A.L. (1980). Observations from Earth orbit and variability of the polar aurora on Jupiter, *Astrophys. J. Lett.* **241**, L179-L182.

Clarke, J.T., Moos, H.W., and Feldman, P.D. (1982). The far-ultraviolet spectra and geometric albedos of Jupiter and Saturn, *Astrophys. J.* **255**, 806-818.

Conrath, B.J., Flasar, F.M., Pirraglia, J.A., Gierasch, P.J., and Hunt, G.E. (1981). Thermal structure and dynamics of the Jovian atmosphere 2. Visible cloud features, *J. Geophys. Res.* **86**, 8769-8775.

Cravens, T.E., Victor, G.A., and Dalgarno, A. (1975). The absorption of energetic electrons by molecular hydrogen gas, *Planet. Space Sci.* **23**, 1059-1070.

Dickinson, R.E., Ridley, E.C., and Roble, R.G. (1975). Meridional circulation in the thermosphere I. Equinox conditions, *J. Atmos. Sci.* **32**, 1737-1754.

Doschek, G.A., Behring, W.E., and Feldman, U. (1974). The widths of the solar He I and He II lines at 584, 537 and 304 Å, *Astrophys. J. Lett.* **190**, L141-L142.

Durrance, S.T., Feldman, P.D., and Moos, H.W. (1982). The spectrum of the Jovian aurora 1150-1700 Å, *Geophys. Res. Lett.* **9**, 652-655.

Feautrier, P. (1964). Sur la résolution numérique de l'équation de transfert, *C.R. Acad. Sc. Paris* **258**, 3189-3191.

Festou, M.C., Atreya, S.K., Donahue, T.M., Sandel, B.R., Shemansky, D.E., and Broadfoot, A.L. (1981). Composition and thermal profiles of the Jovian upper atmosphere determined by the Voyager ultraviolet stellar occultation experiment, *J. Geophys. Res.* **86**, 5715-5725.

Ford, A.L. and Browne, J.C. (1973). Rayleigh and Raman cross sections for the hydrogen molecule, *Atomic Data* **5**, 305-313.

Fricke, K.H., von Zahn, V., Combes, M., and Encrenaz, Th. (1982). Ammonia in the Jovian stratosphere: A comparison of photochemical calculations with IUE observations, contribution to *3rd European IUE Conference*, Madrid.

Fuller-Rowell, T.J. and Rees, D. (1980). A three-dimensional time-dependent global model of the thermosphere, *J. Atmos. Sci.* **37**, 2545-2567.

Gardner, E.P. (1981). The vacuum ultraviolet photolysis of methylamine with application to the outer planets and Titan, Ph.D. thesis, University of Maryland, College Park, Maryland.

Gautier, D., Conrath, B., Flasar, M., Hanel, R., Kunde, V., Chedin, A., and Scott, N. (1981). The helium abundance of Jupiter from Voyager, *J. Geophys. Res.* **86**, 8713-8720.

Gautier, D., Bezard, B., Marten, A., Baluteau, J.P., Scott, N., Chedin, A., Kunde, V., and Hanel, R. (1982). The C/H ratio in Jupiter from the Voyager infrared investigation, *Astrophys. J.* **257**, 901-912.

Georgieff, K.K. and Richard, Y. (1958). Diacetylene: preparation, purification and ultraviolet spectrum, *Can. J. Chem.* **36**, 1280-1283.

Gorden, R. and Ausloos, P. (1967). Gas-phase photolysis and radiolysis of methane. Formation of hydrogen and ethylene, *J. Chem. Phys.* **46**, 4823-4834.

Halstead, M.P., Leathard, D.A., Marshall, R.M., and Purnell, J.H. (1970). The reaction of hydrogen atoms with ethylene, *Proc. Roy. Soc. Lond. A.* **316**, 575-591.

Hamilton, D.R. (1947). The resonance radiation induced by elliptically polarized light, *Astrophys. J.* **106**, 457-465.

Hampson, Jr., R.F. and McNesby, J.R. (1965). Vacuum-ultraviolet photolysis of ethane at high temperature, *J. Chem. Phys.* **42**, 2200-2208.

Hanel, R., Conrath, B., Flasar, M., Kunde, V., Lowman, P., Maguire, W., Pearl, J., Pirraglia, J., Samuelson, R., Gautier, D., Gierasch, P., Kumar, S., and Ponnamperuma, C. (1979). Infrared observations of the Jovian system from Voyager 1, *Science* **204**, 972-976.

Heaps, M.G., Bass, J.N., and Green, A.E.S. (1973). Electron excitation of a Jovian aurora, *Icarus* **20**, 297-303.

Heller, S.R. and Milne, G.W.A. (1978). EPA/NIH mass spectral data base, Vol. 1, Molecular weights 30-186. National Bureau of Standards Reference Data Ser. NSRDS-NBS (63), U.S. Dept. Commerce, Washington, D.C.

Hickman, A.P., Isaacson, A.D., and Miller, W.H. (1977). Penning ionization of H_2 by He(2^3S): Quantum mechanical scattering calculations within the rigid-rotor approximation, *J. Chem. Phys.* **66**, 1492-1495.

Hinteregger, H.E. (1977). EUV flux variation during end of solar cycle 20 and beginning cycle 21, observed from AE-C satellite, *Geophys. Res. Lett.* 4, 231-234.

Hinteregger, H.E. (1979). Development of solar cycle 21 observed in EUV spectrum and atmospheric absorption, *J. Geophys. Res.* **84**, 1933-1938.

Hiraoka, K. and Kebarle, P. (1975). Energetics, stabilities, and possible structures of $CH_5^+(CH_4)_n$ clusters from gas phase study of equilibria $CH_5^+(CH_4)_{n-1} + CH_4 = CH_5^+(CH_4)_n$ for n=1-5, *J. Am. Chem. Soc.* **97**, 4179-4183.

Hord, C.W., West, R.A., Simmons, K.E., Coffeen, D.L., Sato, M., Lane, A.L., and Bergstralh, J.T. (1979). Photometric observations of Jupiter at

2400 Angstroms, *Science* **206**, 956-959.

Hudson, R.D. (1971). Critical review of ultraviolet photoabsorption cross sections for molecules of astrophysical and aeronomic interest, *Rev. Geophys. Space Phys.* **9**, 305-406.

Hummer, D.G. (1962). Non-coherent scattering I. The redistribution functions with Doppler broadening, *Mon. Not. R. Astr. Soc.* **125**, 21-37.

Keil, D.G., Lynch, K.P., Cowfer, J.A., and Michael, J.V. (1976). An investigation of nonequilibrium kinetic isotope effects in chemically activated vinyl radicals, *Intern. J. Chem. Kin.* **VIII**, 825-857.

Kostiuk, T., Mumma, M., Deming, D., Espenak, F., Jennings, D., and Zipoy, D. (1981). Heterodyne observations of 12 μm emission from the Jovian south polar region, *Bull. Am. Astr. Soc.* **13**, 738.

Laufer, A.H. (1981a). Kinetics of gas phase reaction of methylene, *Rev. Chem. Intermed.* **4**, 225-257.

Laufer, A.H. (1981b). Reactions of ethynyl radicals. Rate constants with CH_4, C_2H_6, and C_2D_6, *J. Phys. Chem.* **85**, 3828-3831.

Laufer, A.H. (1982). Kinetics and photochemistry of planetary atmospheres, Abstracts, Fourth Ann. Meeting of Planetary Atmospheres Principal Investigators, Ann Arbor, 21-23 April, 1982, 137-138.

Lee, J.H., Michael, J.V., Payne, W.A., and Stief, L.J. (1978). Absolute rate of the reaction of atomic hydrogen with ethylene from 198 to 320 K at high pressure, *J. Chem. Phys.* **68**, 1817-1820.

Lee, J.-S. and Meier, R.R. (1980). Angle-dependent frequency redistribution in a plane-parallel medium: External source case, *Astrophys. J.* **240**, 185-195.

Lee, M.-T. (1981). Private communication.

Lee, M.-T., Lucchese, R.R., and McKoy, V.B. (1982). Electron-impact excitation and dissociation processes in H_2, *Phys. Rev. A*, in press.

Lias, S.G., Collin, G.J., Rebbert, R.E., and Ausloos, P. (1970). Photolysis of ethane at 11.6-11.8 eV, *J. Chem. Phys.* **52**, 1841-1851.

MacFadden, K.O. and Currie, C.L. (1973). Flash photolysis studies in a time-of-flight mass spectrometer. I. Divinyl ether and reactions of the vinyl and vinoxy radicals, *J. Chem. Phys.* **58**, 1213-1219.

Maguire, W. (1981). Private communication.

Mason, E.A. and Marrero, T.R. (1970). The diffusion of atoms and molecules, *Advances in Atomic and Molecular Physics* **6**, D.R. Bates and I. Esterman ed., pp. 155-232.

McConnell, J.C., Sandel, B.R., and Broadfoot, A.L. (1980). Voyager UV spectrometer observations of the He 584 Å dayglow at Jupiter, *Planet. Space Sci.* **29**, 283-292.

McNesby, J.R. and Okabe, H. (1964). Vacuum ultraviolet photochemistry, *Advan. Photochem* **3**, 157-240.

Meier, R.R. and Lee, J.-S. (1981). Angle-dependent frequency redistribution: Internal source case, *Astrophys. J.* **250**, 376-383.

Mentall, J.E. and Gentieu, E.P. (1970). Lyman-α fluorescence from the photodissociation of H_2, *J. Chem. Phys.* **52**, 5641-5646.

Michael, J.V., Osborne, D.T., and Suess, G.N. (1973). Reaction $H + C_2H_4$: Investigation into the effects of pressure, stoichiometry, and the nature of the third body species, *J. Chem. Phys.* **58**, 2800-2812.

Mihalas, D. (1978). *Stellar Atmospheres*. W.H. Freeman and Company, San Francisco.

Miles, W.T., Thompson, R., and Green, A.E.S. (1972). Electron-impact cross sections and energy deposition in molecular hydrogen, *J. Appl. Phys.* **43**, 678-686.

Mount, G.H., Warden, E.S., and Moos, H.W. (1977). Photodissociation cross sections of methane from 1400 to 1850 Å, *Astrophys. J. Lett.* **214**, L47-L49.

Mount, G.H. and Moos, H.W. (1978). Photoabsorption cross sections of methane and ethane, 1380-1600 Å, at $T = 295°$ K and $T = 200°$ K, *Astrophys. J. Lett.* **224**, L35-L38.

Mount, G.H., Rottman, G.J., and Timothy, J.G. (1980). The solar spectral irradiance 1200-2550 Å at solar maximum, *J. Geophys. Res.* **85**, 4271-4274.

Nakayama, T. and Watanabe, K. (1964). Absorption and photoionization coefficients of acetylene, propyne, and 1-butyne, *J. Chem. Phys.* **40**, 558-561.

Nishida, A. and Watanabe, Y. (1981). Joule heating of the Jovian ionosphere by corotation enforcement currents, *J. Geophys. Res.* **86**, 9945-9952.

Okabe, H. (1978). *Photochemistry of Small Molecules*. John Wiley and Sons, Inc., New York.

Okabe, H. (1981). Photochemistry of acetylene at 1470 Å, *J. Chem. Phys.* **75**, 2772-2778.

Olivero, J.J., Bass, J.N., and Green, A.E.S. (1973). Photoelectron excitation of the Jupiter dayglow, *J. Geophys. Res.* **78**, 2812-2826.

Panek, R.J. (1981). Private communication.

Parkes, D.A., Paul, D.M., Quinn, C.P., and Robson, R.C. (1973). The ultraviolet absorption by alkylperoxy radicals and their mutual reactions, *Chem. Phys. Lett.* **23**, 425-429.

Parkes, D.A., Paul, D.M., and Quinn, C.P. (1976). Study of the spectra and recombination kinetics of alkyl radials by molecular modulation spectrometry. Part I. The spectrometry and a study of methyl recombination between 250 and 450 K and perdeutero methyl recombination at room temperature, *J. Chem. Soc. Farad. Trans. I* **8**, 1935-1951.

Patrick, R., Pilling, M.J., and Rogers, G.J. (1980). A high pressure rate constant for CH_3 + H and an analysis of the kinetics of the CH_3 + H – CH_4 reaction, *Chem. Phys.* **53**, 279-291.

Payne, W.A. and Stief, L.J. (1976). Absolute rate constant for the reaction of atomic hydrogen with acetylene over an extended pressure and temperature range, *J. Chem. Phys.* **64**, 1150-1155.

Peterson, L.R. and Green, A.E.S. (1968). The relation between ionization yields, cross sections and loss functions, *J. Phys. B* **1**, 1131-1140.

Phillips, E., Judge, D.L., and Carlson, R.W. (1982). Measurements of the profile of solar He I resonance lines, *J. Geophys. Res.* **87**, 1433-1438.

Prasad, S.S. and Huntress, Jr., W.T. (1980). A model for gas phase chemistry in interstellar clouds: I. The basic model, library of chemical reactions, and chemistry among C, N, and O compounds, *Astrophys. J. Suppl.* **43**, 1-35.

Prather, M.J., Logan, J.A., and McElroy, M.B. (1978). Carbon monoxide in Jupiter's upper atmosphere: An extraplanetary source, *Astrophys. J.*

223, 1072-1081.

Rebbert, R.E. and Ausloos, P. (1972). Photolysis of methane: Quantum yield of $C(^1D)$ and CH, *J. Photochem.* **1**, 171-176.

Rottman, G.J. (1981). Rocket measurements of the solar spectral irradiance during solar minimum, 1972-1977, *J. Geophys. Res.* **86**, 6697-6705.

Sandel, B.R., Shemansky, D.E., Broadfoot, A.L., Bertaux, J.L., Blamont, J.E., Belton, M.J.S., Ajello, J.M., Holberg, J.B., Atreya, S.K., Donahue, T.M., Moos, H.W., Strobel, D.F., Dalgarno, A., Goody, R., McElroy, M.B., and Takacs, P.Z. (1979). Extreme ultraviolet observations from Voyager 2 encounter with Jupiter, *Science* **206**, 962-966.

Sato, M., Kawabata, K., and Hansen, J.E. (1975). A fast invariant imbedding method for multiple scattering calculations and an application to equivalent widths of CO_2 lines on Venus, *Astrophys. J.* **216**, 947-962.

Sato, M. and Hansen, J.E. (1979). Jupiter's atmospheric composition and cloud structure deduced from absorption bands in reflected sunlight, *J. Atmos. Sci.* **36**, 1133-1167.

Sepehrad, A., Marshall, R.M., and Purnell, H. (1979). Reaction between hydrogen atoms and methane, *J. Chem. Soc. Farad. Trans. I* **75**, 835-843.

Slanger, T.G. (1982). 1216 Å photodissociation of H_2O, NH_3 and CH_4, Abstracts, Fourth Ann. Meeting of Planetary Atmospheres Principal Investigators, Ann Arbor, 21-23 April, 1982, 129-131.

Stoll, C. (1980). Polarimetry of Jupiter at large phase angles, Ph.D. thesis, University of Arizona, Tucson, Arizona.

Strobel, D.F. (1969). The photochemistry of methane in the Jovian atmosphere, *J. Atmos. Sci.* **26**, 906-911.

Strobel, D.F. (1973). The photochemistry of hydrocarbons in the Jovian atmosphere, *J. Atmos. Sci.* **30**, 489-498.

Strobel, D.F. (1975). Aeronomy of the major planets: Photochemistry of ammonia and hydrocarbons, *Rev. Geophys. Space Phys.* **13**, 372-382.

Summers, M.E. (1982). Private communication.

Terao, T., Sakai, N., and Shida, S. (1963). Reaction of methylene radicals with acetylene in gas phase, *J. Am. Chem. Soc.* **85**, 3919-3920.

Teng, L. and Jones, W.E. (1972). Kinetics of the reactions of hydrogen atoms with ethylene and vinyl fluoride, *J. Chem. Soc. Farad. Trans. I* **68**, 1267-1277.

Tokunaga, A.T., Beck, S.C., Geballe, T.R., Lacy, J.H., and Serabyn, E. (1981). The detection of HCN on Jupiter, *Icarus* **48**, 283-289.

Torr, M.R., Torr, D.G., Ong, R.A., and Hinteregger, H.E. (1979). Ionization frequencies for major thermospheric constituents as a function of solar cycle 21, *Geophys. Res. Lett.* **6**, 771-774.

Trainor, D.W., Ham, D.O., and Kaufman, F. (1973). Gas phase recombination of hydrogen and deuterium atoms, *J. Chem. Phys.* **58**, 4599-4609.

Troe, J. (1977). Theory of thermal unimolecular reactions at low pressures II. Strong collision rate constants, *Applications J. Chem. Phys.* **66**, 4758-4775.

Van de Hulst, H.C. (1980). *Multiple Light Scattering, Vol. 2.* Academic Press, Inc., New York, p. 544.

van den Bergh, H.E. (1976). The recombination of methyl radicals in the low pressure limit, *Chem. Phys. Lett.* **43**, 201-204.

Vidal-Madjar, A. (1977). The solar spectrum at Lyman alpha 1216 Å, in *The Solar*

Output and Its Variation, O.R. White ed., Colorado Associated University Press, Boulder, pp. 213-234.

von Wagner, H.Gg. and Zellner, R. (1972). Reaktionen von wassertoffatomen mit ungesättigten C_3-kohlen wasserstoffen. II. Die reaktion von H-atomen mit methylacetylen, *Ber. Bunsen-Gesellschaft*, **76**, 518-525.

Wallace, L. and Hunten, D.M. (1973). The Lyman-alpha albedo of Jupiter, *Astrophys. J.* **182**, 1013-1031.

Watanabe, K., Zelikoff, M., and Inn, E.C.Y. (1953). Air Force Cambridge Research Center Tech. Rept. 53-23.

Watanabe, K. (1954). Photoionization and total absorption cross sections of gases. I. Ionization potentials of several molecules. Cross sections of NH_3 and NO, *J. Chem. Phys.* **22**, 1564-1570.

West, R.A. (1981). Sunlight absorption by aerosols in Jupiter's upper atmosphere, *Geophys. Res. Lett.* **8**, 847-849.

Yung, Y.L. and Strobel, D.F. (1980). Hydrocarbon photochemistry and Lyman alpha albedo of Jupiter, *Astrophys. J.* **239**, 395-402

Yung, Y.L., Gladstone, G.R., Chang, K.M., Ajello, J.M., and Srivastava, S.K. (1982a). H_2 fluorescence spectrum from 1200 to 1700 Å by electron impact: Laboratory study and application to Jovian aurora, *Astrophys. J. Lett.* **254**, L65-L69.

Yung, Y.L., Allen, M., and Pinto, J.P. (1982b). Photochemistry of methane, nitrogen, and carbon monoxide on Titan: Abiotic synthesis of organic compounds, submitted to *J. Geophys. Res.*

Zelikoff, M. and Watanabe, K. (1953). Absorption coefficients of ethylene in the vacuum ultraviolet, *J. Opt. Soc. Am.* **43**, 756-759.